Hierarchical Nanostructure of Natural Biominerals and Man-made Semiconductors

by

Jiseok Gim

A dissertation submitted in partial fulfillment
of the requirements for the degree of
Doctor of Philosophy
(Materials Science and Engineering)
in The University of Michigan
2021

Doctoral Committee:

Assistant Professor Robert Hovden, Chair
Professor Emmanuelle Marquis
Professor Zetian Mi
Professor Amit Misra

Jiseok Gim

gjiseok@umich.edu

ORCID ID: 0000-0001-7499-873X

DEDICATION

For my wife who encouraged and supported me to pursue this academic journey.

For my academic adviser who guided me in this process and kept me on track.

For my parents who have brought me into the world and have always loved me .

ACKNOWLEDGMENTS

I would first like to thank my supervisor Professor Robert Hovden for all of his guidance and mentoring during the last 5 years at Michigan. His expertise was invaluable in formulating the research questions and methodology. His insightful feedback pushed me to sharpen my thinking and brought my work to a higher level. During my time in his group, my skills as a researcher, writer, and presenter have dramatically improved as a direct consequence of his skill in these areas and how closely he works with his students. With his understanding and patience, I was able to focus on my research and make the best out of the years I spent as a PhD student at Michigan.

I would also like to thank Professors Zetian Mi, Amit Misra, and Emmanuelle Marquis for serving on my special committee. The discussions and feedback during my preliminary exam and data meeting guided me to think more deeply about the fundamental backgrounds, experimental techniques and my research results. Consequently, I could broaden my perspective and have more confidence when I completed each step of the requirements toward the PhD degree.

My work wouldn't be possible without the dedicated staffs at the Michigan Center for Materials Characterization: Kai Sun, Haiping Sun, Tao Ma, and Bobby Kern. They provided extensive experience and a friendly demeanor that made experimentation pleasant. I am also grateful to have interacted with my labmates who have made my time as a microscopist more enjoyable: Suk Hyun Sung, Jonathan Schwartz, Noah Schnitzer, Alden Koch, Reed Yalisove, Jacob Pietryga, Yin Min Goh, EmJ Rennich, Yu-Ho Lin. Particularly, Suk Hyun and Jonathan

for discussing materials science with electron microscopy both in class and lab. Noah and Alden for developing scientific ideas.

I also thank the professors with whom I've been fortunate enough to work with directly: Zetian Mi, Amit Misra, Dorrit Jacob, Stephan Wolf, Pallab Bhattacharya, John Heron. I would like to acknowledge many brilliant colleagues while in Michigan for their wonderful collaboration: Ayush Pandey, Ping Wang, Laura Otter, Yongjie Wang, Yong Bum Park, Srinivas Vanka, Anthony Aiello, Sheng Chu. Without their support, I could not have such valuable research opportunities.

Finally, I would like to thank my parents for their support over the years, and Ji Hak Kim for being such good sibling. Special thanks to my spouse Anna. I could not have completed this dissertation without her support. Anna is always there for me and she means everything to me. I would also like to thank my nephews for sharing their lives with us so that we feel we are always together even if we are far away.

TABLE OF CONTENTS

GLOSSARY OF ACRONYMS

ADF	Annular Dark Field
BF	Bright Field
CBED	Convergent-beam Electron Diffraction
CTEM	Conventional Transmission Electron Microscope
DF	Dark Field
EQE	External Quantum Efficiency
EELS	Electron Energy Loss Spectrometry
ELNES	Energy-Loss Near Edge Structure
FFT	Fast Fourier Transform
FWHM	Full Width Half Max
HAADF	High-Angle Annular Dark Field
LED	Light Emitting Diodes
STEM	Scanning Transmission Electron Microscope
SNR	Signal to Noise Ratio
MBE	Molecular Beam Epitaxy
TEM	Transmission Electron Microscope
XEDS	X-ray Energy Dispersive Spectroscopy
WPE	Wall-Plug Efficiency

LIST OF FIGURES

FIGURE

ABSTRACT

Materials with structural hierarchy have become a central focus to inspire new designs of next-generation high-performance materials. Using 3D hierarchical architectures that traverse the atomic, nano-, micro-, to macro-scale with precision, nature and humans exploit exotic physical properties or better performance beyond the inherent properties of the materials, such as diffracting iridescence of nacre, unique quantum effects, and parallel computing. However, visible light is a demarcation point because conventional microscopy such as optical microscope cannot resolve the materials below this length scale. In this thesis, we apply scanning transmission electron microscopy (STEM) to investigate materials down to angstrom length scales using the recent advancement of aberration-corrected electromagnetic lenses. First half of this work provides systematic approach on Nacre to understand the superior toughness, the mesocrystalline order, and the self-correcting growth. The second half of this work provides experimental approach on Group III-Nitrides to understand the structure and chemistry attributable to enhance solar conversion efficiency.

The first chapter motivates materials characterization by high-energy electrons for natural biominerals and man-made semiconductors. The exceptional resolving power of STEM with spectroscopic techniques are able to reveal the structural behavior of nacre from macro- to nanoscale and the exotic new phases in group III-nitride at atomic scale.

In Chapter II, our investigation of nacre deformation reveals the underlying nanomechanics that govern the structural resilience and absorption of mechanical energy[1].

Using high-resolution S/TEM combined with in-situ indentation, we observe nanoscale recovery of heavily deformed nacre. The combination of soft nanoscale organic components with inorganic nanograins hierarchically designed by natural organisms results in highly ductile structural materials that can withstand mechanical impact and exhibit high resilience on the macro- and nano-scale.

Chapter III presents Nacre's remarkable medium-range mesocrystal formed through corrective processes that remedy disorder and topological defects[2]. In layered growth of nanomaterials, external guidelines don't exist and mesocrystallinity is prohibitive. In rare instances Nature unconsciously assembles mesocrystals—which merits our attention. The entire nanostructure of nacreous pearls is characterized in cross-section to reveal complex stochastic processes that govern ordered nacre growth. Mollusks strike balance between preserving translational symmetry and reducing thickness variation by creating a paracrystal with medium-range order (5.5 μm). This balance allows Pearls to attenuate the initial disorder during early formation and maintain order throughout a changing external environment.

In Chapter IV, the thesis extends the InGaN ternary system, that is an optimal photoelectrode for efficient solar hydrogen production[3-5]. However, it is difficult to grow high crystalline InGaN with uniformly homogeneous indium composition because In-rich crystals are highly strained causing phase segregation and subsequent performance degradation[6]. Here, aberration-corrected STEM combined with analytic spectroscopy such as EELS and XEDS is used to study crystallinity and compositional uniformity in 1D InGaN heteroepitaxy.

Finally, in Chapter V we discuss AlGaN ternary system for high-efficiency deep UV light sources. It is the only alternative technology to replace mercury lamps for water

purification and disinfection[7-9]. At present, however, AlGaN-based mid- and deep UV LEDs exhibit very low efficiency. Here, we investigate the interface phenomenon of 2D AlGaN such as tunnel junction, quantum wall, and nanoclusters in active region to enhance light emitting performance[9-12].

CHAPTER I

Introduction

1.1. Hierarchical Structure

1.1.1. Hierarchical Structures Both from Nature and from Humans

Materials with structural hierarchy offer unique properties that are far beyond inherent property of each components or exhibit exotic behavior by structuring the components across multiple length scale[13]. Nature has optimized high-performance materials using 3D hierarchical architectures that traverse the atomic, nano-, micro-, to macro-scale with precision that human technology is yet to achieve[14]. Structural features arose from Nature give rise to enhanced physical properties such as structural coloration of peacock's tail feathers[15], water-repellent surface of lotus[16], and superior toughness of biominerals such as bone[17] and enamel[17,18]. Inspired by nature, man-made hierarchical materials also exhibit excellent performance. In the semiconductor industry, many transistors and gates are interconnected and extend horizontally and even vertically to build D-RAM memory or CPU processors. Humans even engineer materials at atomic scales when tuning bandgaps in optoelectronics.

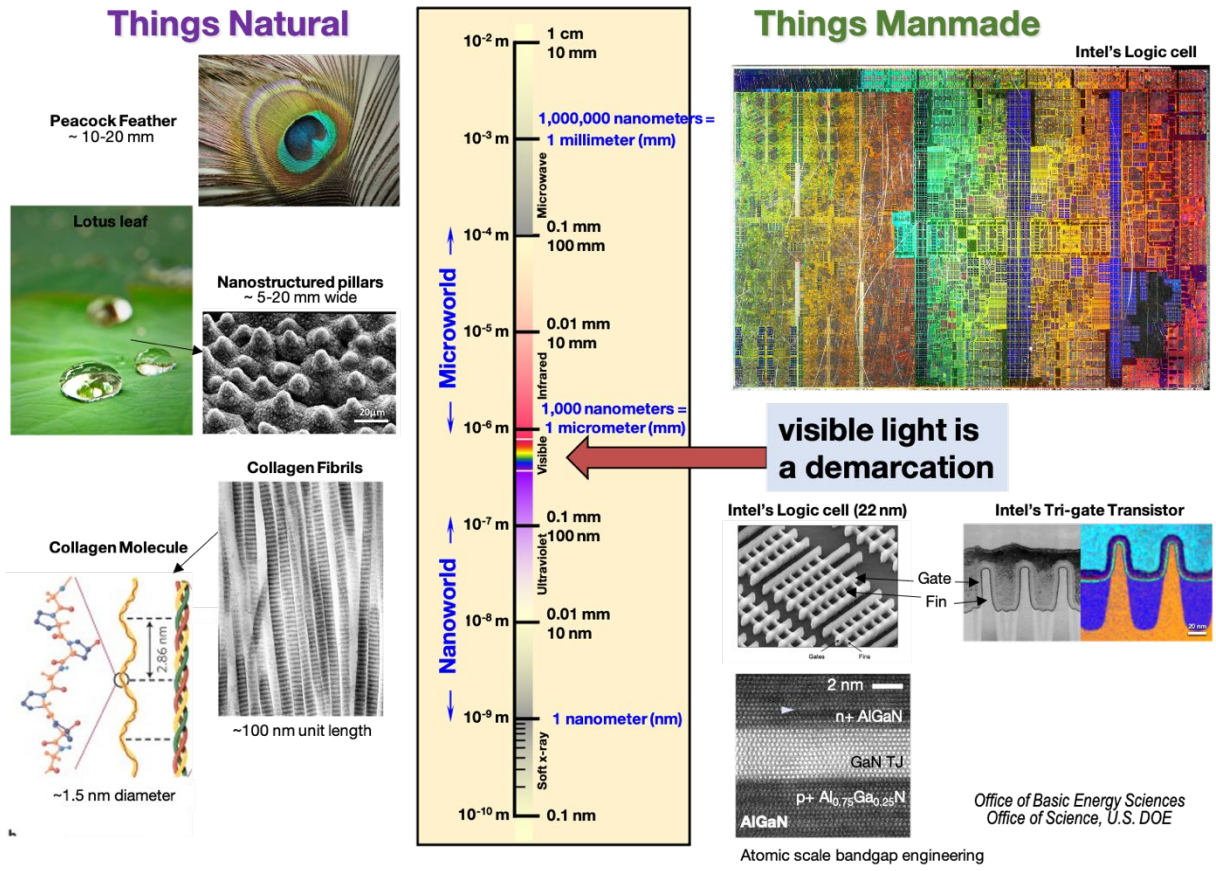

Figure 1.1 Hierarchical structures created by nature and by human[19-26]. **a** Living organism structured by nature traversing from microscale to sub-nanometer scale. **b** Man-made architectures applied for a wide range of area such as CPU, memory, capacitor, and LEDs to make our lives better. This figure is adapted and modified from Office of Basic Energy Sciences and Office of Science, U.S. DOE to include data from Ref. [19-26].

1.1.2. Biominerals

Nacre is the iconic supermaterial because it has beautiful diffracting iridescence on the macroscale and is one of the toughest materials in nature. Like chalk, nacre is composed of $CaCO_3$, but it is much tougher and stronger than chalk. Although you can easily break chalk when you drop it, you cannot break a mollusk shell or a pearl at all by dropping it or even by biting with your teeth. Among the diverse set of structural biominerals that straddle the gap between strength and toughness[17,18,27], nacre is the prototypical supermaterial[17,24,28-30]. The

biomineralization precisely controls secretion of organic and inorganic ingredients and hierarchically designs the combination of soft nanoscale organic components with inorganic nanograins that govern the formation of pearls and shells[31]. In nacre, aragonite polygon tablets are periodically stacked and connected by ~10 nm interlamellar membrane and each polygon is composed of lots of nanograins and intra-crystalline organics[1] (Fig. 1.2b). During indentation, all these components heavily deform and absorb the external force. Therefore, this hierarchical structure reveals unrivaled strength, toughness, and resilience, which is much more malleable than the bulk $CaCO_3$ like chalk[32-35]. We want to learn from nature to develop superior materials technology.

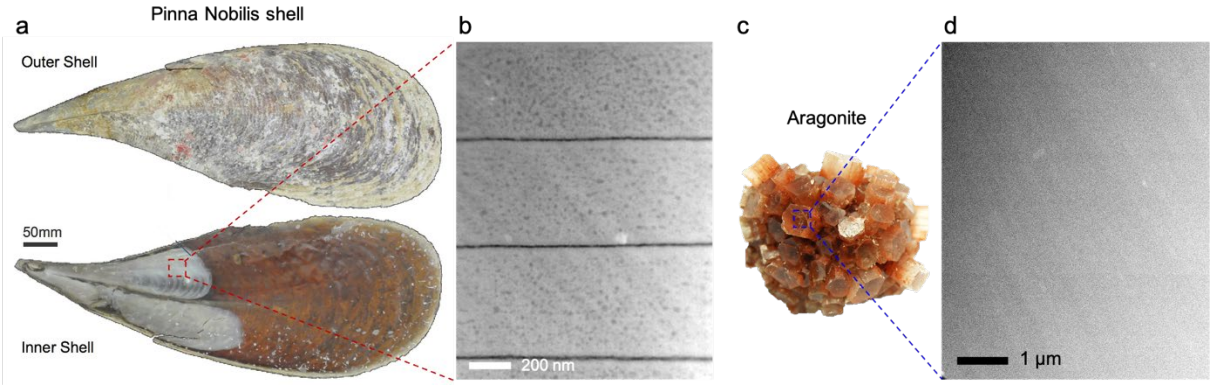

Figure 1.2 Biogenic aragonite and geological aragonite. **a** Schematic of the bivalve mollusk P. nobilis[31] [adapted from Ref. 31]. The inner shell surface made of nacre (i.e., biogenic aragonite) and outer shell surface composed of prismatic calcite. **b** HAADF-STEM shows the cross-section of nacre the investigated area marked by a red square. **c** Schematic of geological aragonite. **d** HAADF-STEM shows the cross-section of the monolithic aragonite.

1.1.3. Group III-Nitrides

Group III-Nitride material is a great example of artificially engineered hierarchical structure to improve device performance by learning from nature. Using bottom-up growth and top-down templating, low-dimensional nanostructures accommodate crystalline InGaN nanowires or AlGaN thin films capable of enhanced photovoltaic device performance. The

bandgap (E_g) of InGaN or AlGaN is direct and tunable from 3.4 (GaN) to 0.65 eV (InN) or from 6.2 (AlN) to 3.4 (GaN). Thus, it covers almost the entire solar spectral range spanning from the deep unltraviolet (UV) to the near-infrared (NIR) wavelengths unlike other crystal structure of the III-nitrides or other III-V materials. Moreover, the ternary system has the large piezoelectric constants, high mechanical and thermal stability. The Group III-Nitride ternary system is optimal photovoltaic materials for efficient device applications such as solid-state lighting, LED displays, photoelectrochemical water splitting, and high-power devices capable of high-voltage and high-temperature[36-39]. However, engineering the optical bandgap is challenging. For example, In-rich crystals are highly strained causing phase segregation and subsequent performance degradation due to the large lattice mismatch between InN and GaN. Using plasma-assisted molecular beam epitaxy (MBE) together with the optimal growth parameter such as lithographic template, non-planar substrate, and concentration of adatoms, highly crystalline InGaN and AlGaN can be grown as one dimensional (1D) or two dimensional (2D) nanostructures, reducing phase segregation and allowing high quantum efficiency.

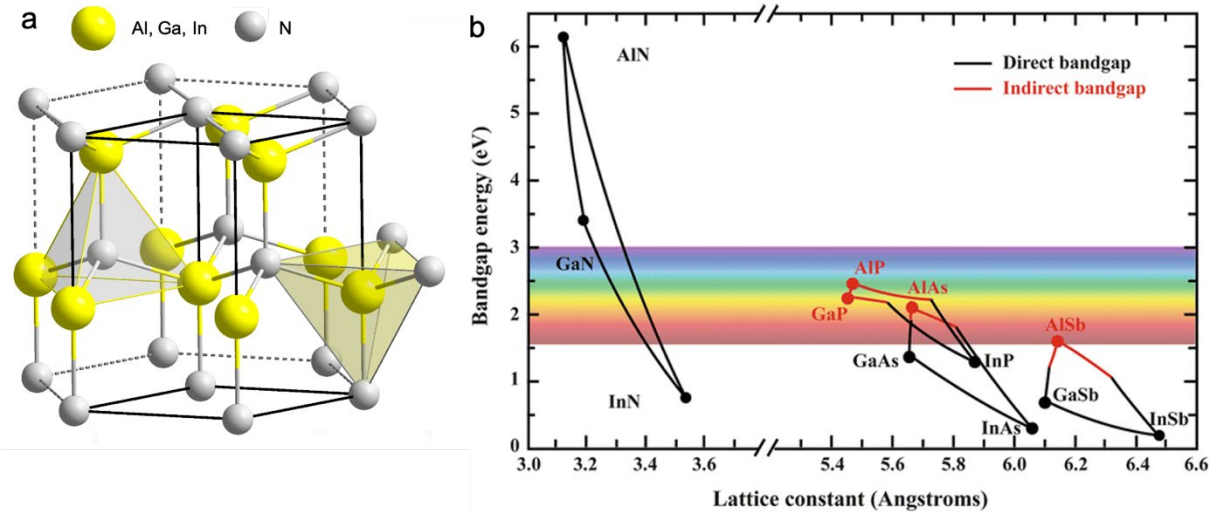

Figure 1.3 Wurtzite phase of Group III-V nitrides **a** Wurtzite symmetry of the crystal structure[19] [adapted from Ref. 19]. **b** Wurtzite phase of group III-nitrides revealed direct bandgap spanning from the deep UV to the near infrared spectrum[40] [adapted from Ref. 40].

1.2. Transmission Electron Microscope (TEM)

1.2.1. Scanning Transmission Electron Microscope (STEM)

Both the natural biomineral and the man-made semiconductors are grown with hierarchical order that spans the macro- to atomic- scale. Visible light is a demarcation point because conventional microscopy such as optical microscope cannot resolve below this length scale. Electron beams have much smaller wavelength that allows materials to be resolved down to atomic length scales. In electron optics, the spatial resolution is limited by the lens aberrations, which broaden the distribution and the spatial localization of the intensity of the electron probe[41-43]. Aberration correctors fix the geometric aberrations and confine electron probe to sub-angstrom. The confined electron-probe enables not only a better spatial resolution but also the higher peak intensity provides far better sensitivity to single atoms. The structure and chemistry of materials can be correlated to the electrical, optical, and magnetic properties.

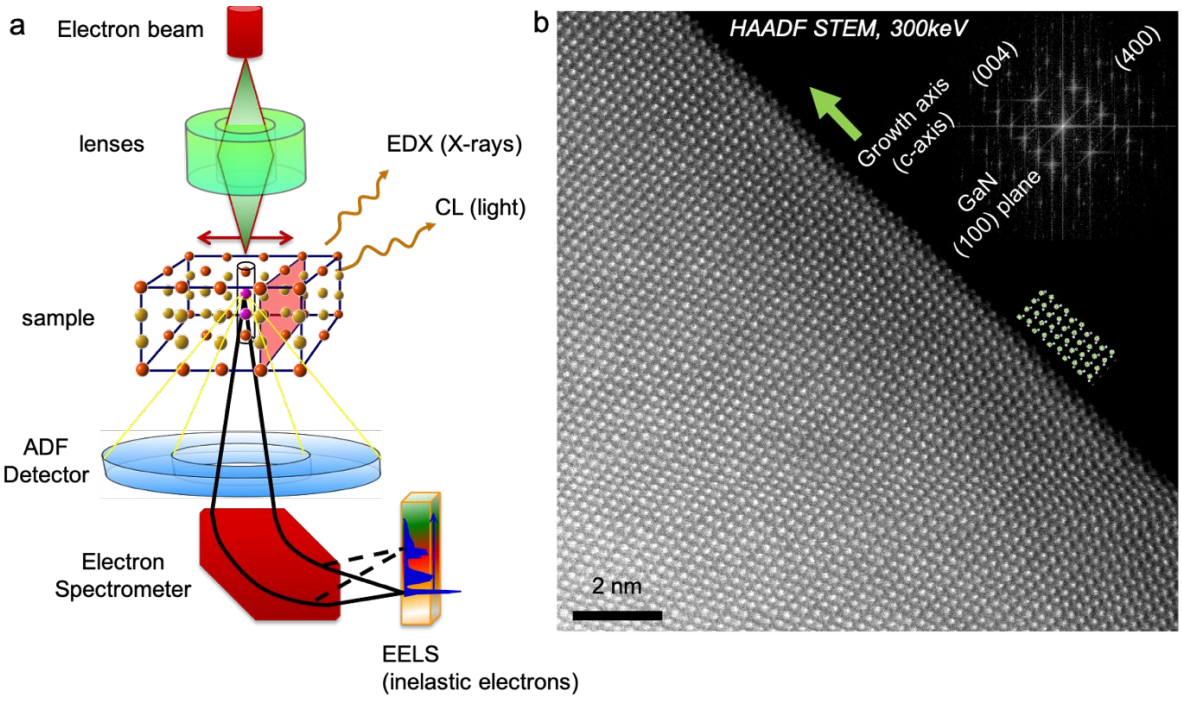

Figure 1.4 Analytic imaging of STEM and examples of Z-contrast. **a** A conceptual scheme of STEM. [inspired by unpublished slides by D.A. Muller] **b** High-angle annular dark-field (HAADF) STEM image of GaN nanowire.

In STEM, when a focused beam of electrons passes through a specimen, they interact strongly with atoms by elastic and inelastic scattering processes (Fig. 1.4). In quantum electrodynamics that accurately describes all phenomena involving electrically charged particles interacting by means of exchange of photons[44], electrons scattering with a charged particle is explained by the differential cross section that describes angular distribution of incident electrons scattered by the Coulomb potential of a charged nucleus of fixed atom[45]. Electrons scatter to higher angles more strongly off heavier atoms than lighter atoms. In the limit of Rutherford scattering, it goes as Z^2, so the contrast in the image will vary approximately as Z^2 [41-43]. Since electrons scattered to higher angles are dependent on atomic number (Z), when an annular detector collects the electrons that scatter to high angles. It provides atomic resolution images where the contrast of an atomic column is directly related to Z.

Electrons from the probe that are scattered inelastically can be collected to provide a spectroscopic signal containing information about atomic bonding and electronic structure—a technique known as electron energy-loss spectroscopy (EELS) technique[46] (Fig. 1.5). When an incident electron scatters with core-shell electron, the electron inelastically scatters and loses its energy by the amount of the core-shell electron's ionization energy (E_c). This ionization energy is uniquely defined for each element because it is a function of the specific atom and the specific electron shell[42,45]. When we collect this characteristic signal, 'ionization edges' appear in energy loss spectrum and we can identify the chemical species or ionization states.

Therefore, the energy lost by the incident electron similarly reflects the distribution of the unfilled states[47-49]. The energy distribution of the unoccupied states has various features and

details (the electronic structure) that appear as fine structures on the ionization edge, called the energy-loss near edge structure (ELNES). The ELNES is said to measure a site- and symmetry-projected unoccupied density of states (DOS) and can give us information about the optical, electronic and mechanical properties of materials[49]. The inelastic scattering is concentrated within smaller scattering angles, and the excitation of energy states results in energy losses[42,45].

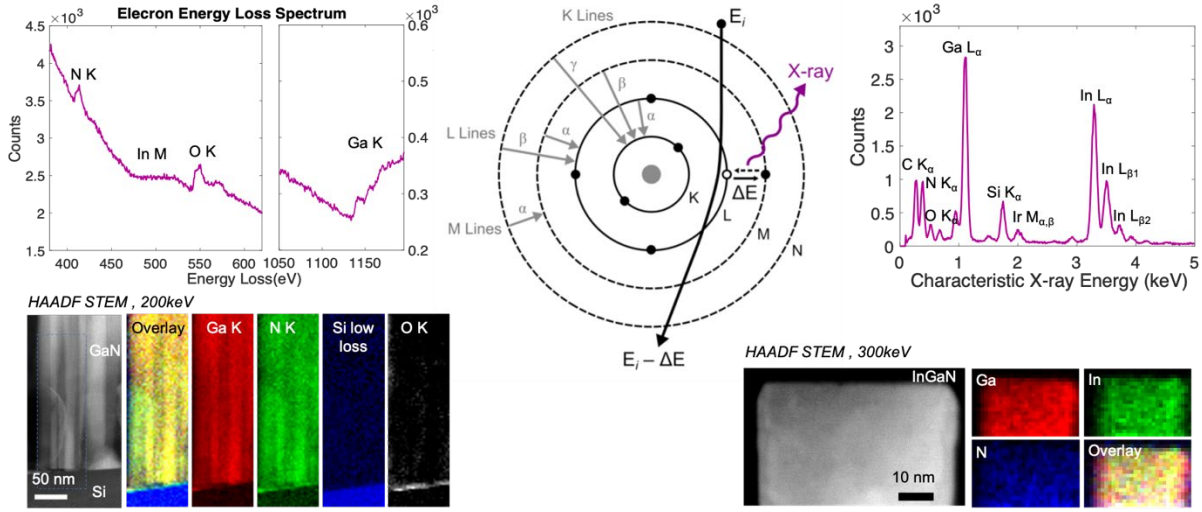

Figure 1.5 Example of analytic spectroscopic imaging[50]. **a** EELS spectroscopic mapping of the GaN nanowires grown on Si substrate interface. **b** X-ray EDS spectroscopic mapping of the 1D InGaN nano-ridge structure [Electron shell model adapted from Egerton et al. Ref. 50].

The inner-shell ionizations result in edge-shaped structures in EELS spectra which can be useful for detecting the elemental components of a material at high resolution. Because the inelastically scattered electrons are concentrated in small angles, a large fraction of the inner-shell ionizations can be collected by the spectrometer[42,45]. When the thickness of the specimen is larger than plasmon mean free path (i.e., $t/\lambda_p > 1$ where t is thickness and λ_p is plasmon mean free path), the EELS spectra, however, is hindered by multiple plasmon scattering which are less localized than elastic scattering limiting to achieve high resolution spectroscopic imaging. Ideally, specimens should be thinner than their plasmon mean free path (λ_p = 106 nm for

amorphous carbon and λ_p = 129 nm for indium, respectively) to identify individual at atom positions, atomic species and local bonding properties combining with sub-angstrom electron-probe[41-43,50]. Multiple-scattering effects have to be considered as the specimen thickness increases[42,45].

The number and energy of the X-rays emitted from a specimen can be measured by an energy-dispersive spectrometer. The incident beam excites an electron in an inner shell, ejecting it from the shell while creating an electron hole where the electron was. An electron from an outer, higher-energy shell then fills the hole, and the difference in energy between the higher-energy shell and the lower energy shell can be released in the form of an X-ray. As the energies of the X-rays are characteristic of the difference in energy between the two shells and of the atomic structure of the emitting element, energy dispersive spectroscopy (EDS) allows the elemental composition of the specimen to be measured[51].

While 2D Z-contrast images are formed by a high-angle annular detector, spectroscopic mapping by EDS or EELS can be obtained simultaneously (Fig. 1.4). Directly interpretable Z-contrast imaging combined with simultaneous spectroscopy and enhanced signal enable to see atoms with unprecedented clarity and map the chemical composition of specimen[43].

1.2.2. In situ TEM Indentation

In situ TEM indentation is a great technique to discover mechanical behavior of materials. Unlike conventional indentation techniques that primarily measure a bulk specimen on the microscale, in situ TEM indentation provides high-resolution load and displacement measurements. A small indentation tip allows to measure on a small area of the thin cross-sectional TEM specimen and records small changes of load and displacement through the

voltage applied to a piezoelectric eleements. High frames rate camera such as Gatan OneView collect a frame ranging from 4096 x 4096 pixels at 25 fps to 512 x 512 pixels at 300 fps because it detects single electrons with highest signal-to-noise ratio using the most sensitive scintillator and fiber optics available. Thus, in situ TEM indentation combined with the camera captures the delicate strain propagation in real time with high-resolution load-displacement curve. Using EELS spectra, one can estimate sample thickness, derives stress, and quantify the amount of mechanical energy the system absorbs. A wide area for indentation is necessary to get reproducible data. Thus we used wedge polishing that give me a-millimeter-wide area for lots of indentation. All these techniques were applied to find nanomechanics that govern nacre.

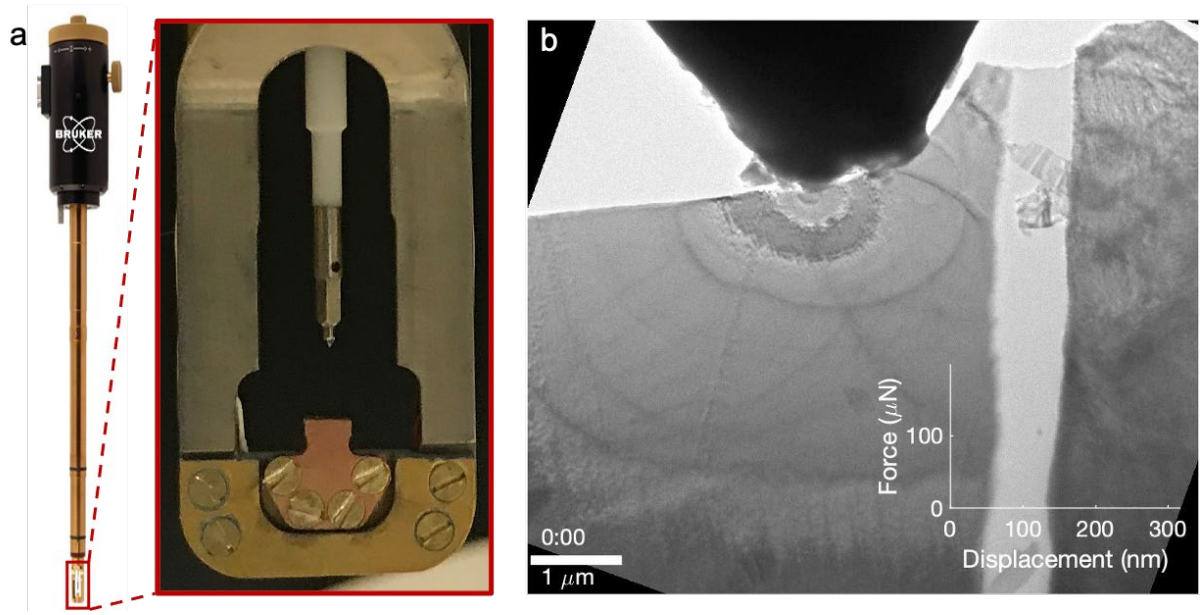

Figure 1.6 In situ TEM indentation. **a** Hysitron PI 95 TEM PicoIndentor. Capacitive transducer, comprising an electrostatic load generator and a capacitive displacement (depth) sensor allows precise measurement of load and displacement. **b** High frames rate camera such as Gatan OneView captures delicate strain propagation in real-time because it can detect single electron with highest signal-to noise using the most sensitive scintillator and fiber optics available.

CHAPTER II

Nano-mechanics in Nacre of Pinna Nobilis Shells

The combination of soft nanoscale organic components with inorganic nanograins hierarchically designed by natural organisms results in highly ductile structural materials that can withstand mechanical impact and exhibit high resilience on the macro- and nano-scale. Our investigation of nacre deformation reveals the underlying nanomechanics that govern the structural resilience and absorption of mechanical energy. Using high-resolution scanning / transmission electron microscopy combined with in-situ indentation, we observe nanoscale recovery of heavily deformed nacre that restores its mechanical strength on external stimuli up to 80% of its yield strength. Under compression, nacre undergoes deformation of nanograins and non-destructive locking across organic interfaces such that adjacent inorganic tablets structurally join. The locked tablets respond to strain as a continuous material, yet the organic boundaries between them still restrict crack propagation. Remarkably, the completely locked interface recovers its original morphology without any noticeable deformation after compressive contact stresses as large as 1.2 GPa.

2.1. Introduction

The inherent tradeoff between strength and toughness inspires new design approaches to structural materials with high damage tolerance. While plastic deformation degrades materials' strength and performance lifetime, it is the key attribute for toughness and resistance

to fracture. Thus, overcoming the tradeoff between toughness, strength, and resilience remains a fundamental design challenge for structural materials[28]. Optimizing mechanical properties for predictable and non-catastrophic failure motivates novel design of modern high-performance structural materials[52,53]. Nature has optimized high-performance materials with unrivaled strength, toughness, and resilience using 3D hierarchical architectures that traverse the atomic, nano-, micro-, to macro-scale with precision that human technology is yet to achieve[14].

Among the diverse set of structural biominerals—such as bone[17], enamel[18], and various biosilica[27]—to be mimicked for designing new synthetic structural materials, nacre is the prototypical supermaterial[28,17,24,29,30]. After crack initiation, bulk nacre shows a 40-fold higher fracture toughness than the monolithic/single crystal calcium carbonate from which it is constructed[17,32-34,54]. Thus, a central focus has been placed on understanding the principal mechanisms of nacre's excellent mechanical properties to inspire new designs of next-generation high-performance structural materials[17,33,34,54-62]. However, nacre's ability to undergo limited deformation and dissipate critical stresses before fracture has not yet been quantified nor correlated with nanomechanical processes. Nacre tablets have a textured surface roughness and internal substructure that are both derived from space filling nano-granules[63-67]. The surface contains nano-asperities suspected to play an important role in the prevention of tablet sliding[68]. Surface asperities between opposing nacre tablets occasionally form narrow (20-50 nm) intrinsic mineral bridges[69] without external stress (Fig. 2.1) connecting across the interlamellar membrane, while wider (150-200 nm) major intrinsic mineral bridges are thought to be involved in the initial formation of new nacre tablets[70,71].

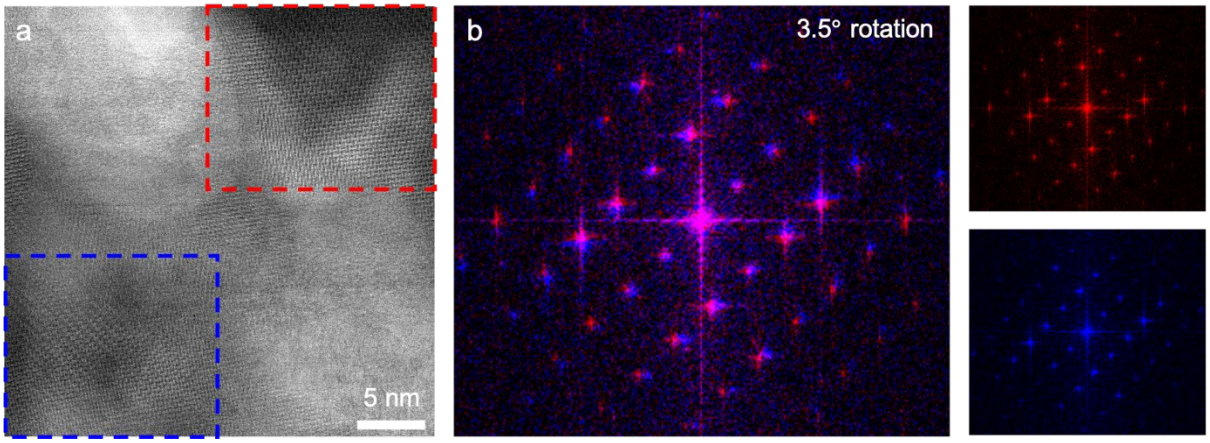

Figure 2.1 Shared crystal orientation between two adjacent nacre tablets. **a** Cross-sectional bright field STEM of a minor connection i.e., intrinsic mineral bridge structure without external stress spanning across the interlamellar membrane showing continuous crystal growth between tablets. **b** Fast Fourier Transformation of (a) showing a twist angle of 3.5 degrees between the crystallographic orientations of the tablets. This could suggest continuous growth of the tablets from one layer to the next through intrinsic bridges, noted as a possible nacre growth mechanism.

In nacre, U. Wegst et al.[24] have suggested that crack bridging and the resulting 'pull-out' of mineral bricks is associated with controlled, yet limited, sliding of the aragonite layers over each other and is aided by visco-plastic energy dissipation in the organic layer. X. Li et al observed the plastic deformation of aragonite surfaces under tensile load at the nanometer level using atomic force microscopy (AFM)[58,61]. However, additional mechanisms for strengthening and toughening have been proposed: resistance from the lamellae nanoroughness[59], the organic layer acting as a viscoelastic glue[27,56,60,62], the presence of (pre-existing) mineral bridges[34,57,72], and platelet interlocking at the microscopic level[62]. Direct observation is required to disambiguate the mechanism of nanomechanical deformation of nacre; however, most knowledge of the biomineral toughening process is assembled from microscale tribology[29,33,55,56], tensile[17,33,55,59,60,62,73], or compression[54,59,74] testing on bulk specimens. Understanding nanomechanical responses across the 3D hierarchical architectures is critical to understanding how the individual nacre components work together to create properties greater than the sum of their parts (i.e. far exceeding the rule of mixtures[24]).

Our investigation of toughening strategies in nacre reveals nanomechanical deformation of organic interfaces, nanocrystallites, and organic inclusions as key to the increased damage-tolerance of nacre. High-resolution S/TEM combined with in-situ nano-indentation[75,76] has been adapted to biomineral systems to allow sub-nanometer resolution imaging of the nanomechanical deformation processes and provide precise assessment of when and where fracture occurs. We show that during compressive indentation nacre undergoes non-destructive locking where inorganic tablets come into contact across organic interfaces (Fig. 2.2). Remarkably, the completely locked interface recovers its original morphology without any deformation after releasing compression and retains its full mechanical strength. During compression, the aragonite grains and organic inclusions reversibly rotate and deform indicating nanoscale resilience of the nacre tablets. Prior to tablet locking, strain attenuates up to 80% between the decoupled tablets. However, by 3% engineering strain of the first tablet, the tablets have locked to redistribute stress continuously across the organic interface and the strain attenuation decreases.

When fracture occurs, we show the organic components restrict crack propagation both within and between tablets, sustaining the overall macroscale architecture through multiple fractures to allow further structural loading. This allows nacre to absorb significantly greater mechanical energy than monolithic aragonite. We report that nacre absorbs roughly 1-3 times more mechanical energy than geological (i.e. non-biogenic) monolithic aragonite before fracture results in structural failure under nanoindentation. This approach provides an energy dissipation measurement that is not derived from a crack-propagating force. In addition, we show that the yield strength measured under nanoscale compression along the c-axis (growth direction) of a single tablet can reach values three times higher (e.g. ~1.1-1.6 GPa) than

previously reported for bulk nacre measured with micro-indentation[17,28,34,54-56,68,74,77,78].

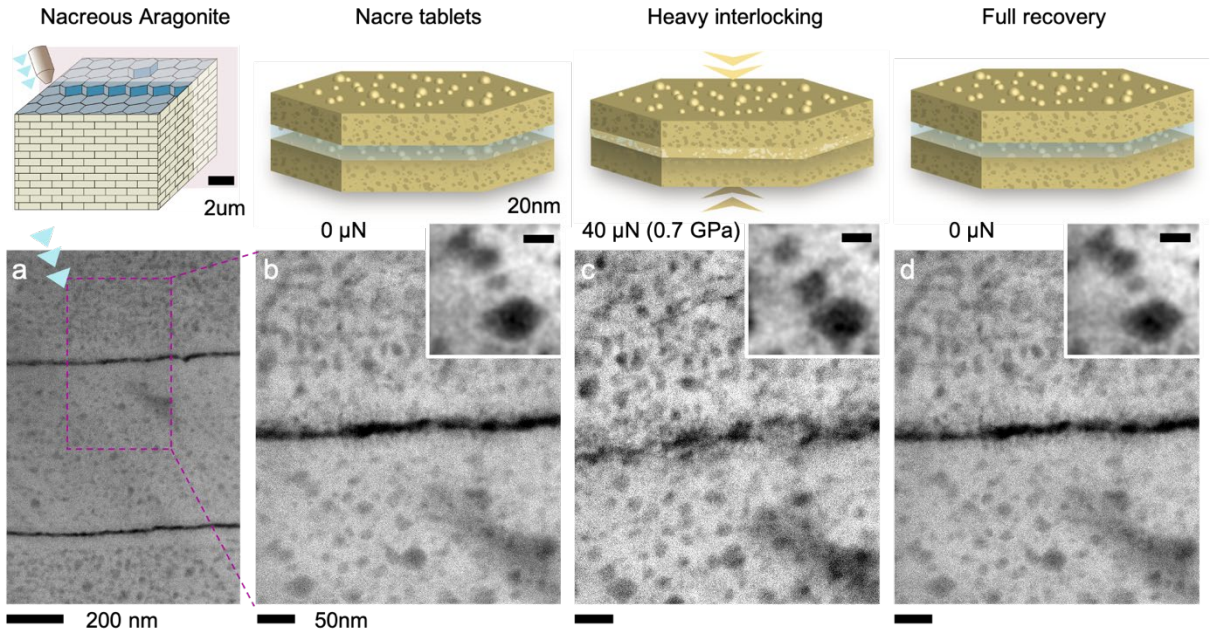

Figure 2.2 Highly deformed and recovered nacre[1]. **a** HAADF STEM overview image of cross-sectional interface of nacre tablets before compression. **b** High-resolution STEM image of two tablets and their organic interface before compression. **c** Tablets heavily interlocked under 40 μN compressive load. **d** After indenter is retracted, tablets and organic interface have fully recovered their initial morphology. Insets show the movement of organic inclusions due to the deformation of the tablet and their complete recovery after removing the compressive load [J.Gim et al. Ref. 1].

2.2. Materials and Methods

2.2.1. Specimen and Sample Preparation

Specimens of the protected Mediterranean *P. nobilis* (*Pinnidae*, Linnaeus 1758) bivalve species were live collected in the bay of Villefranche-sur-Mer, Département Alpes-Maritimes, France (Fig. 1.2a). All necessary permits were acquired from DDTM (Direction Départementale des Territoires et de la Mer) of Alpes-Maritimes department. *P. nobilis* is strongly protected by a European Directive (92/43/CEE). Specimens of the geological monolithic aragonite were mined in Sefrou, Morocco (Fig. 1.2c).

After the bivalves were sacrificed, small shell sections were cut from the whole shell

measuring 60 cm shell hight[64] using a diamond wire saw. To avoid beam damage and amorphization from ion beam milling, cross-sections for S/TEM were prepared by mechanical wedge polishing[64] (See Appendix B for details). This technique provided large-area, electron-transparent specimens with structural stability critical for nanotribology. Nacre samples had thicknesses of 124 nm ± 3 nm (Fig. 2.13a-c), 98 nm ± 2 nm (Fig. 2.9a), prismatic calcite had a thickness of 102 nm ± 6 nm (Fig. 2.13d-f), monolithic aragonite had a thickness of 169 nm ± 1 nm (Fig. 2.13g-i).

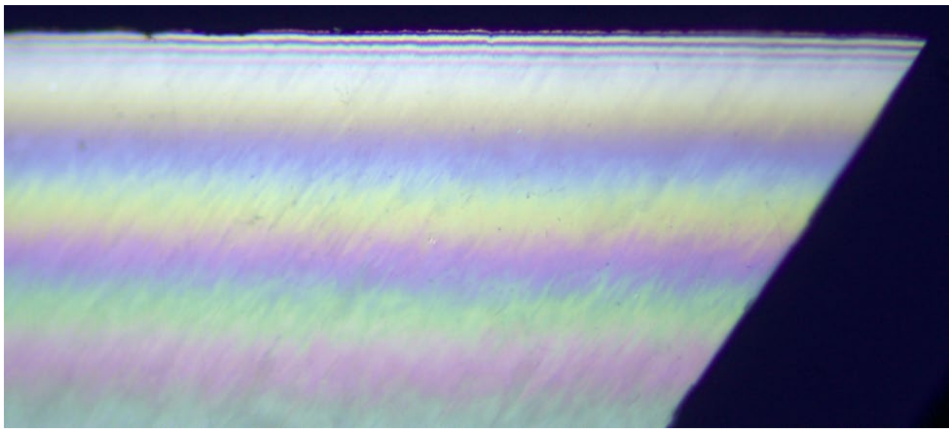

Figure 2.3 Wedge polished specimen of nacre in *Pinna Nobillis* mollusk shell.

2.2.2. Electron Microscopy

Real-time observation of the compressive nano-deformation was performed using S/TEM. Column pressure in the TEM column at the specimen was ~1×10^7 torr. Bright field transmission electron microscopy with 60 μm (for nacre) and 120 μm (for biogenic prismatic calcite) apertures provided contrast of strain contours and performed on a 200 keV JEOL 2010F and Gatan OneView camera enabling frame rates of up to 200 frames per second. Images were captured at 50 frames (2048 × 2048 pixels) per second for nacre, and at 12.5 frames (2048 × 2048 pixels) per second for biogenic prismatic calcite and monolithic aragonite. STEM was

performed using a JEOL 3100R05 microscope with Cs aberration corrected STEM (300 keV, 22 mrad) and cold field emission gun. A HAADF detector with 120–150 mm camera lengths and a detector angle of 59~74 (inner) – 200 mrad (outer) were used to produce Z-contrast images where greyscale intensity is sensitive to the atomic number in the specimen's matrix.

No change was observed in mechanical behavior measurements with beam exposure: whether the beam was blanked, or the microscope was operated in low-dose STEM or TEM mode. Low-dose methods, beam shuttering, and examination of regions exposed to the beam were used to separate electron beam irradiation from intrinsic phenomena. For STEM measurements, with a typical field of view of 500 nm the electron dose was typically ~150 e^{-}·Å^-2 and dose rates around ~4 e^{-}·Å^-2·s^-1 the material was structurally preserved during imaging. However, for the same imaging conditions at higher magnifications (e.g. 30 nm field of view) the radiation dose increases to ~$2 \cdot 10^5$ $e^{-}/Å^2$ and dose rate to ~10^3 e^{-}·Å^-2·s^-1 which causes the material to show electron irradiation damage localized to the small field of view. Thus, larger fields of view are preferred to minimize dose and provide a large area of observation where fracture may nucleate. Atomic resolution STEM requires a small field of view, on-axis region of interest, and a static specimen which was not achievable during in-situ nanoindentation. This limits atomic imaging during nanoindentation despite the well-aligned instrument's probe limited resolution of ~1Å. For TEM imaging, dose was minimized through use of a heavily diverged beam and a high-efficiency camera (DQE of 0.3) with single electron sensitivity and high-readout speed (up to 300 fps).

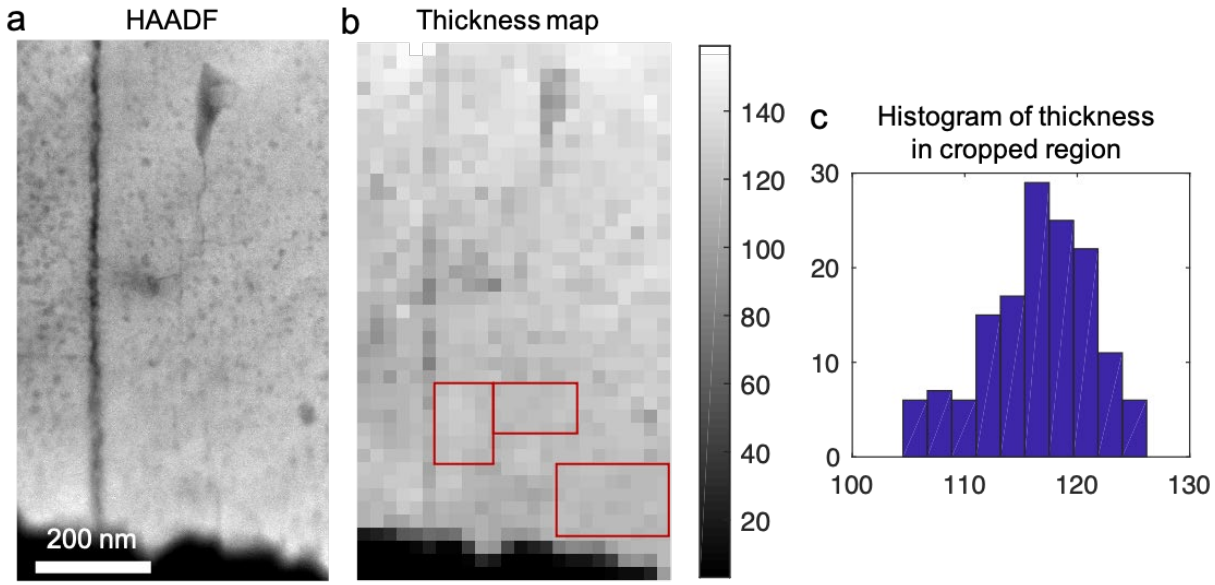

Figure 2.4 Measurement of the local thickness t of the indented nacre tablets using EELS. **a** HAADF-STEM showing the overview of the nacreous tablet adjacent to the indented nacre. **b** Thickness map in the same region in a. Thickness is determined by plural scattering in an electron energy loss spectrum (See, methods). **c** Histogram of the estimated thickness in cropped region showing 115 ± 2 nm of average thickness. $CaCO_3$-rich region is accounted for thickness because the plural scattering is mostly contributed by $CaCO_3$.

Low-loss electron energy loss spectra (EELS) were acquired at 300 kV with a Gatan Quantum Energy Filter, with 1.5 eV per channel to determine thickness of the specimen. The convergence semi-angle was 22 mrad and the collection semi-angle was approximately 40 mrad. Linear combination of power laws (LCPL) with local background averaging (LBA) was applied to analyze the spectrum image using the Cornell Spectrum Imager[79]. Thickness of the specimen is determined from plural scattering in an electron energy loss spectrum, which is defined by $I_0 = I_{\mathrm{ZLP}} \cdot e^{-\frac{t}{\lambda}}$ where I_0 is total plural scattering in electron-loss spectrum, I_{ZLP} is zero loss peak in the spectrum, t is the thickness of the nacre, and λ is the wavelength of the incident electron beam, as described in Egerton[50]. Relative organic concentration in nacre tablet was formulated by ratio of high-angle elastic electron scattering intensity, which is defined by $I_{\mathrm{HAADF}} = t \cdot \sum Z_x^{\gamma} \cdot \rho$ where I_{HAADF} is the high-angle annular dark field intensity, t is the thickness of the nacre, x is a certain element in $CaCO_3$ or organic molecule, γ is elastic

scattering cross-section ranging from 1.4 to 1.7 and ρ is the $CaCO_3$ or organic molecular density (Fig. 2.5).

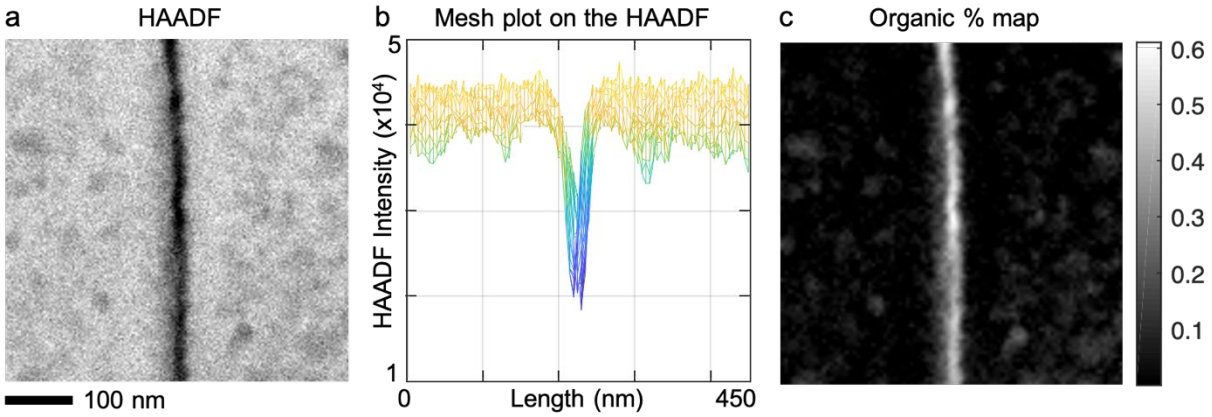

Figure 2.5 Relative organic concentration in nacre tablets using ratio of high-angle elastic electron scattering intensity. **a** HAADF-STEM showing the overview of the nacreous tablet. The region of interest is cropped with a area of 500 nm by 500 nm, which is equivalent to the width of a nacre tablet width. **b** Mesh plot on HAADF image in a showing the region interest has little thickness variation. **c** Relative organic component concentration map on the region in a. Organic materials occupies 6.1 % of nacre (2.6 % for interlamellar and 3.1 % for interorganic).

2.2.3. In-situ Nanoindentation and Triboindentation

Nanoindentation experiments were conducted in the TEM column (~25 ℃, 10^{-6} Torr) using a Hysitron PI-85 PicoIndentor. Load-controlled nanoindentation was performed using cube corner (tip radius = ~0.1 μm, half-angle = 35.26°, included angle = 90°) and conospherical (tip radius = ~1 μm, semi-angle = 60°) diamond probe tips. Maximum loads varied from 10 to 400 μN. A piezoelectric actuator controlled the specimen position in all three dimensions. During indentation the indenter was advanced at a rate of 5 nm/s for nacreous aragonite and prismatic calcite and at a rate of 60 nm/s for monolithic aragonite. Force–displacement information and movies were recorded during indentation, and still TEM micrographs were collected between tests. The electrostatic force constant of the transducer was calibrated such that the root-mean-square error fell below ~ 10^{-5} $\mu N/V^2$ using Z-axis calibration, which results in the measurement error in force and displacement within ± 5%. The top surface of the tip was

aligned vertically to the cross-sectional nacre specimen to achieve uniaxial compression without shear or bending. For all the samples, contact stress is calculated through dividing the measured load by cross-sectional area of the specimen in contact with the indenter tip. This contact area is estimated by multiplying the length of the contact region measured in real-time with S/TEM images and the specimen cross-sectional thickness measured by the ratio of zero loss / total low loss electron energy loss spectrum captured with EELS. Total error of contact stress is calculated by a quadrature of the errors from the contact length measured by human vision (± 10%), the specimen thickness estimated by EELS spectrum image (± 11%), and the load reported by the nanoindentation software (± 5%). The contact area changes through series of indentations (Fig. 3) due to stage drift (typically 20 - 60 nm). Toughness (J/m^2) is defined as the absorbed mechanical energy, which can be bounded by integrating the stress-displacement curve to find the energy absorbed per unit area (Fig. 4j). The tablet engineering strain along the c-axis is defined as the ratio of the reduction of the tablet width (that is, compressive deformation directly under the region of loading) to its initial width (Fig. 2.6). Strain attenuation is defined as the ratio of the measured tablet engineering strain between the first and the second tablet from the indenter tip contact location (Fig. 2.6).

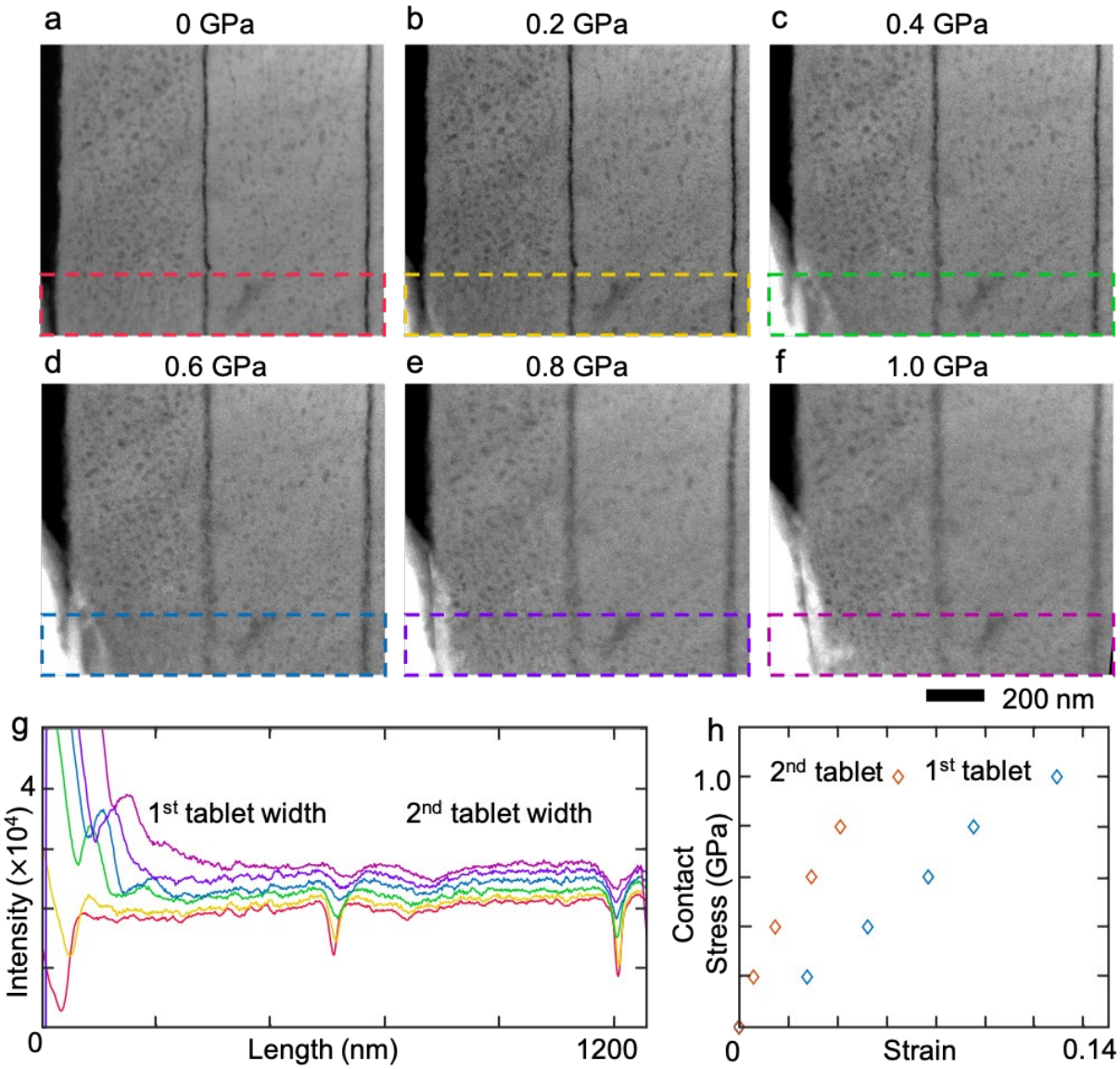

Figure 2.6 Strain attenuation from 1st to 2nd tablet from indenter tip. **a-f** HAADF-STEM images showing nacreous tablet compressed from 0 GPa to 1.0 GPa. **g** HAADF intensity profiles of the cropped area in a-f showing the gradual reduction of the tablet width. **h** Contact stress-tablet engineering strain curve plotted based on the ratio of 1st and 2nd tablet width measured in g.

Triboindentation experiments were carried out on bulk biological aragonite, calcite and geological aragonite samples (5 mm × 5 mm area, 3 mm thick) with polished surfaces to determine the elastic modulus of the materials using a Hysitron TI-950 Triboindenter. During indentation the indenter was advanced at a rate of 20 nm/s for nacre, prismatic calcite and monolithic aragonite with a Berkovich tip (i.e. three-sided pyramidal diamond tip). The probe

area function was calibrated for the Berkovich tip, particularly in the low depth ranges using a standard quartz sample before determining the mechanical properties accurately. To validate the tip calibration, a standard Al single-crystal was used to confirm our calibration values match the elastic modulus and hardness (69.6 ± 10% GPa and 9.25 ± 10% GPa) provided by the manufacturer within a standard deviation of 5% using the standard Oliver-Pharr method.

2.3. Results

2.3.1. Nanoscale Deformation and Toughening Processes

We observe non-linear elastic nanoscale deformation and toughening processes in nacre under compression using nano-indentation with 0.04 - 0.2 μm^2 contact areas approximately normal to the growth direction (c-axis). This surface normal is nacre's strongest direction[33,34,68], although the monolithic aragonite from which it is comprised is stiffer along the planar direction[80]. Electron transparent cross-sections from a mature *P. nobilis* specimen (Fig. 2.1a) provided the structural stability required for indentation while allowing sub-nanometer resolution imaging (see methods). S/TEM observation revealed a range of strengthening and toughening processes enabled by nacre's hierarchical structure: (i) tablet interlocking, (ii) strain damping, (iii) crack blunting, and (iv) intracrystalline deformation and rotation of nanograins and organics. Despite comprising only a few weight percent (i.e. ~2 to 5 wt. %[56,59,60,71,72,77,81,82]) of the entire nacre architecture, the organic components of nacre provide a range of functions that absorb the energy of applied loads while remaining highly recoverable even after initial fracture. The ratio of HAADF STEM intensity estimates the total organic volume fraction in *P. nobilis* nacre to be 7.1 ± 2.2 vol. % (3.4 ± 1.0 wt. %) comprised of 2.5 ± 0.3 vol. % (1.2 ± 0.1 wt. %) interlamellar and 4.6 ± 1.9 vol. % (2.2 ± 0.9 wt. %) intracrystalline material (Fig. 2.5).

2.3.2. Highly Recoverable Nacre Tablet Locking

Nacre's nanoscale organic boundaries and inclusions allow heavily deformed nacre to fully recover its original morphology on the nanoscale (Fig. 2.3). Under large compressive loads (e.g. 0.7 GPa in Fig. 2.3c), opposing nacre tablets interlock across the mineral-organic interface to form temporary inorganic connections through the joining of asperities. Further, the entire tablet volume compresses resulting in small but discernable deformation of organic inclusions (Fig. 2.3). After releasing the load, the mineral connections at the deformed organic interface and the intratablet nanostructure perfectly recover their initial morphology without any sustained deformation (Fig. 2.3e). This remarkable recovery after tablet locking was reproduced and observed across all areas of interest (Fig. 2.5).

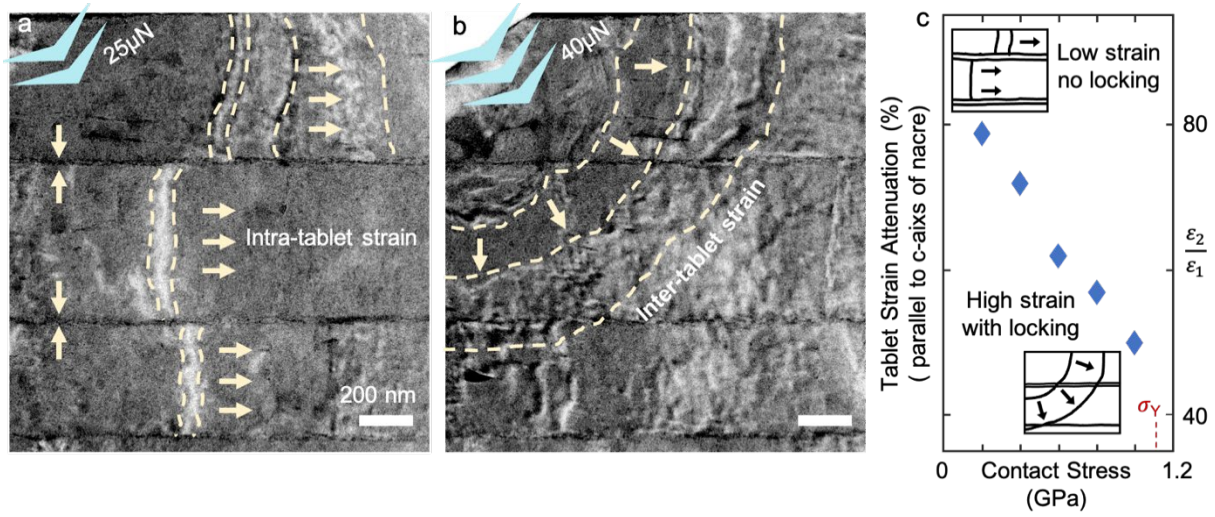

Figure 2.7 Strain propagation confined by organic interfaces[1]. **a-b** Bright field TEM (with contrast inverted) on the cross-sectional nacreous region under low and high compressive contact stresses. Under low compressive stress, intra-tablet strain contours are generated, and strain propagates independently along each tablet. As the compressive stress is increased, nacre tablets interlock and larger inter-tablet strain contours propagate diagonally between tablets. **c** Tablet strain attenuation along the axis of the indentation source. The linear strain dissipation behavior indicates that the deformability of nacre is weakened as the applied stress is increased. Scale bar 200 nm [J.Gim et al. Ref. 1].

Nacre shows mechanical response regimes of high and low compression visible in the strain contours measured during in-situ TEM indentation (Fig. 2.7). Low compressive loads

applied along the growth direction generate strain contours which propagate transversely within each tablet (Fig. 2.7a). Shearing of the interlamellar membranes prevent propagation longitudinally to neighboring tablets. At higher loads, tablets couple, coming into direct contact with one another and allowing strain contours to spread across tablets radially from the location of indentation (Fig. 2.7b).

Strain along the c-axis is highest directly below the tip loading and tablet compression (tablet engineering strain) is measurable using interlamellar demarcation (Fig. 2.6). By ~3% engineering strain in the first tablet, the contours redistribute continuously and by ~6% engineering strain, locking is strikingly visible between tablets. Initially, the engineering strain of the first to second tablet along the axis of indentation decreases by over ~80% when measured using a 0.1 um^2 contact area. This measurement is only one component of an inhomogeneous strain field that on-average, dissipates away from the point of compression. As greater contact stress is applied, the tablets increasingly lock farther away from the tip and the strain attenuation linearly decreases—the deformability is reduced as the nacre behaves more like a monolithic material (Fig. 2.7c). This entire process occurs with elastic processes that are fully repeatable.

We note, tablets also exhibit a limited amount of locking for indentation parallel to the tablet plane (Fig. 2.8). This occurred near the indentation tip where stress is high, and the Poisson effect pushes the compressed tablet against its neighbors. Further away, unlocked tablets accommodate shear deformability at their interface and strain contours are discontinuous. Indentation parallel to the tablet plane was less resilient and typically resulted in unrecoverable brittle fracture (Fig. 2.8).

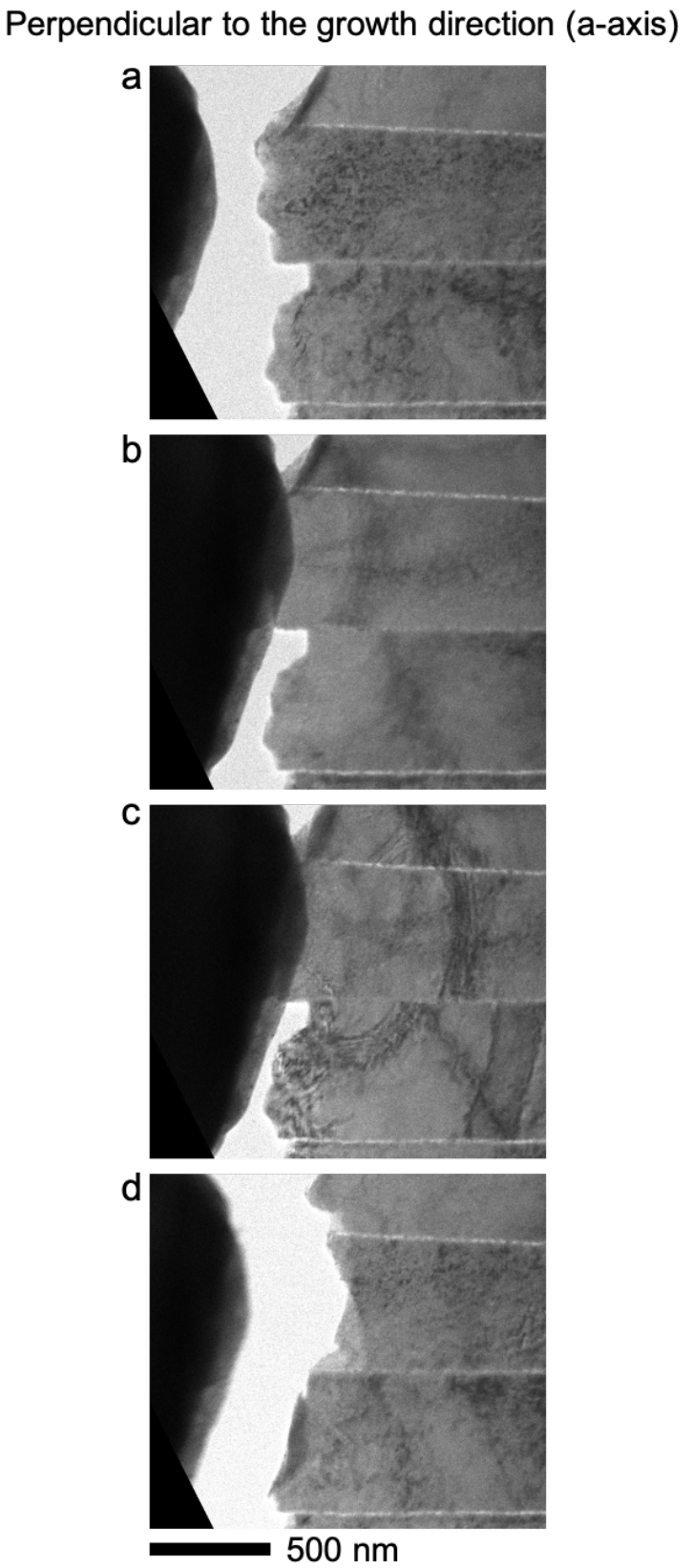

Figure 2.8 In situ TEM nanoindentation along a-axis of nacre tablets. **a-d** Compression parallel to the tablet plane showing a limited amount of locking at interface before fracture.

2.3.3. Preservation of Mechanical Strength

During consecutive indentation tests, highly deformed nacre fully recovers under external loads up to ~80% of its yield contact stress. This can be seen in Figure 2.9a, where the elastic modulus remains unchanged during eight-consecutive compressions (blue and red). As shown in the specimen of Figure 2.9d-e, beyond ~0.8 GPa, nacre begins non-linear elastic deformation—yield is visible from the decreasing slope of the contact stress-displacement curve. However, unlike traditional plastic deformation, the initial structure is preserved after unloading. Full recovery was even observed in highly deformed nacre (e.g. above ~0.8-1.1 GPa) prior to crack formation (Fig. 2.3 and 2.11). This preservation of mechanical strength under repeated loading/unloading cycles reflects a non-linear elastic deformation process featuring nanomechanical resilience not present in traditional bulk materials, attributable at least in part to tablet interlocking.

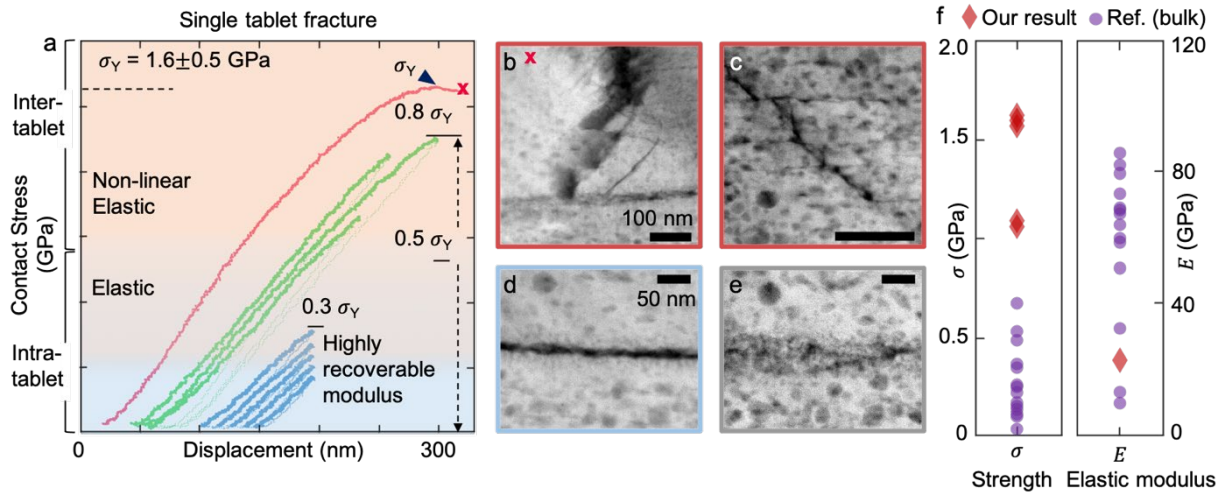

Figure 2.9 Recoverable mechanical strength of nacre and crack blunting within and between tablets[1]. **a** Nine consecutive in situ TEM compression tests on the same nacreous tablet. Three different colors correspond to different contact areas during the series of the compressions. Stage drift caused changes to contact area between indentations. **b** ADF STEM images after the series of the indentation tests showing a crack blunted by an organic boundary. **c** ADF STEM image shows crack formed within tablet and blunted by an organic inclusion. **d, e** ADF STEM images of Nacre tablet compressed by 47 μN (55% of σ_{Yield}), corresponding to the non-linear elastic regime, structure remains fully recoverable—after deformation nacre still preserves both its initial strength and structure. **f** Strength and elastic modulus of nacre from contact stress in nanoindentation on the thin cross-sectional specimen in this study and various types of testing – microscale tribology, tensile, compression, and bending– on bulk specimens in previous reports. Scale bar 50 nm [J.Gim et al. Ref. 1].

The rotation and deformation of organic inclusions and nano-granularity has also been predicted as another mechanism for viscoelasticity[61]. Although structurally recoverable locking of tablets is key to nacre's resilience, in the reported nanoindentation experiments, performed under dry conditions, the absorbed energy appears to primarily occur within the resilient deformation of nanograined tablets that constitute a significant volume fraction (~ 97%). This process is confirmed in our bright field TEM data, where individual aragonite nanograins change contrast as nanograins reorient and organic inclusions slightly reshape their volume (Fig. 2.10).

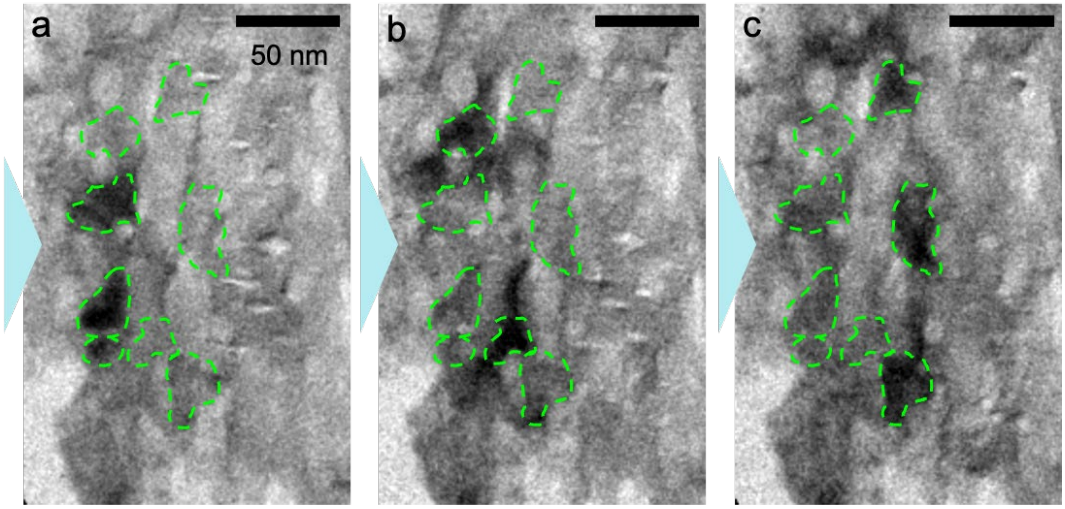

Figure 2.10 Rotation and deformation of aragonite nanograins and organic inclusions in nacre at the nano-scale. **a-c** Bright field TEM of the cross-sectional nacreous region after contact with indenter tip (noted by cyan arrow) and continuous compression of the same region. Darkening of grains corresponds to changes in crystallographic orientation. Notably, the organic inclusions of c) have become rounded in morphology compared to a, b. Here, BF-TEM contrast of the thin specimen is sensitive to strain and small changes in crystallographic orientation. The visible darkening of grains (green circles) during indentation are due to nanograin deformation or reorientation from local stresses.

The deformation of these nanometer scale organic inclusions with compression of the material accommodates the load while avoiding irrevocable damage to the inorganic matrix (Fig. 2.3c-e, also shown in insets of Fig. 2.10 and 2.11). Here, nacre's response shows non-linear elastic deformation distinct from that expected in analogous nanocrystalline metals.

Unlike nano- or micro-grained metals, which strengthen through reduced mobility of dislocations at grain boundaries[83,84], nacre's proteinaceous organic components contain flexible

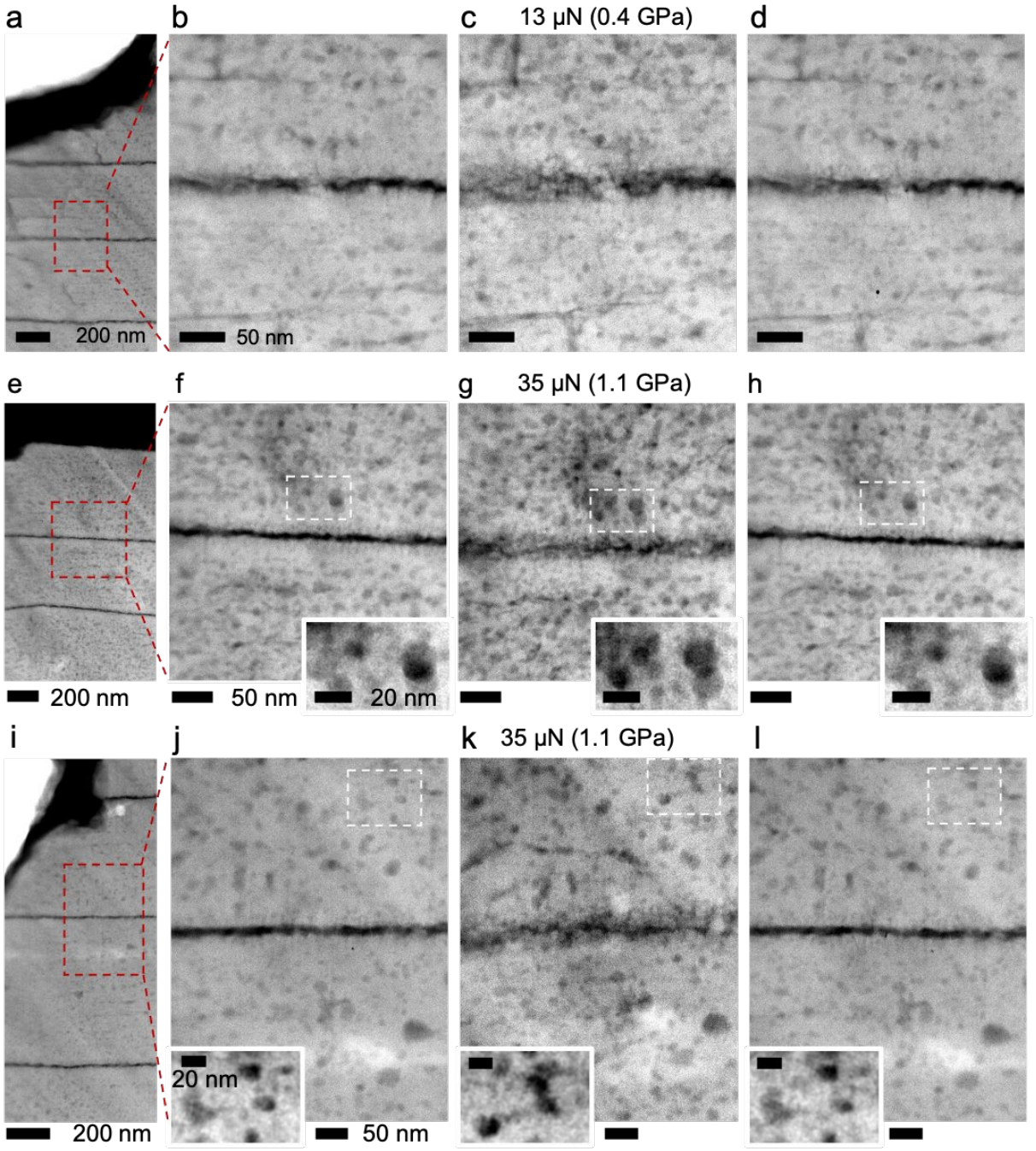

Figure 2.11 Cross-sectional view of nacre deformation and recovery at tablet interfaces using HAADF STEM. **a, e, i** Overview of three different nacre tablets. **b, f, g** The interlamellar membrane between opposite tablets is well defined before compressive nanoindentation. **c, g, k** Upon loading, interface interlocks and temporary inorganic connections form. **d, h, l** After the load is released, the system fully recovers to its initial state. Insets highlight deformation of aragonite grains and organic inclusions as viewed in projection.

molecular bonds that elastically accommodate strain and rotation of nanograins and restoratively return the system to original state when an external stress is released. This process occurs without the introduction of dislocation pile-up and plastic deformation. Energy absorption during protein stretching / unfolding and subsequent energy release upon refolding of the elastomeric molecules provides high resilience in nacre and similar to that found in bone[85]. In contrast, nanocrystalline or nanotwinned metals have lower resilience since they exhibit plasticity via dislocations.

At failure, the organic components in nacre impede crack propagation both within and between tablets (Fig. 2.9b-c, 2.12, and 2.13c). The smaller organic inclusions embedded within the inorganic matrix hinder crack propagation within the tablet and were observed to blunt and deflect cracks (Fig. 2.9c). The interlamellar membrane likewise hampers propagation between tablets, where cracks often terminate or jump at the interface (Fig. 2.9b). After each fracture event, the overall macroscale architecture is preserved and maintains its mechanical properties (Fig. 2.13a-c). This extends the damage tolerance of the superstructure beyond a single fracture. In fracture mechanics[86], the ability to resist fracture is quantified by a fracture toughness when a crack is present. In this complex material local stress states can lead to a variety of mechanisms responsible for the fracture process zone. Here, cracks can be under mixed mode loading conditions, which in general can lead to differences in the energy required for crack extension and make quantification of fracture toughness by nanoindentation challenging. In bulk specimens loaded in mode I, a fracture toughness of 10 $MPa \cdot m^{1/2}$ has been reported for nacre, 40-fold larger than that of single crystal aragonite, ~0.25 $MPa \cdot m^{1/2}$ [54,73].

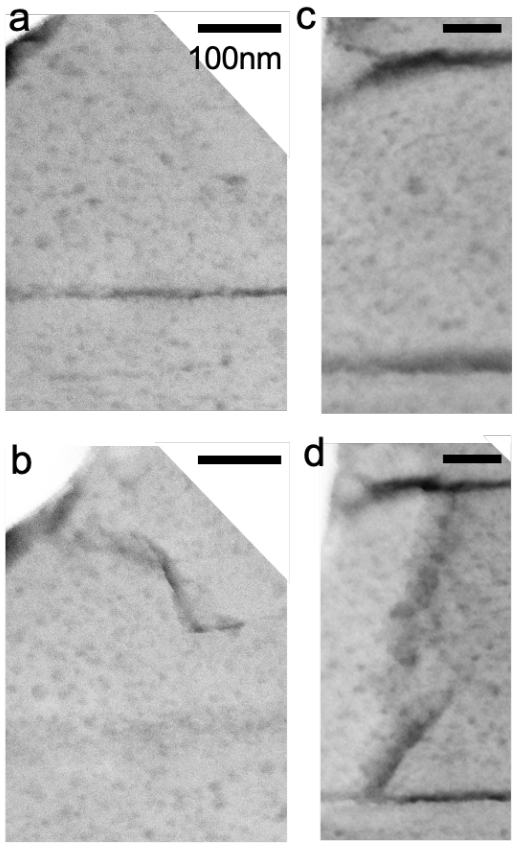

Figure 2.12 Cracks blunted by organic boundaries and inclusions in nacre. **a, c** Nacre structure before compression. After failure cracks propagate and **b** terminate at organic inclusions or **d** terminate at the interlamellar membrane.

2.3.4. Damage-Tolerance of Nacre's Architecture

On a system level, nacre can sustain several fractures before total failure due to its hierarchical soft-hard matter design. This means the yield stress of nacre is not typically defined by crack initiation. In contrast, prismatic calcite and monolithic aragonite exhibits limited deformation before the yield stress is followed by catastrophic failure or crack runaway (Fig. 2.13d-i) from cone cracking at indentation. Monolithic aragonite responds to strain with stress contours radiating from the point of contact. Prismatic calcite from the *P. nobilis* mollusk—behaved similar to monolithic aragonite however indentation near an organic interface showed significant attenuation into an adjacent prism (Fig. 2.13e).

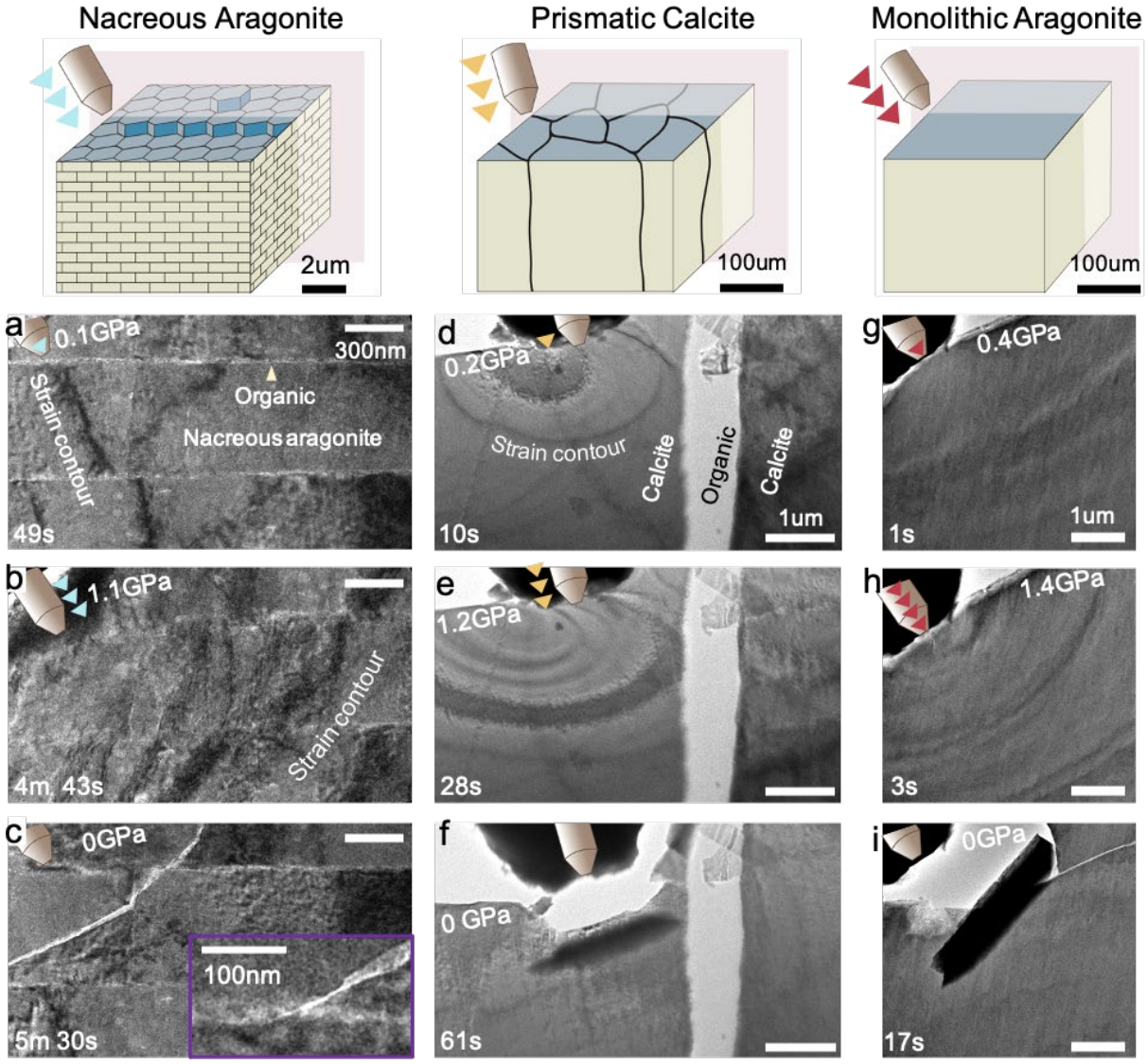

Figure 2.13 Toughening processes of nacre, prismatic calcite, and monolithic aragonite[1]. **a-c** Bright field TEM images of the cross-sectional nacreous region during in situ TEM indentation. The nacreous tablets made contact on the side of the tip (tip diameter: ~100 nm). Inset in (c) shows crack blunting at the organic interface. **d-f** Bright field TEM images of the cross-sectional prismatic calcite region during indentation. **g-i** Bright field TEM images of non-biogenic, monolithic aragonite during indentation [J.Gim et al. Ref. 1].

When compared to monolithic calcite materials, we clearly see nacre's interlamellar membranes reshape compressive strain fields. Both biogenic calcite from the prismatic layer of *P. nobilis* and geological monolithic aragonite were noticeably stiffer than nacre (Fig. 2.14b) and typically reached higher yield stresses than nacre (Fig. 2.14a). However, nacre's inorganic-

organic architecture reliably absorbed 1-3 times more mechanical energy than prismatic calcite and monolithic aragonite before total failure. Integrating the applied stress over the displaced volume of the indenter contact area provides an upper bound on nacre's energy dissipation of 1.1×10^3 J/m^2. Here, nanoindentation provides us with true estimates of the energy required to cause fracture(s) that lead to structural degradation. A typical contact stress-displacement curve for nacre often included several intermediate failures, where cracking was halted, nanoscale morphology of nanograins and organic inclusions was preserved, and nacre could undergo further loading without a noticeable change of structure in its mechanical response. Notably, in calcite and monolithic aragonite crack runaway occasionally allowed noticeable energy absorption—however this occurred after the maximum yield stress and resulted in the unrecoverable structural failure typically found in brittle materials.

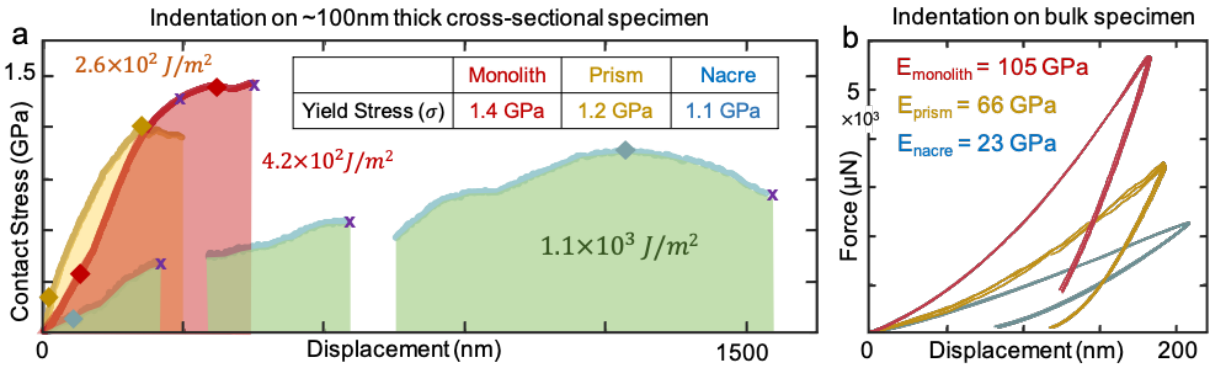

Figure 2.14 External energy absorption of nacre, prismatic calcite, and monolithic aragonite[1]. **a** Correlative compressive contact stress vs. displacement curve showing mechanical response of the nacreous, prismatic, and monolithic region. Stress herein is engineering stress calculated by dividing load by cross-sectional area contacted with tip. Total energy dissipation values (area under contact stress-displacement curves) marked. **b** Triboindentation on bulk specimens of nacre, prismatic calcite, and monolithic aragonite [J.Gim et al. Ref. 1].

In-situ nanoindentation enables mechanical behavior to be measured at the single tablet level, allowing the contributions of the toughening and resilience mechanisms across length scales to be assessed. For instance, while the elastic modulus of nacre and calcite from *P. nobilis* were comparable to previous reports on bulk specimens[54-58,68,77,87-92] (Fig. 2.9f and 2.15), the

measured strength of nano-indented nacre reached values as high as 1.6 ± 0.2 GPa, roughly three times larger than the literature reports for bulk nacre in hydrated and dehydrated specimens[17,28,34,54-56,68,74,77,78]. Dehydrated nacre has been shown to have a greater strength and elastic modulus, but lower toughness than hydrated nacre due to the plasticizing of the organic matrix by water[33]. Here the *Pinna nobilis* specimen was sacrificed and dehydrated. In native conditions, the performance of nacre should be even better, we underestimate the recoverability of nacre under conditions of low-pressure, low-hydration and overestimate its tendency to fracture. Typically, nanoindentation in the thin cross-sectional specimens of the nacre and calcite from *P. nobilis* and geological monolithic aragonite also resulted in a yield strength (e.g. 1.1 $\pm$ 0.1 GPa) larger than previously reported bulk values (Fig. 2.9f and 2.16). The high strength may be attributed to the finite size of the indentation tip and nanoscale size effects of the mechanical response. As previously observed in several materials—including gold nanowires[93], polycrystalline thin films[94], and multiwalled carbon nanotubes[95]—the size effects on mechanical properties of nanostructured materials deviate from bulk and necessitate the use of in-situ nanomechanical testing[96,97].

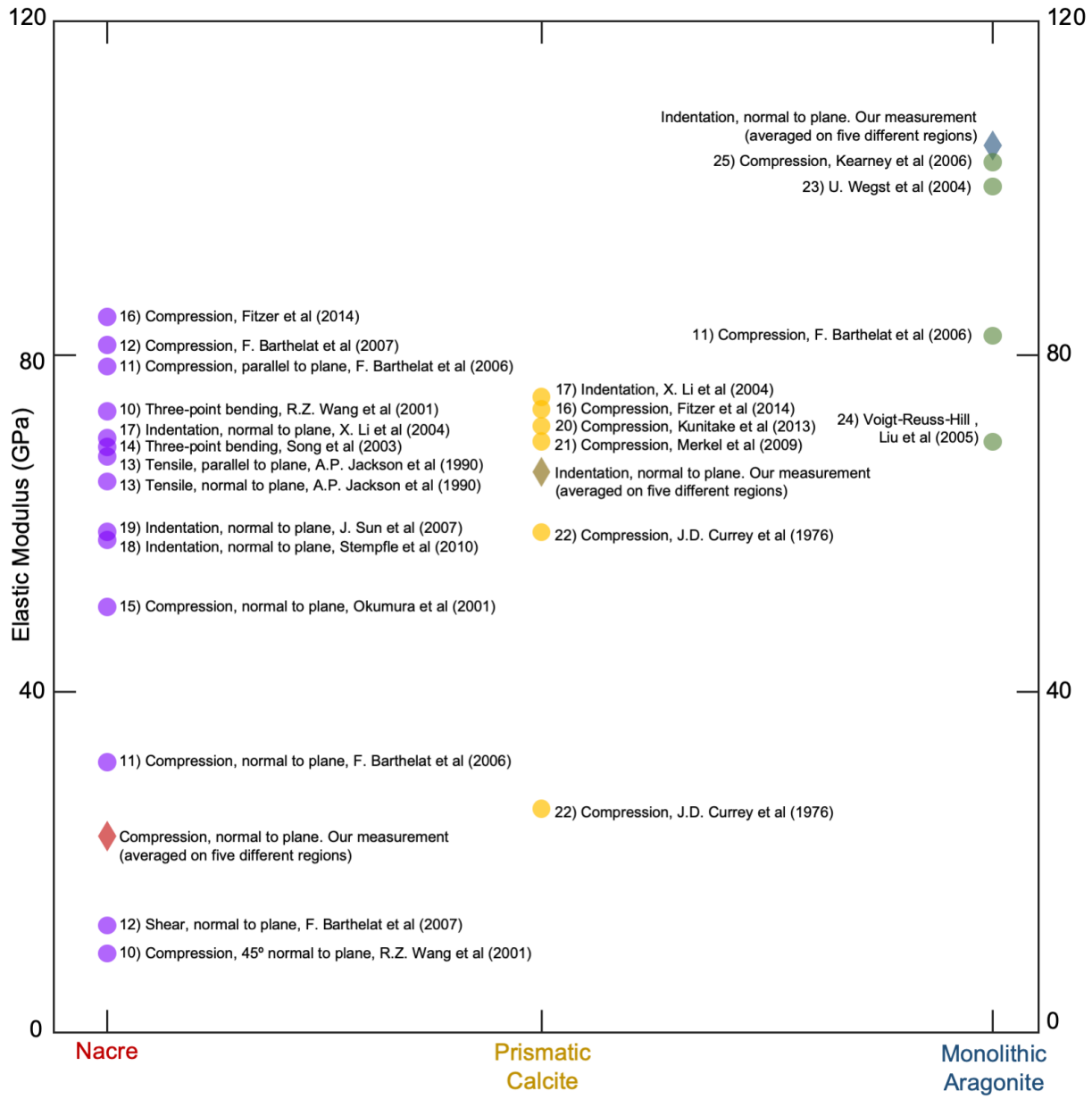

Figure 2.15 Literature survey of elastic modulus of nacre, prismatic calcite, and monolithic aragonite. Both the cross-sectional nanoindentation measurements taken in this study, and previous reports on the bulk properties of the materials are shown[29,35,55-58,68,77,87-92,98,99]. Values from the literature are averages that represent each test type.

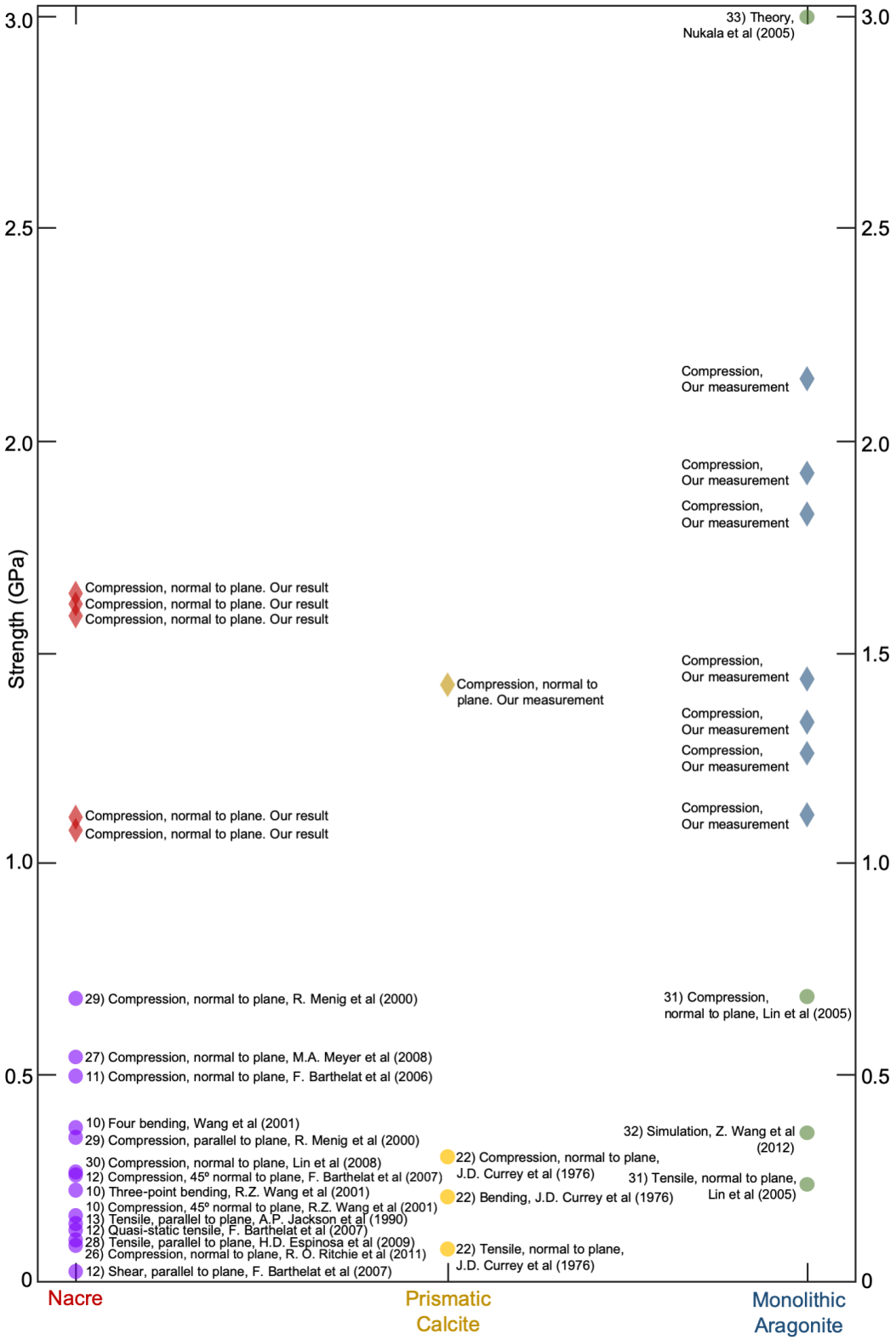

Figure 2.16 Literature survey of strength of nacre, prismatic calcite, and monolithic aragonite. Both the cross-sectional nanoindentation measurements taken in this study, and previous reports on the bulk properties of the materials are shown[17,28,34,35,55,56,68,74,77,78,100-102]. Values from the literature are averages that represent each test type.

2.4. Conclusion

The present in-situ S/TEM nanoindentation study illuminates nacre's distinct non-linear elastic deformation processes that provide high resilience. We see how large forces can drive nacre into locked states that allow the material to distribute strain across tablets and recoverably absorb energy through inorganic and organic compression, nanograin reorientation, and the deformation of organic inclusions. After the load is removed, locked nacre completely recovers both its original morphology and mechanical strength. Even after fracture, failure is mitigated through barriers to crack propagation that preserve the macroscale architecture and allow nacre to retain its mechanical properties and further sustain impact. The material's structure and deformation mechanisms allow it to absorb more mechanical energy than geological monolithic aragonite and biogenic prismatic calcite. Using in-situ S/TEM nanoindentation, the mechanical properties of the material were tested down to the individual tablets where yield ~3 times stronger than bulk measurements were observed.

This approach enables investigation of the wider range of evolutionary optimized biomineral to reveal advantages underlying each's nanomechanical design. The study of deformation and fracture under nanoindentation is a subset of the broader fracture phenomena in nacre and other biological materials which may reveal additional nanomechanical responses to external forces such as tensile strain or shear. The observed mechanisms reported in this work may guide theoretical models of deformation behavior, and the demonstration of *in situ* S/TEM nanoindentation of nacre opens the possibility of other *in situ* S/TEM such as bending, tensile, etc. across a wider range of biological and bio-inspired composites. For nacre under compression, the rich multiscale resilient deformation processes and interlamellar locking inspires new synthetic routes to complex structural materials.

CHAPTER III

The Mesoscale Crystallinity of Nacreous Pearls

A pearl's distinguished beauty and toughness is attributable to the periodic stacking of aragonite tablets known as nacre. Nacre is a naturally occurring mesocrystal that remarkably arises in the absence of translational symmetry. Gleaning the inspiring biomineral design of a pearl requires quantifying its structural coherence and understanding the stochastic processes that govern formation. By characterizing the entire structure of pearls (~3 mm) in cross-section at high resolution, we show nacre is a medium-range mesocrystal formed through nanoparticle assembly processes. Self-correcting growth mechanisms actively remedy disorder and topological defects of the tablets and act as a countervailing force to paracrystallinity (i.e. long-range disorder). Nacre has a correlation length of roughly 16 tablets (~5.5 μm) despite persistent fluctuations and topological defects. For longer distances (> 25 tablets, ~8.5 μm), the frequency spectrum of nacre tablets follows $f^{-1.5}$ behavior suggesting growth is coupled to external stochastic processes—a universality found across disparate natural phenomena which now includes pearls.

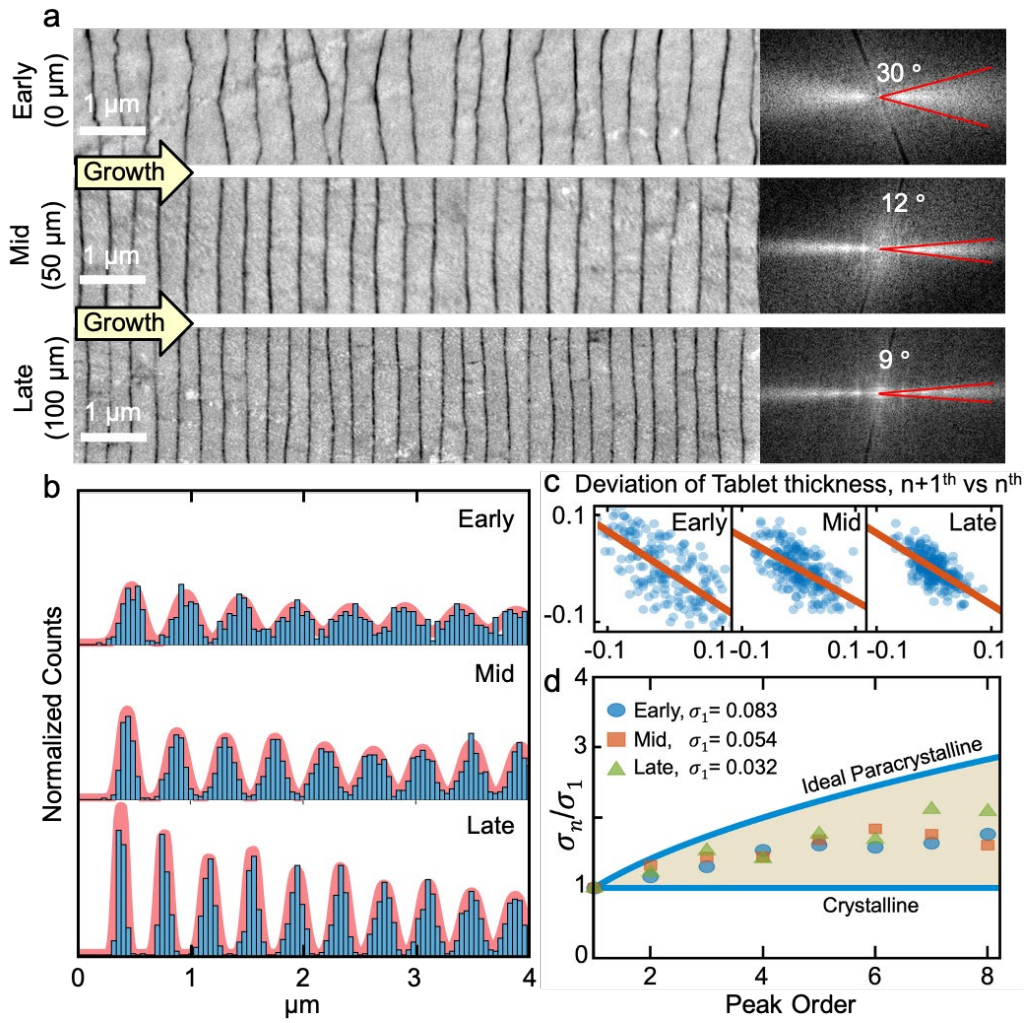

Figure 3.1 Quantification of mesocrystallinity in nacre[2]. **a** Cross-sectional backscatter SEM of the early, middle, and mature stage of nacre growth shows ordering through reduced variation in the interface curvature and tablet thickness. Fourier transforms (right) of nacre (left) imaged by BSE-SEM show that angular broadening decreases from ±15° to ±5°. **b** Pair-correlation functions of nacreous layers represent the probability of finding tablets spaced a given number of unit cells apart. Sharpening of peaks in later nacre indicates increasing long-range order. **c** Correlation of the thickness of tablets with nearest neighbors shows a negative correlation. If one tablet is thick, the next one tends to be thin. **d** Cumulative disorder in nacre described by a real paracrystalline model, demonstrating that the nacre mesocrystal has order between that of a crystal and a paracrystal [J.Gim et al. Ref. 2].

3.1. Introduction

The artist Jorge Méndez Blake illustrated a basic principle of structure in mesocrystals and grown nanocrystalline materials when he placed a single book (i.e. a defect) in a brick wall, displacing every subsequent brick layer[103]. Blake's work demonstrates the principle of paracrystallinity: disorder from any one defective site propagates throughout the layers of the

material[104-106]. In the context of brick-laying, skilled masons overcome this difficulty using external templates to achieve translational order—marked guideposts and lacing cords align layers to prevent disorder from propagating[107,108]. Only with great calculated effort can a ten-story building ensure the same number of aligned brick layers on all sides[109]. Regarding layered growth of nanomaterials, of course, external templates do not exist. Mesocrystallinity—long range translational order of mesoscopic building blocks—is thus improbable due to natural variations in the unit sizes, without the aid of some additional countervailing mechanism. The rare instances where nature assembles mesocrystals therefore merits our attention[110]. Nacre in pearls and mollusk shells are one such example where mesocrystallinity arises in an environment absent of translational symmetry[31,111,112].

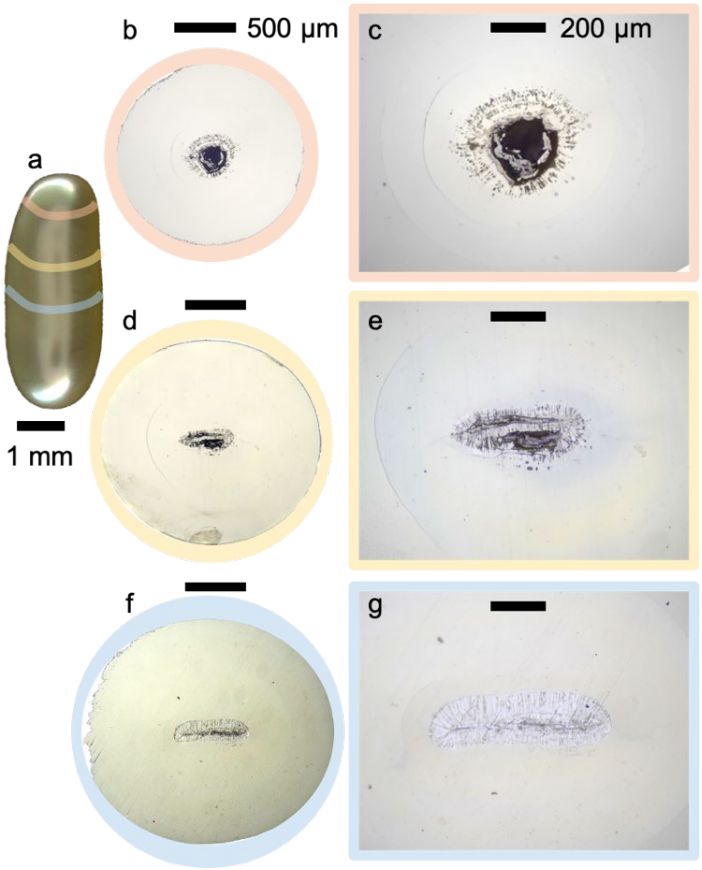

Figure 3.2 Optical overview of a non-beaded cultured Akoya keshi pearl. **a** Photograph of the elongated, baroque-shaped keshi pearl. **b-g** Overview of the cross-sectional pearl along its long axis. Each cross-section shows different sizes and shapes due to the irregularity of the initially formed organic center.

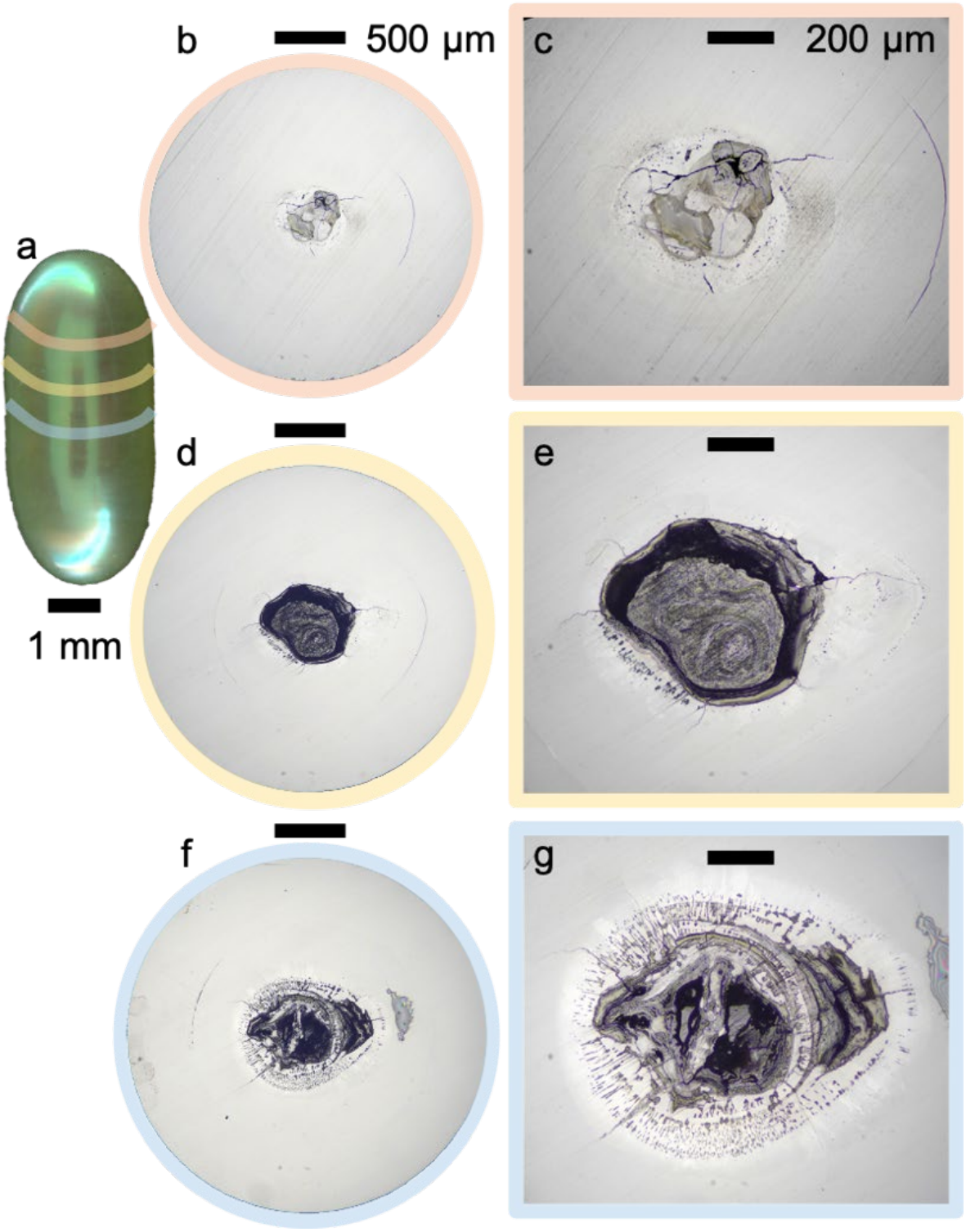

Figure 3.3 Other example of a non-beaded cultured cylindrical keshi pearl. **a** Photograph of the elongated, baroque-shaped keshi pearl. **b-g** Overview of the pearl cross-sectioned several times along its long axis. Each cross-section shows different sizes and shapes due to the irregularity of the initially formed organic center.

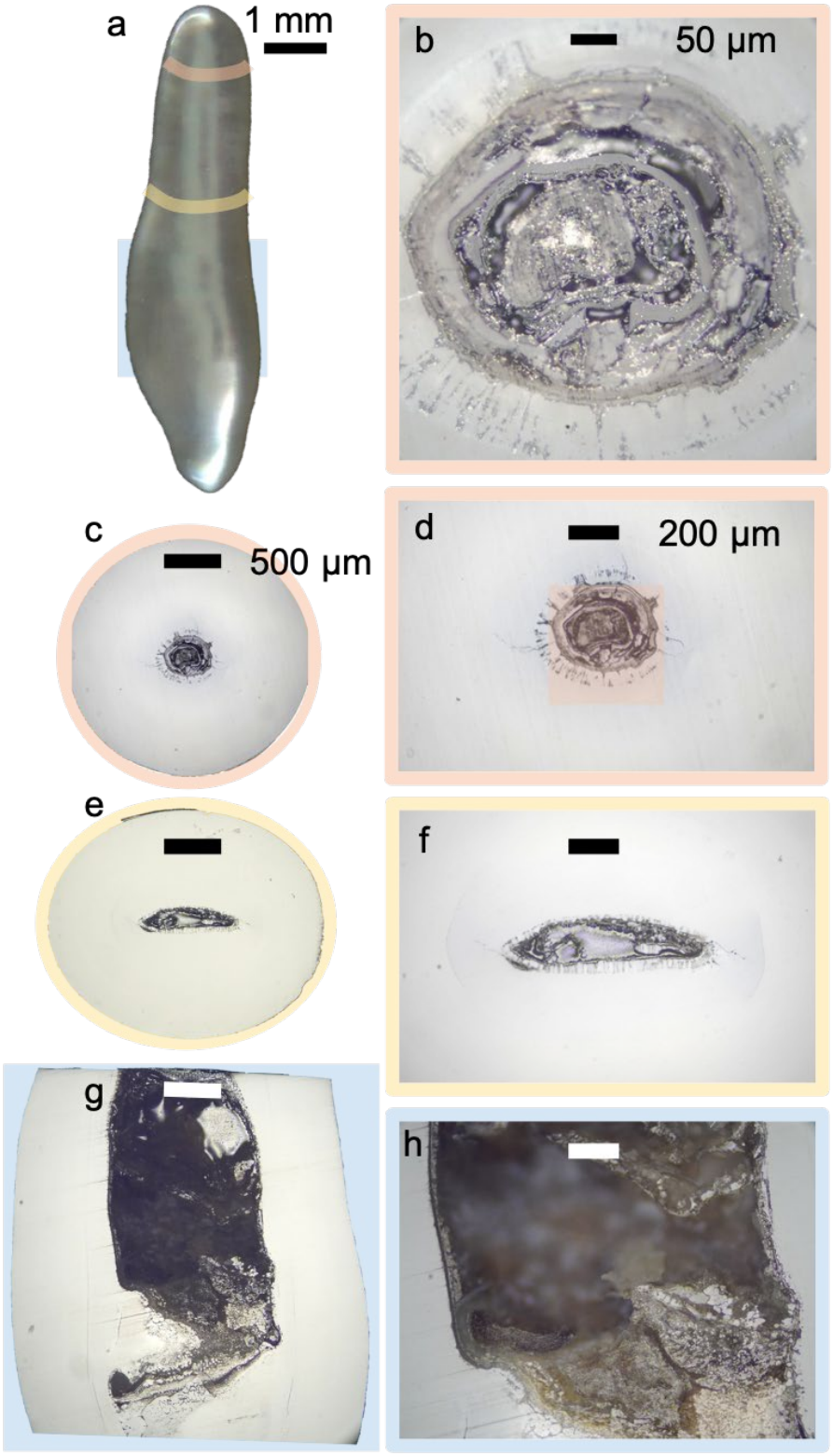

Figure 3.4 A third example of a non-beaded cultured Akoya keshi pearl. **a** Photograph of the elongated, baroque-shaped keshi pearl. **b-g** Overview of the pearl cross-sectioned several times along its long axis. Each cross-section shows different sizes and shapes due to the irregularity of the initially formed organic center.

Pearls are renowned and coveted for their beauty; that beauty results from the diffracting iridescence of periodically stacked tablets (~500 nm thick units) known as nacre[113-116]. Nacre is grown layer-by-layer, with aragonitic tablets bonded by soft interlamellar organic layers (~10-20 nm thickness). These tablets define the unit cell of a mesocrystal. The mesocrystal is a highly ductile structural composite that can withstand mechanical impact and exhibits high resilience on the macro- and nano-scale[1,17,35]. Because of its superior toughness, nacreous shells protect the mollusk's soft body[24,31,117,118], which inspires scientists designing next-generation super-composites[119-121]. Yet, despite a century of scientific fascination with nacre[1,31,111,117,122], its astonishing mesoscale crystallinity has not been quantified, leaving key questions about this material unanswered: does nacre have long-range order? What is the stochastic process that govern its formation?

Here we show nacre is a remarkable medium-range mesocrystal formed through corrective processes that remedy disorder and topological defects. The entire nanostructure of nacreous pearls is characterized in cross-section to reveal complex stochastic processes that govern ordered nacre growth. Beginning atop an initially formed organic center, nanocrystallites self-assemble into bulk aragonite that becomes a substrate to nacre. The initial layers of nacre laid over this substrate are disordered; however, this disorder attenuates within the first 200 layers through self-corrective growth processes that persist throughout the entire pearl. When a tablet is grown too thin, the next tends to be thicker—and vice versa—thus compensating for the initial error. Local irregularities in thickness ($\pm 15°$ variation of interfacial curvature) and topological defects (5.9×10^8 m^{-2} defect density) intermittently appear, yet the pearl maintains order with a correlation length of ~16 tablets (~5.5 μm). However, a pearl is not a perfect mesocrystal and local disorder persists into subsequent layers—a paracrystalline property which

ultimately limits long-range order. For longer length-scales (e.g., > 25 tablets. ~8.5 μm) the aperiodic fluctuation of nacre's tablet thicknesses follow $f^{-1.5}$ noise behavior, which represents external Markov processes with longer memory attributable to cooperative environmental changes such as temperature, pH, food availability, seasonality, and tidal cycles.

3.2. Materials and Methods

3.2.1. Sample Preparation

Specimens of nacreous non-bead cultured Akoya "keshi" pearls produced by the *Pinctada imbricata fucata* pearl-oyster were collected at the Broken Bay Pearl farm (Pearls of Australia Pty Ltd) located on the East coast of Australia. The term keshi pearls is used today to describe beadless pearls that were unintentionally produced as a byproduct of culturing bead-cultured pearls[123]. This farm was chosen as it avoids post-harvest treatments such as bleaching or dying as is otherwise common practice[124] (Otter et al., 2017). Cross-sections were cut from the whole pearls measuring 3-5 mm in diameter using a diamond wire saw. The cross-sections for S/TEM were prepared by mechanical wedge polishing[1,31], which provides large-area, electron-transparent specimens with structural stability.

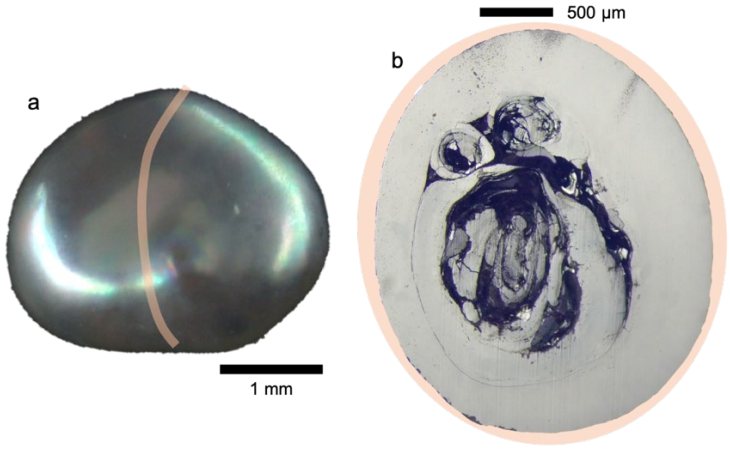

Figure 3.5 Fourth example of a non-bead-cultured Akoya keshi pearl. **a** Photograph of the spherical shaped keshi pearl. **b-g** Overview of the pearl cross-sectioned showing the irregularity of the initially formed center.

3.2.2. Electron Microscopy

SEM images were recorded with a Z-contrast backscattered electron detector of a JEOL IT500 system (10 kV) with an XEDS (X-ray Energy Dispersive Spectroscopy) detector. High angle annular dark-field scanning transmission electron microscopy (ADF-STEM) were performed using a JEOL 3100R05 microscope with Cs aberration corrected STEM (300 keV, 15 mrad) and cold field emission gun. A ADF detector with 120–150 mm camera lengths and a detector angle of 59~74 (inner) – 354~443 mrad (outer) were used to produce Z-contrast images where greyscale intensity is sensitive to the atomic number in the specimen's matrix. Column pressure in the STEM column at the specimen was ~1×10^7 torr.

Low-dose methods, beam shuttering, and examination of regions exposed to the beam were used to separate electron beam irradiation from intrinsic phenomena[1,31]. For STEM measurements, with typical fields of view from ~500 nm to 10 μm the electron dose was typically from ~0.4 to 90 e^{-}·Å^-2 and dose rates ranging from around ~0.1 to 2.7 e^{-}·Å^-2·s^-1. The material was structurally preserved during imaging. However, for the same imaging conditions at higher magnifications (e.g., 20 nm field of view) the radiation dose increases to ~9×10^5 e^{-}·Å^-2 and dose rate to ~3×10^3 e^{-}·Å^-2·s^-1 which causes the material to show electron irradiation damage localized to the small field of view. Thus, larger fields of view are preferred to minimize dose and provide a large area of observation. Atomic resolution STEM requires a small field of view with an on-axis region of interest.

Relative organic concentration in nacre tablets is determined by the area ratio of visible organic phases to mineral. Based on backscattered electron intensity, the area is assigned by thresholding the range of intensities corresponding to the organic phases. The estimated concentration of organic phases in mature nacre is ~5 vol.% which is within a reasonable range

of organic concentrations previously reported[71] (Supplementary Fig.7).

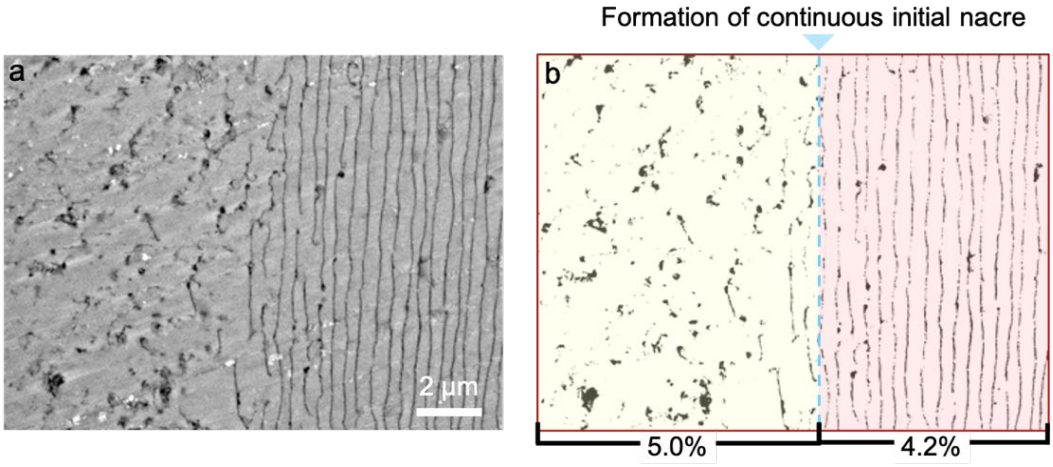

Figure 3.6 Relative organic concentration on a transition zone using the ratio of back-scattered electron intensity. **a** BSE-SEM showing the overview of the transition zone from monolithic aragonite to initial nacre. **b** The area where nacre protein occupies on the transition. In this example, organic materials occupy 5.0 ± 0.6 vol. % on the transition composed of 4.2 ± 0.6 vol. % before the formation of the initial nacre and 5.8 ± 0.6 vol. % after the formation.

Nacre's growth rate is counted backward based on the age of pearl. We assume that only nacre growth takes out most of the Pearl's lifetime because nacre occupies almost 90% of the entire volume compared to the bulk aragonite and the growth rate of nacre along c-axis is slower than that of the aragonite[100,125]. Thus, the growth rate of nacre is the total number of nacre layers (e.g. 2615 layers) divided by the lifetime of pearl (e.g. 18 months ~ 548 days).

3.2.3. Raman Spectroscopy

Confocal Raman spectroscopy was performed on the cross-sections of pearls using a Tescan RISE Microscope equipped with a WITec confocal Raman microscope (Figure 3.7). Raman spectra in the spectral range (100-3700 cm^{-1}) were recorded with a CCD camera using a solid-state 532 nm laser as the excitation source (spectral grating: 600 g/mm, laser power: 10~15 mW, optical lens: 100x). Each Raman spectrum was acquired typically for 0.5~1 s, and with 30~100 of scans to minimize noise effects. The parameters for excitation power,

acquisitions and accumulations are selected to prevent the sample from laser burn. Spectral reproducibility was confirmed by taking several spot analyses.

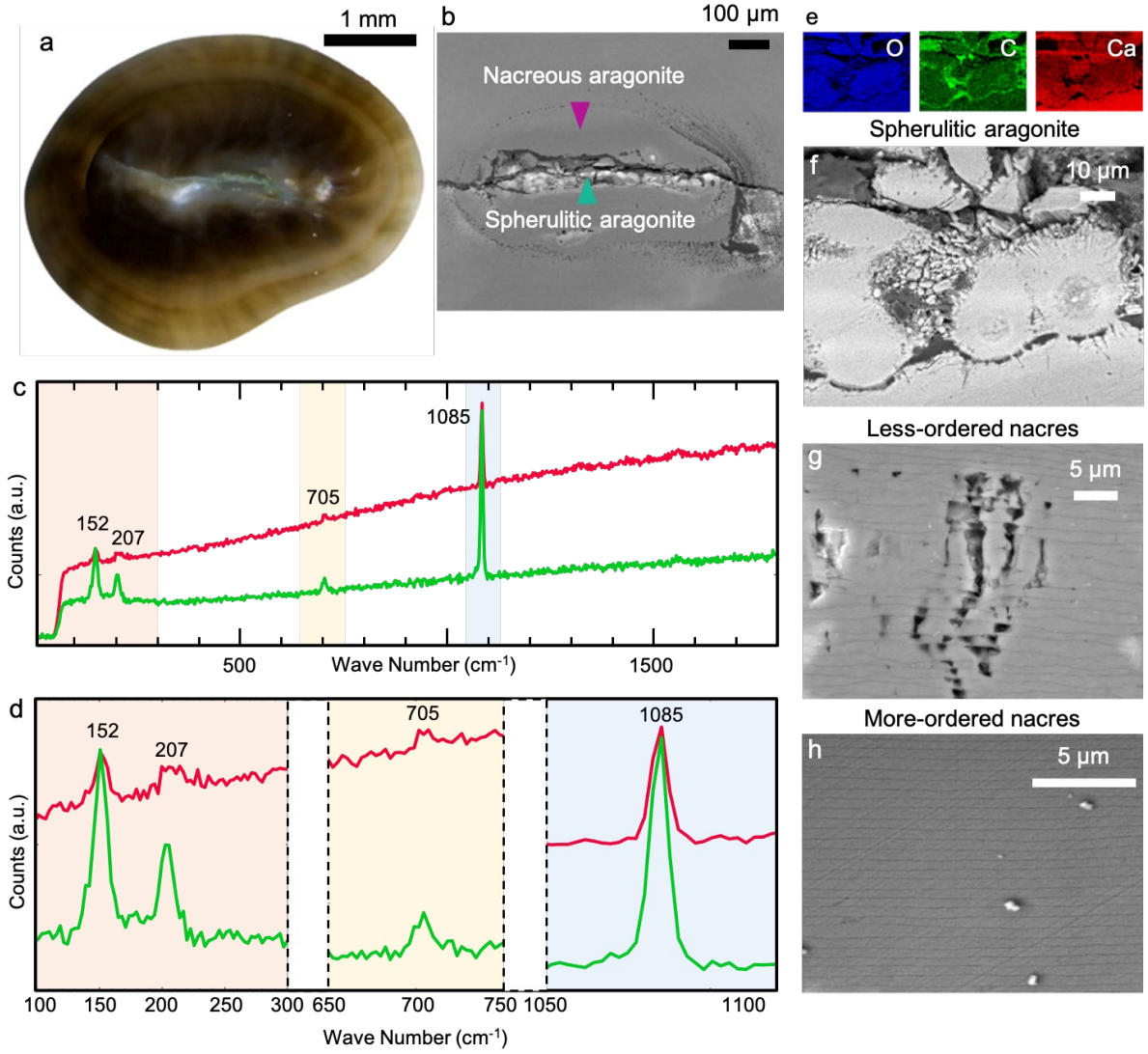

Figure 3.7 Structure of a non-bead-cultured Tahiti keshi pearl. **a** Optical overview of the cross-sectional pearl. **b** Backscattered electron (BSE) SEM the pearl's center. Spherulitic aragonite is initiated on an inner organic center and is followed directly by nacre. **c,d** Raman spectroscopy confirms both nacre and spherulite composed of aragonite. **d-f** Magnified BSE SEM of (b) viewed parallel to the growth direction. Spherulitic aragonite directly transitions to the initial form of nacre (disordered state) and becomes mature nacre (ordered state). Inset in d shows SEM-EDS confirming spherulites and nacreous region covered by organic matrix.

3.2.4. Data Analysis

The pair correlation function describes the probability distributions of nearest-neighbor

(NN) tablets in space about a known tablet position[126]. The one-dimensional pair correlation function is extracted from raw back-scattered electron (BSE) SEM images with high resolution (~3 nm). Mechanical scratches are removed using the image filtering[127]. Interlamellar membranes are identified by finding local minima in BSE intensity line profiles taken perpendicular to the nacre layers. The resulting interfacial positions are then used to calculate the thickness of nacre layers by measuring the distance between positions. The N^{th} tablet thickness is calculated as the difference between the N^{th} and $(N+1)^{th}$ interface positions. A 1D histogram of tablet thickness was then calculated and normalized by a factor of $\frac{1}{k*bw}$ to obtain a discretization of the pair correlation function, where k is the number of samples and bw is the histogram bin width. A sum of normalized gaussians is fit to the histogram peaks and the standard deviations are plotted vs peak order.

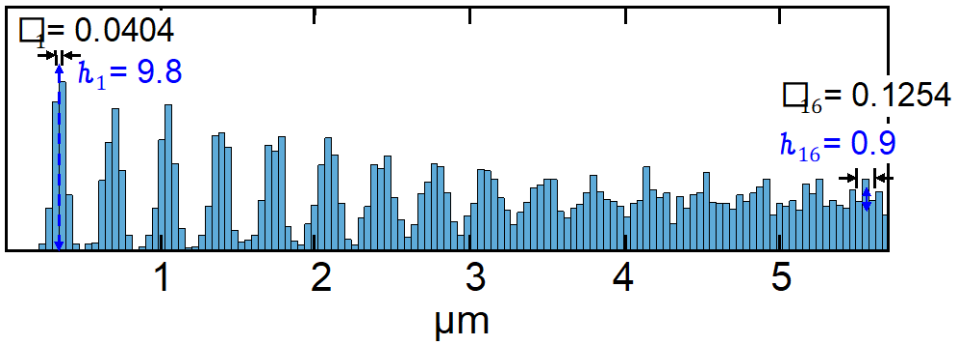

Figure 3.8 Correlation length of mature nacre. Correlation become negligible when the magnitude of the following peak is below 10% of the first peak (i.e., $\frac{h_x}{h_1} < 0.1$). Transitional symmetry lost by 16 layers (i.e. 5.5 μm).

Correlation between the widths of adjacent tablets is calculated by measuring the deviation in tablet width from the local mean tablet width. The local mean is calculated from the list of all sampled tablet widths using a rolling average with a width of three tablets. Thus, the deviation in thickness of the nth tablet is given as $width_N - \left(width_{(N-1)} + width_N + width_{(N+1)}\right) / 3$. Deviations in thickness of pairs of adjacent tablets are plotted against each

other and the correlation coefficient is estimated by linear least squares fitting. Correlation length is defined as the length where the pair-correlation envelope disappears (Figure 3.8). It becomes negligible when the magnitude of the following peak is below 10% of the first peak (i.e., $\frac{h_x}{h_1} < 0.1$). Transitional symmetry is lost by 16 layers (i.e., 5.5 μm).

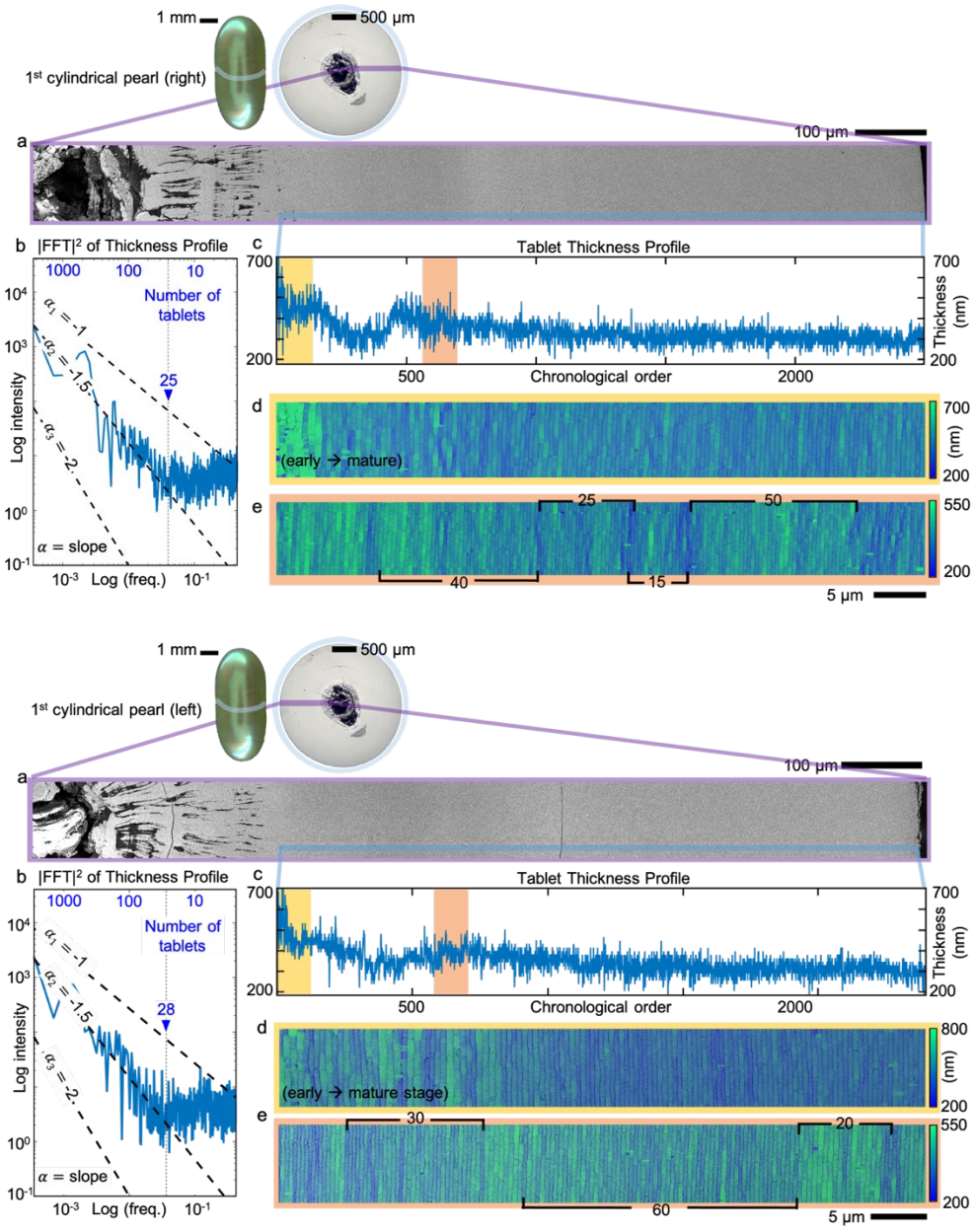

Figure 3.9 Quantification of spectral density of stochastic nacre growth. **(Top)** Nacre on the right side of the pearl. **(Bottom)** Nacre on the left side of the pearl. Both region reveals Markov process in low frequency that is (f < 0.04) for length scales >~25 tablets (or time-scale >~6 days) and a flattening of the 1/f noise due to Nacre's corrective growth at higher frequencies (< ~25 tablets).

Autocorrelation of tablet's stochastic process can be interpreted by power spectral density (PSD), that is generated in the frequency domain by squaring a fast Fourier Transform of thickness profile (Figure 3.9). The tablet thickness is measured from BSE SEM images using the peak detection algorithm described above and is plotted in chronological order where the values are evenly spaced. Since the Fourier transform is not a consistent estimator (the variance is not reduced when the number of data points increases), the PSD is averaged over the profiles from ten neighboring regions and is linearized in log-log scale to reveal 1/f noise. The logarithmic PSD is fitted by polynomial least squares methods to determine the power-law decay coefficient α of the 1/f noise component (i.e., the slope of 1/f noise) for $0.04 < f < 0.0004$ (25 to 2,500 tablets). For frequencies higher than 0.04, the 1/f noise is flattened and change the slope to be positive.

3.3. Results

3.3.1. The Start of Nacre in Pearls

Pearls form either as a natural response to mantle tissue injury or when mantle tissue is deliberately transplanted from a donor into a host shell for pearl culturing. In both cases, the mantle epithelium develops a closed cyst—the so-called pearl sac—programmed to reproduce the structure of the shell[63]. $CaCO_3$ is then secreted onto a manufactured bead (for bead-cultured pearls) or any available debris enclosed by the developing pearl-sac (for non-beaded pearls) within a limited space[128]. The shape of the manufactured or natural nucleus usually dictates a pearl's macroscopic shape[128,129] (Figure 3.2-3.5). Here we primarily study non-bead-cultured "keshi" pearls, grown for ca. 18 months in *Pinctada imbricata fucata* mollusks on the Eastern shoreline of Australia[124].

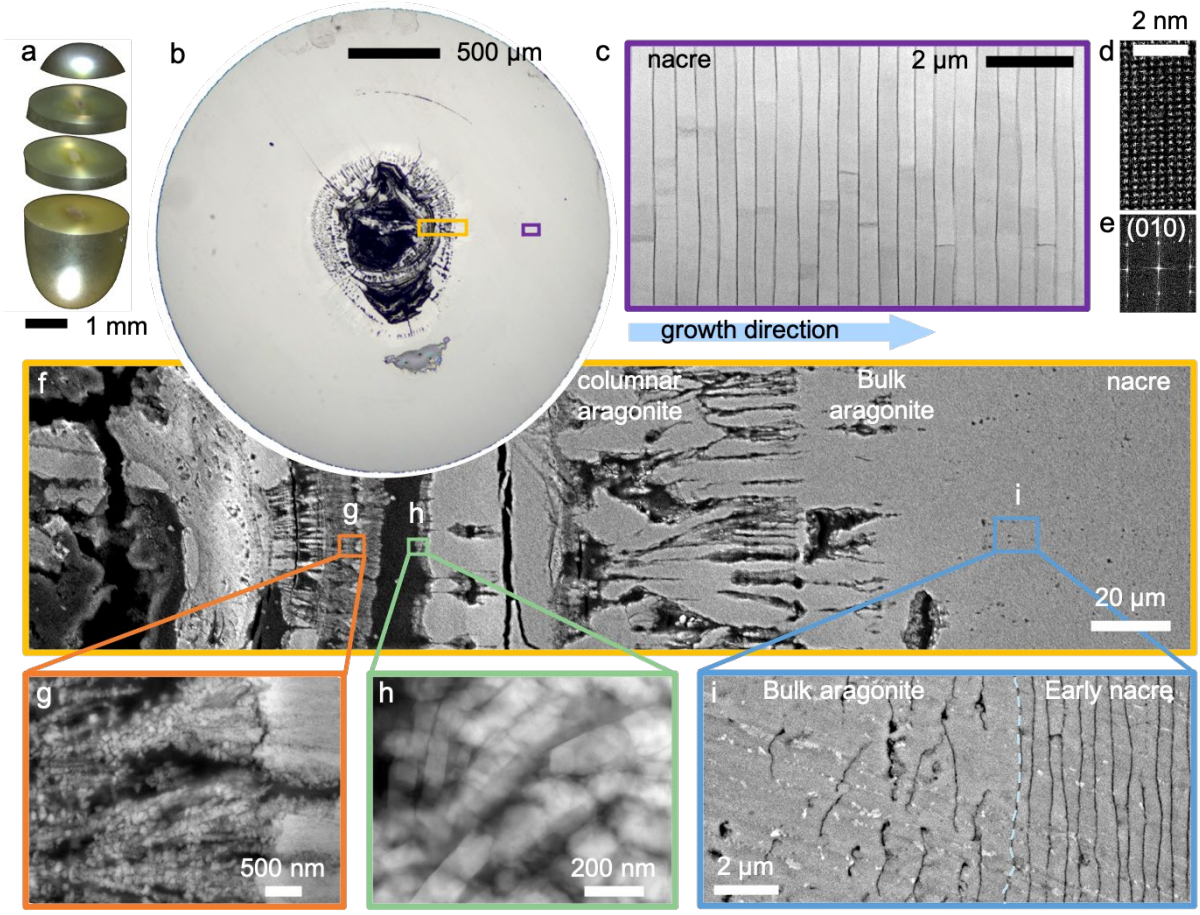

Figure 3.10 Formation of non-bead cultured akoya "keshi" pearls produced in a *Pinctada imbricata fucata* mollusk[2]. **a** Optical overview of a non-beaded keshi cultured pearl showing iridescence due to the interplay of constructive interference at nacre tablet layers with light. **b** Cross-section showing $CaCO_3$ growth begun onto an organic center. **c** Mature nacre (purple box in b) showing ordered state in their thickness and interface curvature. **d,e** Atomic resolution ADF STEM of mature nacre and its corresponding Fast Fourier Transform indicating highly crystalline nacre and a lattice constant that is consistent with aragonite. **f** Cross-sectional backscatter SEM at the center of the pearl (yellow box in b) showing transition from spherulitic aragonite structures to nacre. **g,h** Oriented attachment of nanocrystallites that form massive, structurally indistinct aragonite structure. The growth of acicular $CaCO_3$ is radially distributed and radiates from a series of points, termed the centers of calcification. **i** Formation of nacre beginning directly on massive, structurally indistinct aragonite [J.Gim et al. Ref. 2].

The cross section of a non-bead "keshi" pearl is shown in Figure 3.10b. The mollusk deposits calcium carbonate upon the irregular organic center (~400 µm diameter) and after roughly ~15 µm of bulk aragonite, nacre layers begin to form. Nacre layers are bonded by chitin membranes periodically and synchronously deposited by the epithelium[130,131]. Ordered nacre

makes up 87% of this 2.5 mm pearl (Fig. 3.10b,c). However, the nacre is preceded by more disordered growth stages. Nacre and other biominerals form by non-classical crystallization via metastable transient precursor phases[132,133] and oriented attachment of $CaCO_3$ nanoparticles orchestrated by organic macromolecules (Fig. 3.10g,h, 3.11). The nanoparticles are aragonite crystals in their final form (Fig. 3.12) and their packing intermittently increases until forming columnar aragonite with segregated regions of organic. In Fig. 3.10b this occurs over roughly 200 µm of growth. Throughout this process, the pearl's volume becomes larger and rounder, before penultimately forming a bulk aragonite (Fig. 3.10c). In most observations, we observe bulk aragonite begins after a region reaches positive curvature[134-136].

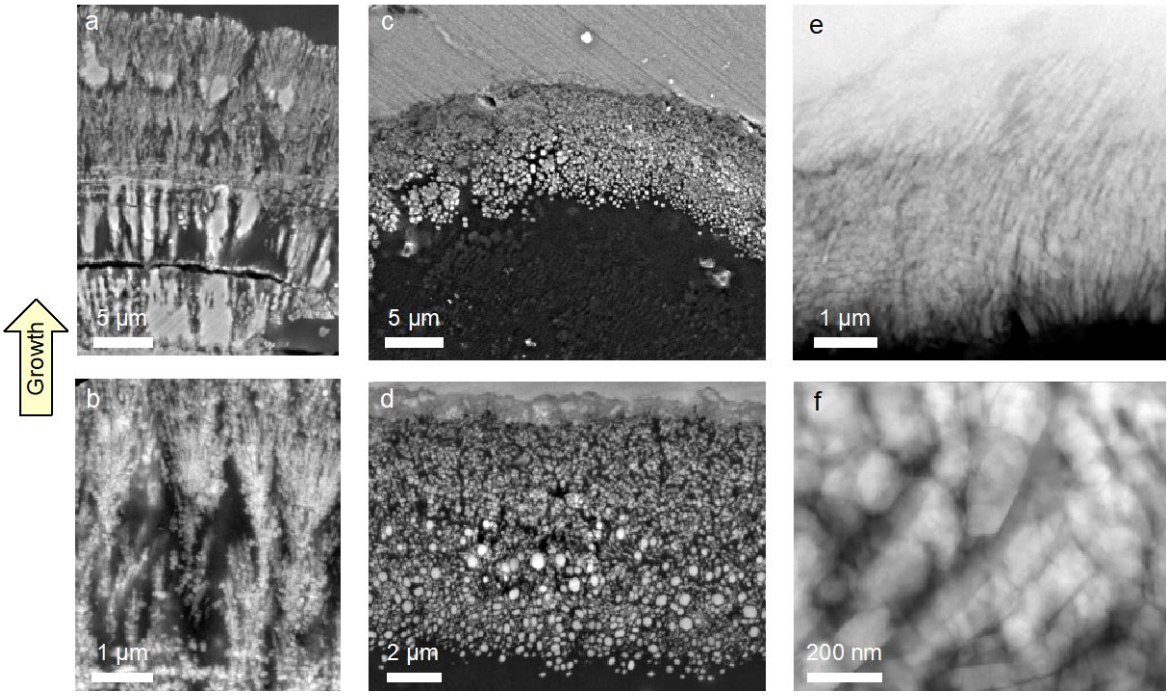

Figure 3.11 Oriented attachment of nanocrystallites that form a monolithic aragonite structure. **a,b** BSE SEM showing non-classical branching to form spherulite $CaCO_3$ in organic nucleated pearl. **c,d** BSE SEM showing non-classical branching to form spherulite $CaCO_3$ in organic nucleated pearl. **e,f** High-angle annular dark field (HAADF) STEM shows linearly oriented attachments of nanocrystallites to form monolithic aragonite.

In pearls, nacre forms abruptly on bulk aragonite. At the start of nacre, around 440 µm (±12%) from the organic center in Figure 3.10, the bulk aragonite is an approximately flat

substrate (curvature of ~0.002) with locally rough texture (~200 nm variation over 7 µm). About 10-20 µm prior to the first nacre layer, the bulk organic phases show deposits equal to the amount observed for mature nacre suggesting the genetic processes directing the system towards nacre deposition start earlier than the structure itself (Fig. 3.6). The same transition was found in non-bead cultured Tahitian "keshi" pearls produced by the *Pinctada margaritifera* mollusk (Fig. 3.7). This direct nacre growth onto bulk aragonite in pearls is distinct from nacre formation reported in mollusk shells (e.g. *Pinna nobilis*) where the assembly process is driven by aggregation of nanoparticles within a several-micron-thick organic matrix[64].

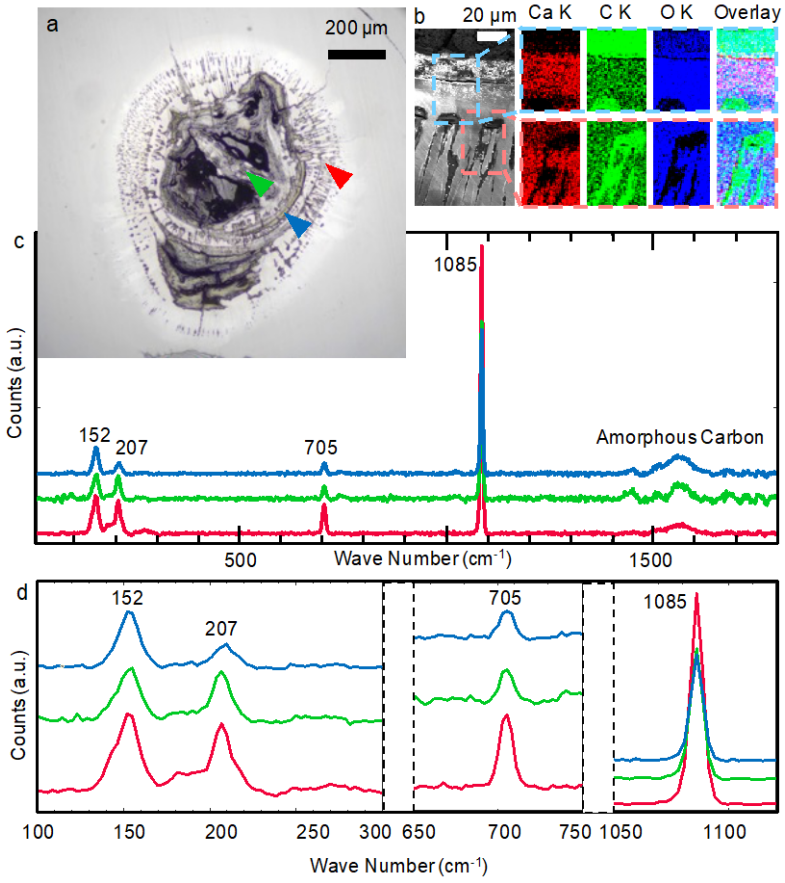

Figure 3.12 Cross-sectional overview of the non-beaded cultured Akoya keshi pearl. **a** Optical overview of pearl in cross-section showing that nacre growth begun with spherulitic aragonite on organic material that is later followed by nacre. **b** Backscattered electron (BSE) SEM the pearl's center showing spherulitic aragonite initiated on an inner organic center and followed directly by nacre. SEM EDS maps show the spherulitic aragonite firmly grown onto the remnant organic material at the center of the pearl. **c, d** Confocal micro-Raman spectroscopy performed on the pearl identifies both the spherulitic and the nacreous region as aragonite.

3.3.2. Mesocrystallinity of Nacre

The first nacre tablets are non-uniform with substantial thickness variation due to the rough aragonitic substrate on which it forms. The Fourier transform of early nacre layers imaged by annular dark-field scanning transmission electron microscopy (ADF-STEM) reveals $\pm 15°$ angular variation in their interface curvature (Inset of Fig. 3.13a). This angular broadening decreases quickly to $\pm 6°$ after 100 layers and further down to $\pm 5°$ after 200 layers (mature nacre). This smoothing of tablet interfaces is clearly visible (Fig. 3.13a, 3.1). At the same time, tablet thickness decreases by 30%, reducing from 500 ± 300 nm for early-nacre to 340 ± 120 nm (a ~40% reduction of variance) for mature nacre. In mature nacre (Fig. 3.13a) peaks visible in the Fourier transform provide the signature presence of mesocrystallinity. However, these peaks in Fourier space do not quantify the long-range order nor describe the stochastic processes that create the mesocrystal.

Pair-correlation functions quantify the mesocrystallinity of nacre in pearls along the growth direction (Fig. 3.13b) by measuring the probability of tablet spacings (see Methods). Subsequent peaks indicate the distance to the 1st nearest neighbor (NN), 2nd NN, 3rd NN, and etc. These plots were calculated based on all pairs of tablets in each stage of nacre (Fig. 3.13a). The first peak represents the average distance between adjacent tablets and subsequent peaks describe longer-range order in the crystal. For ideal crystals, every peak will appear equally sharp. However, in nacre, peaks in the pair-correlation function increasingly broaden—indicating propagation of disorder, as described by the paracrystal model[106,126,137].

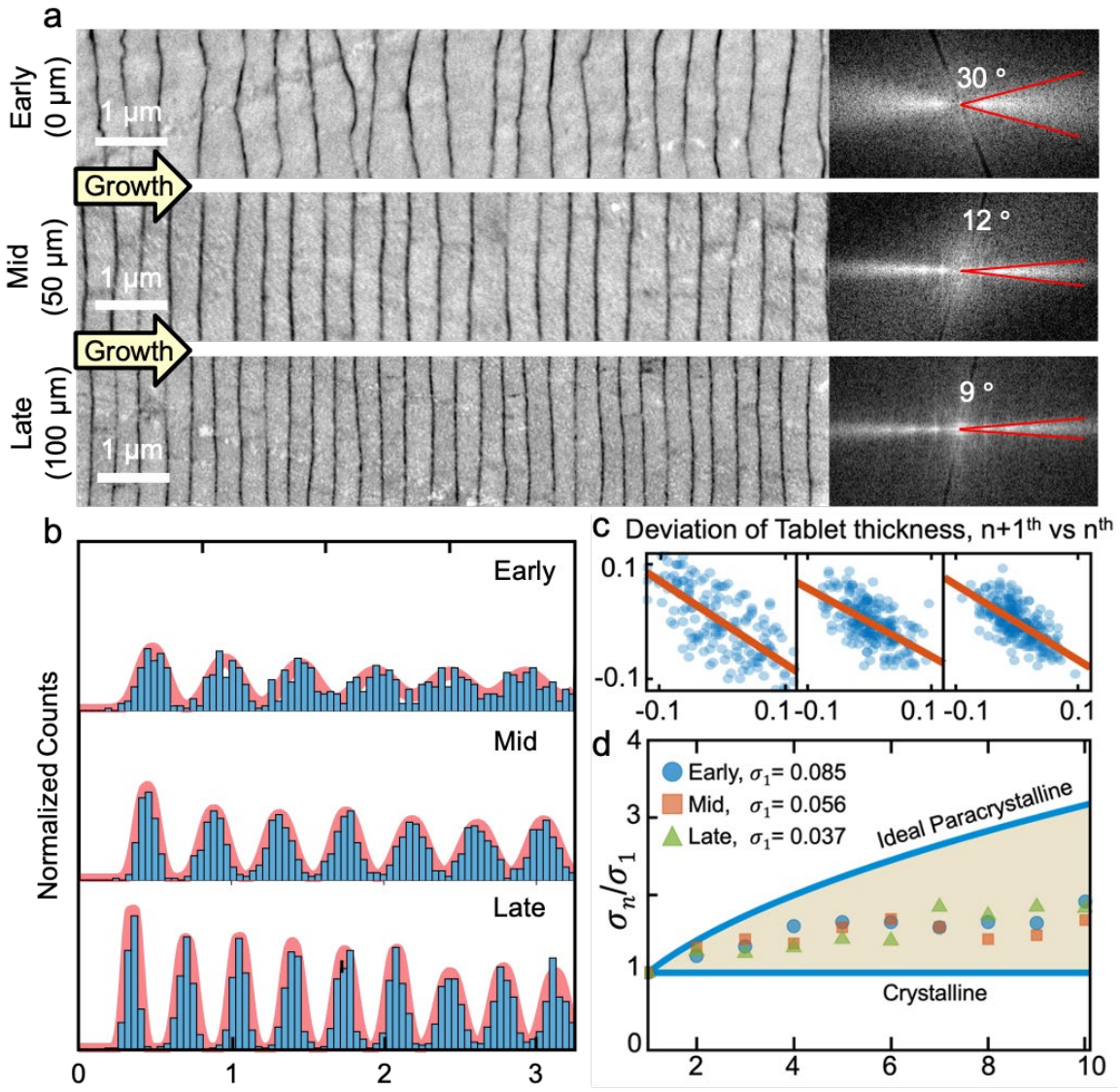

Figure 3.13 Structural variation of nacre growth. **a** Cross-sectional backscatter SEM of the early, middle, and late stage of nacre growth. Fourier transforms of nacre imaged by ADF-STEM showing angular broadening decreased from ±15° to ±4°. **b** Pair-correlation functions of nacreous layers. The progressive sharpening of peaks indicates the system evolved to produce long-range order. **c** Correlation of the thickness of tablets with next nearest neighbors shows a negative correlation. If one tablet is thick, the next one tends to be thin. **d** Cumulative disorder in nacre described by a real paracrystalline model demonstrating that the nacre mesocrystal is neither a perfect crystal nor an ideal paracrystal.

Nacre is well described as an ordered paracrystal or medium-ranged mesocrystal. We report mature nacre has a correlation length of 5.5 µm and translational order is lost by 16 layers. Correlation length is defined as the length where the pair-correlation envelope disappears. (See Methods and Fig. 3.8). Thus, although nacre maintains extraordinary translational symmetry

across a dozen or so layers, it lacks the long-range order of a true mesocrystal. In paracrystals, a deviation in layer thickness displaces subsequent layers and thus disorder propagates. Defects and tablet variation degrade translational symmetry with distance. The progressive broadening of each peak in the pair-correlation functions quantifies the long-range order and paracrystallinity (Fig. 3.13d). In a perfect paracrystal, the standard deviation of peaks broadens by the square root of its peak number ($\sigma_n = \sigma_1\sqrt{n}$)[106,138].

Nacre shares crystalline and paracrystalline structure. As shown in Figure 3.13d, nacre falls below the paracrystal curve (more ordered) and above the flat crystalline curve. The paracrystallinity, or broadening of peaks, is approximately equivalent in early, mid, and mature-stage nacre suggesting the growth mechanisms may be equivalent. However, the sharper first order peaks in mature nacre reflect improved initial conditions (i.e., early nacre begins on a rough substrate).

Nacre maintains crystallinity through self-correcting growth processes. Each nacre layer attenuates the bumps and valleys of the previous nacre layer. If one tablet is thicker than average, the next tends to be thinner. This negative correlation of thickness between adjacent nacre layers is quantified in the early, mid, and mature nacre in Figure 3.13c. The negative correlation is strong and follows an autoregressive model that allows ordered mesocrystalline growth to reach steady state in ~200 layers, which demarcates maturity. In uncorrelated growth, thickness variation of each nacre tablet would devastate the long-range order of the mesocrystal—much like Jorge Méndez Blake's brick wall[103]. However, nacre self-corrects for fluctuations in tablet thicknesses and occasional screw dislocations (Fig. 3.14a,b, 3.15, and 3.16).

3.3.3. Topological Defects in Nacre

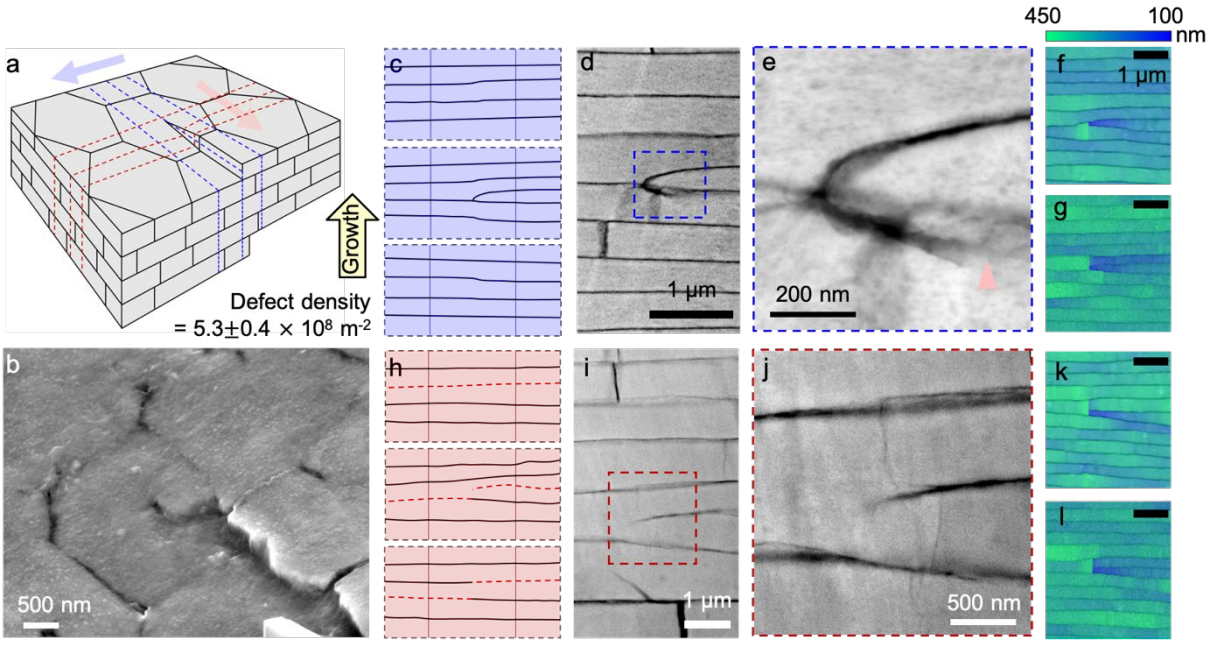

Figure 3.14 Topological defects in nacre. **a** Schematic of topological defects in nacre[2]. **b** 45° tilted backscatter electron microscopy showing a topological defect in nacre. **c** Cross-section of the schematic perpendicular to the slip plane (along the direction of blue arrow in a). **d, e** ADF STEM showing the extra tablet generated due to the defect and the mineral bridge connected to the adjacent layer. **f, g** Thickness map of the extra tablet showing abrupt change of thickness at the point of defect. **h** Cross-section of the schematic along the slip plane (along the direction of red arrow in a). **i, j** HAADF STEM showing the extra organic interface split by the defect. **k, l** Thickness map of the extra organic interface showing abrupt change of thickness at the point of defect [J.Gim et al. Ref. 2].

Local disorder in pearls encompasses topological defects (i.e., screw dislocations) of the tablets and organic interfaces. SEM images at the pearl surface and a corresponding schematic illustrates how screw dislocations originate in nacre (Fig. 3.14a,b, 3.15, and 3.16). High-resolution ADF-STEM images show the dislocation in cross-section along perpendicular axis (Fig. 3.14c-l and 3.16). When viewed parallel to the slip plane, a mineral bridge at the dislocation marks the defect origin. Viewed normal to the slip plane the screw dislocation appears as an additional, partial organic boundary. Screw dislocations in nacre are known[139-141] and recently reported to couple as chiral pairs through a dissipative distortion field that helps accommodate the space filling requirements of nacre[122]. In cross sections, screw dislocations can be easily mis-identified as edge dislocations.

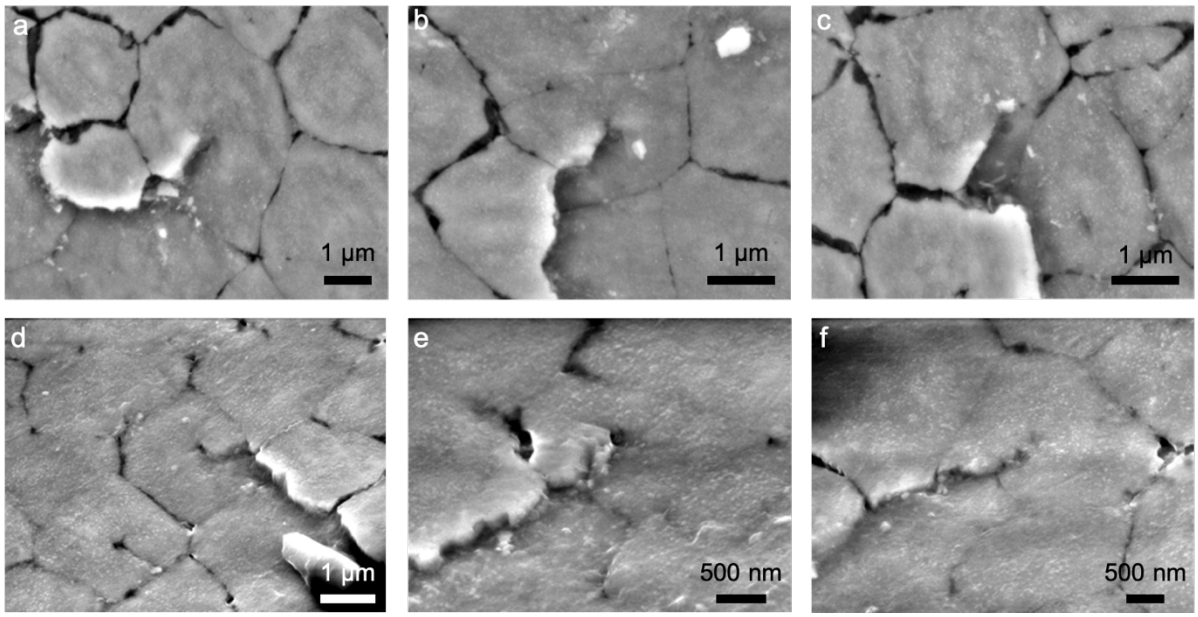

Figure 3.15 Top-viewed topological defect in nacre. **a-c** Top-view BSE SEM on the topological defects. **d-f** 45-degree tilted BSE SEM on the topological defects.

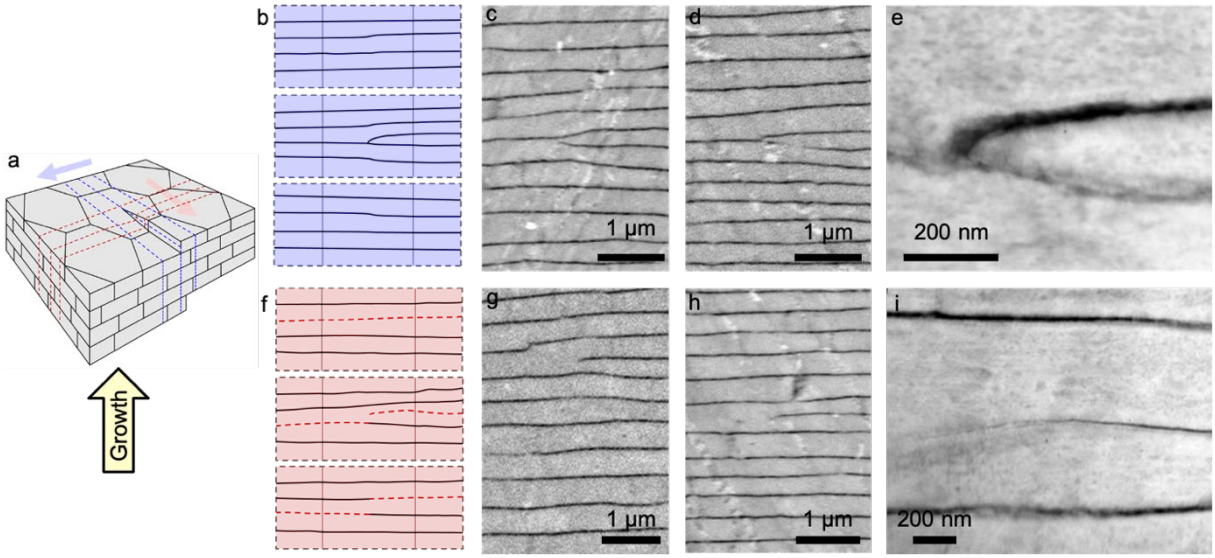

Figure 3.16 Cross-sectional topological defect in nacre. **a** Schematic of topological defects in nacre **b-e** Schematics and BSE images of cross-sectional screw dislocation viewed parallel to the slip plane, showing extra tablet split by the topological defect. **f-h** Schematics and BSE images of cross-sectional screw dislocation viewed normal to the slip plane showing extra organic interfaces split by the topological defect.

The defect density of nacreous pearls herein is $5.3 \pm 0.4 \times 10^8$ m^{-2} in plane-view and $6.5 \pm 0.4 \times 10^8$ m^{-2} in cross-section (Fig. 3.14a and 3.17)—this approximate equivalence suggests a homogeneous screw dislocation distribution in three-dimensions. The dislocation density of

nacre is comparable to typical engineering ceramic materials' defect density of around 10^8~10^{10} m^{-2} [141-143]. Our quantification is measured from top-view and cross-sectional SEM by dividing the total number of defects by the total area (Fig. 3.17).

a	Defect (Top-view)	Defect (Cross-section)
Total number	52	42 *extra tablet :42 *extra interface :42
Total area (μm^2)	98,789	64,721
Defect density (# defects / m^2)	5.3±0.4 × 10^8	6.5±0.5 × 10^8

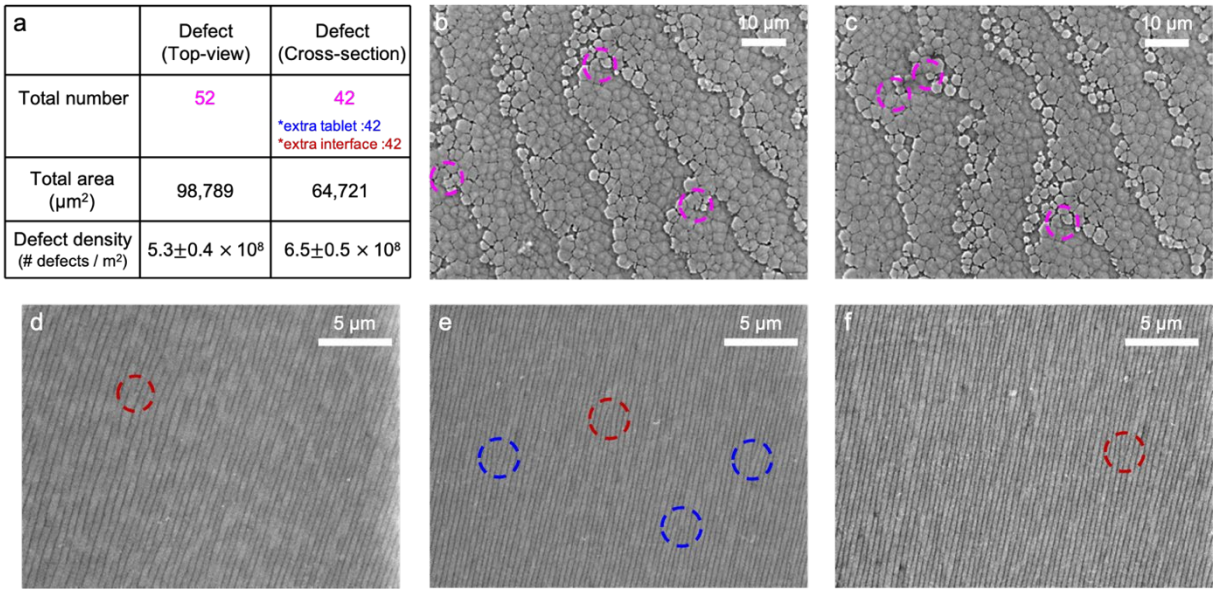

Figure 3.17 Quantification of topological defects. **a** Quantification of topological defects in Top-view and Cross-sectional view. **b,c** Top-viewed BSE SEM images showing topological defects (magenta circle) on the surface of pearl. **d-f** Cross-sectional BSE images of topological defects sectioned in a direction to normal to a-axis (blue circle) and in a direction to parallel to b-axis (red circle)

Despite the prevalence of screw dislocations, nacre's self-correcting growth processes preserve mesocrystallinity via substantial thickness changes (~28%) at the topological singularity. Figure 3.14f,g,k,l shows tablet thicknesses at and around screw dislocations viewed in cross section parallel or perpendicular to the slip plane. The singularity causes tablets to become thinner to accommodate an additional layer without disrupting the long-range order of the mesocrystal. Within just a couple layers, above or below the dislocation, nacre visually returns to uniform, periodic growth.

3.3.4. Stochastic Nacre Growth Follows 1/f Behavior

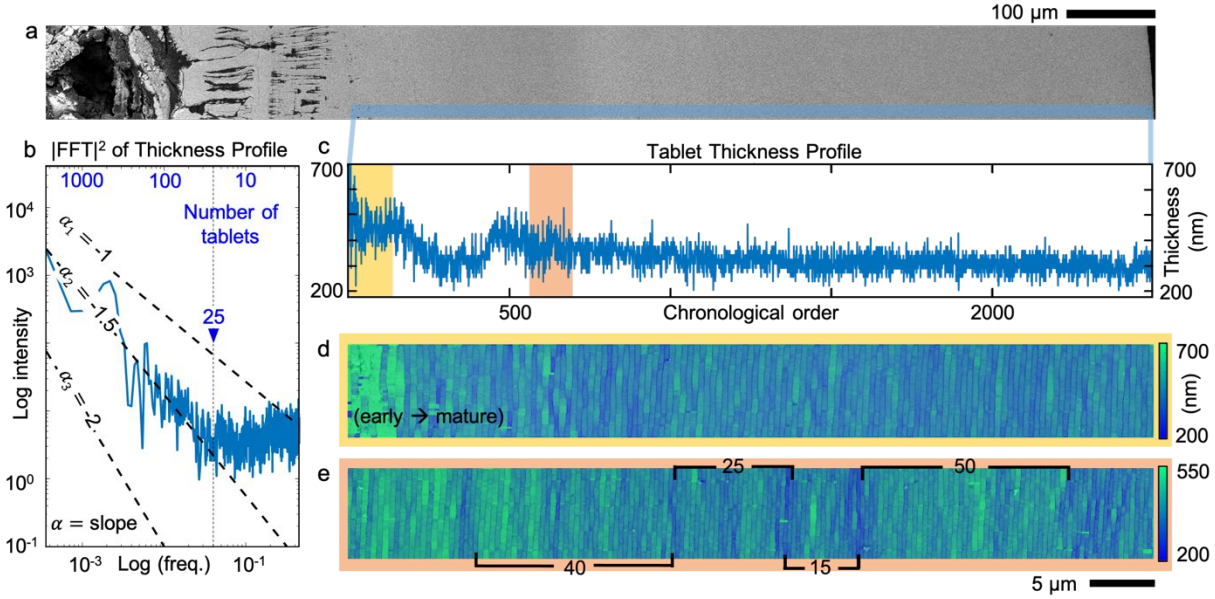

Figure 3.18 Growth dynamic of nacre throughout the entire cross-section of the pearl[2]. **a** Overview of the pearl cross-section spanning from center to edge. **b** Log-log plot of the spectral density of the tablet thickness profile showing nacre thickness variation described by Markov process. **c** Thickness profile across the entire pearl cross-section showing a large fluctuation in the thickness of early nacre which is quickly flattened out with still local variation in late nacre. **d** Thickness map from early to late stage of nacre corresponding to the orange square in the profile. It shows an abrupt attenuation of disorder in thickness and interface curvature. **e** Thickness map of the mature nacre showing the stacks of tablets with a different range of thickness [J.Gim et al. Ref. 2].

To understand the stochastic growth processes over longer lengths and time, nacre tablet thicknesses are analyzed across the entire pearl (2.5 mm diameter) at high-resolution (~3 nm) (Fig. 3.18a). This pearl contained 2615 tablet layers deposited over 548 days giving a mean growth rate of 4 to 5 tablets (1.4 -1.7 µm) per day—in this regard distances may also be considered in terms of time (see Methods). Every tablet of nacre is measured from a mosaic of back-scattered SEM images and a profile of their thicknesses is plotted in chronological order in Figure 3.18c. Initial thicknesses fluctuate substantially but reduce quickly within ~10 layers (Fig. 3.18c, yellow box), as shown in the thickness map (Fig. 3.18d). Notably, sawtooth-shaped bursts in systematic thickness variation are visible (Fig. 3.18c, red box) and repeat aperiodically throughout the entire growth (Fig. 3.18e). The stochastic processes of nacre growth are revealed

in a power spectral density (i.e., squared magnitude of the Fourier transform) of the thickness profile (Figure 3.18b). The spectral density shows two distinct regimes: power law decay across a low to mid frequency regime corresponding to timescales greater than ~5-6 days or distances longer than ~25 tablets and a high frequency regime where the density slightly increases.

The spectral density of a pearl's tablet thicknesses follows power-law decay across low to mid frequencies, colloquially called 1/f noise, suggesting nacre growth has correlations that extend over a wide range of timescales with cooperative effects linked to environmental changes. In stochastic Markov processes the distribution of future events are determined by recent past events,[144,145] and even simple Markov processes can exhibit a spectral density following $f^{-\alpha}$ where $1 < \alpha < 2$. This behavior characterizes a wide range of phenomena from fluctuations in river flow to heart-beats or economic markets[146,147]. The spectral density of nacre follows $f^{-1.5}$ across low to mid frequencies (>~25 tablets or >~6 days). In real-space this corresponds to the saw-tooth shaped bursts in the thickness profile of Fig. 4c,e. Such aperiodic fluctuations can be associated with the $f^{-1.5}$ spectral density and the behavior can be explained by the additive effect of one or several Markov processes representing the external effect of environmental and physiological factors. The coefficient α of power-law decay is estimated by truncating the PSD and applying a square fit for log-log coordinates (See Methods).

The observed power law decay, $f^{-1.5}$, suggests that nacre's growth is governed by a set of stochastic processes with different characteristic time scales. This makes sense: we expect growth to depend on many external factors in the surrounding habitat of the mollusk shell[114-116]. Multiple clocks in nature govern these living animals such as the 30-day circalunar cycle[148,149], the day-night circadian cycle[150,151], tidal changes[152], hibernation in the winter[153,154], and aestivation in the summer[155,156]. This fluctuating marine environment and the natural time scales

of the mollusk are interconnected influences of the non-equilibrium thermodynamical conditions[157-159] of nacre growth and likely explains the observed power law behavior.

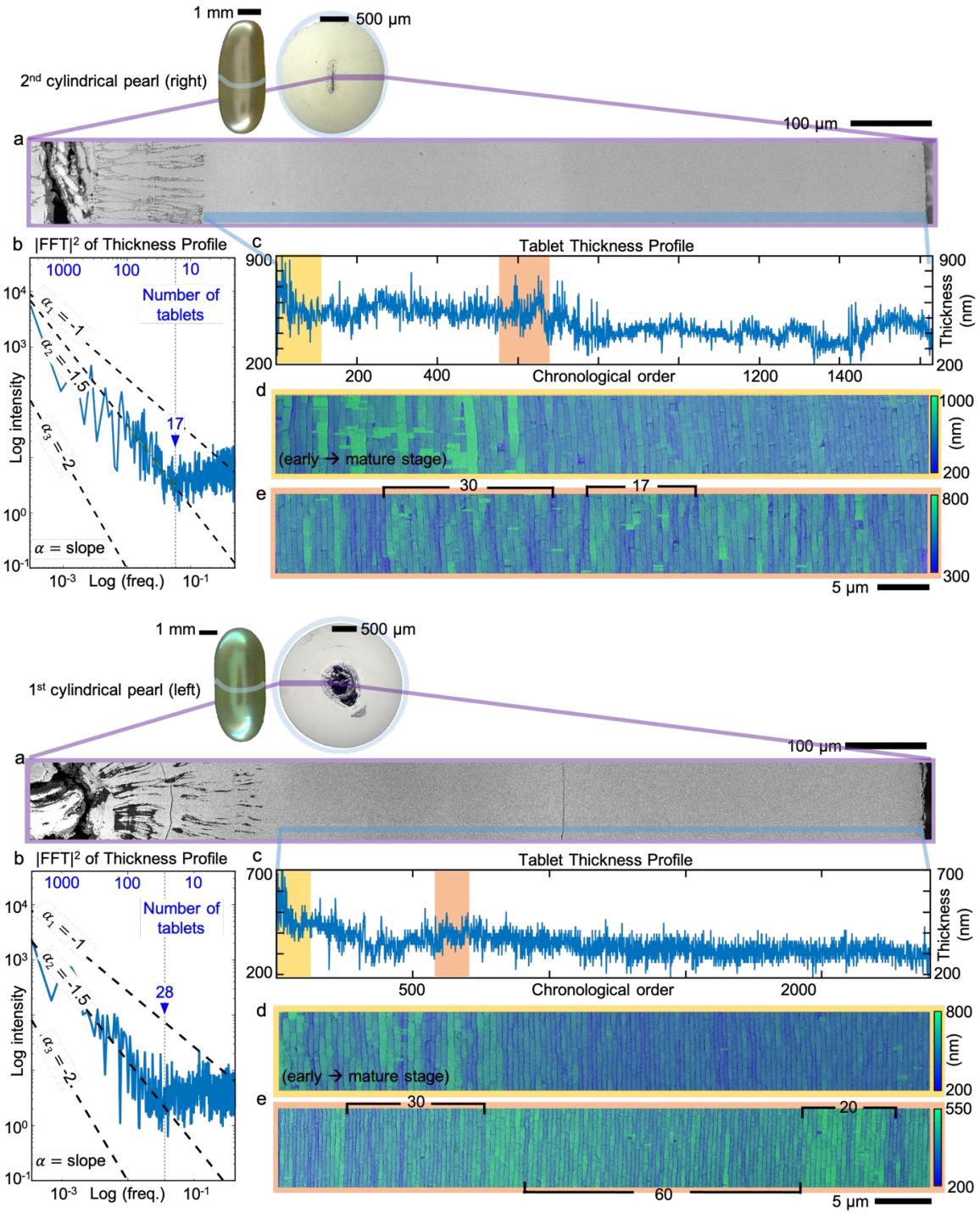

Figure 3.19 Nacre's Growth dynamics from another cylindrical pearl. **(Top)** Nacre on the right side of the pearl. **(Bottom)** Nacre on the left side of the pearl. Both region reveals Markov process in low frequency that is ($f < 0.04$) for length scales >~25 tablets (or time-scale >~6 days) and a flattening of the 1/f noise due to Nacre's corrective growth at higher frequencies (< ~25 tablets).

At high frequencies (< ~25 tablets or ~4-5 days), there is a flattening of the 1/f noise and a slight increase in the power spectrum due to corrective growth processes whereby the thickness of each tablet is anticorrelated with the thickness of the previous layer. The opposing fluctuations in subsequent layers (shown in Fig. 3.1c and 3.13c) amplifies high frequency variations in a manner consistent with a negative autoregressive process[160-162] and causes the slightly increasing profile of the spectral density at high frequencies (Fig. 3.18b). Mechanistically, the source of this correlative correction is not clear—it may be explained by a partial viscosity of the $CaCO_3$ upon deposition under isostatic pressure or possibly by physiological responses. Direct observation on the kinetics of the formation is challenging because existing nanocharacterization methods are highly invasive, are conducted in high-vacuum environments, and require sacrificing the animal. It is a challenge for future researchers to develop specialized in vivo imaging and analysis techniques.

In nacre, we see a fundamental tradeoff between achieving mesocrystallinity and minimizing tablet thickness variation. Corrective growth occurs to counterbalance disorder and the natural tendency towards paracrystallinity thereby enabling surprising and remarkable mesocrystalline ordering. However, this corrective growth process amplifies variation wherein perturbations in one layer causes an opposite perturbation in subsequent layers.

3.4. Conclusion

Pearls are iconic mesoscale crystal grown by mollusks with no external templates along the direction of growth. Nanoparticles assemble within an organic matrix with increasing density until a rough massive, structurally indistinct aragonite forms and later serves as substrate for nacre deposition. Tablets are then grown layer-by-layer with self-correcting mechanisms

that allow the mesocrystal to accommodate tablet variation and topological defects. Mollusks strike balance between preserving translational symmetry and reducing thickness variation by creating a paracrystal with medium-range order (~5.5 μm coherence length). This balance allows pearls to attenuate the initial disorder during early formation and maintain order throughout a changing external environment. Over longer timescales (>~6 days), nacre growth is mediated by external stochastic processes and exhibits a '1/f' behavior that belongs to a universal class of vast and disparate phenomena. Quantifying the mesocrystallinity of nacreous pearls reveals underlying processes of formation and provides new metrics and illuminates new paths toward mimicking nacre's hierarchical design.

CHAPTER IV

Hierarchical InGaN Nanowires for High-Efficiency Solar Water Splitting

4.1. Solar Water Splitting

Solar water splitting has become a promising way to alleviate supply instability of solar energy by directly storing energy in the form of hydrogen fuel (Fig. 4.1). Maximizing efficiency for photoelectrochemical (PEC) water splitting requires (i) a tunable bandgap that captures the solar spectrum, (ii) an energy band edge that spans the water redox potential, and (iii) high quantum efficiency[5,163,164]. Although a variety of materials such as Si, Ta_3N_5, and $BiVO_4$ have been studied as photoelectrodes, most materials have not yet fulfilled these requirements. For instance, the onset potential of Si and Ta_3N_5 is too large so charge carriers cannot be sufficiently generated under sun illumination and $BiVO_4$ has a wide 2.4 eV bandgap that limits the efficient utilization of the solar spectrum[5,163].

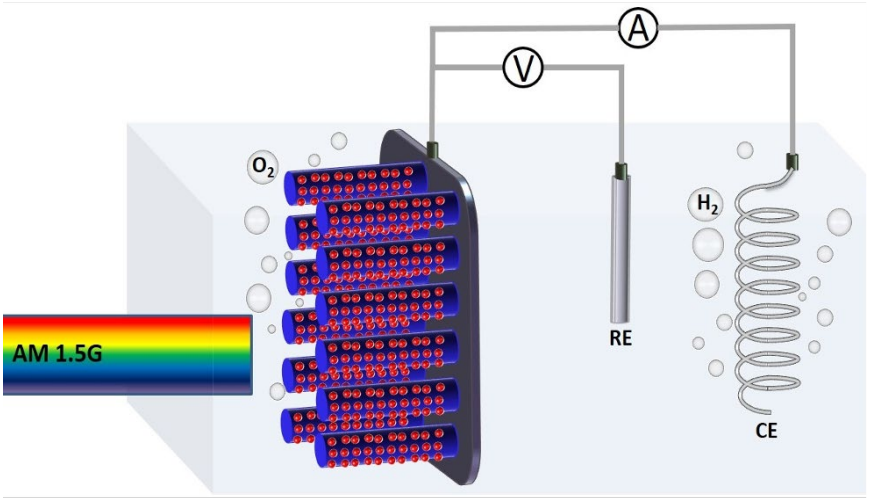

Figure 4.1 InGaN nanowires with IrO_2 nanoparticles provide enhanced water splitting[5] [S. Chu et al. ref. 5].

The InGaN ternary system is an optimal photoelectrode for efficient solar hydrogen production (Fig. 4.2). The bandgap (E_g) of InGaN is direct and tunable from 3.4 (GaN) to 0.65 eV (InN) for indium compositions up to ~50% (Fig. 4.3), allowing optimal use of the entire solar spectrum (Eg ~ 1.7 eV)[5,165]. In addition, it has a high absorption coefficient to increase photo absorption and large charge carrier mobility to enhance charge carrier extraction. These benefits could potentially enable a solar-to-hydrogen efficiency over 25%[5,163,166] (Fig. 4.2). However, creating high-performance InGaN photoelectrodes is difficult as In-rich crystals are highly strained causing phase segregation and subsequent performance degradation.

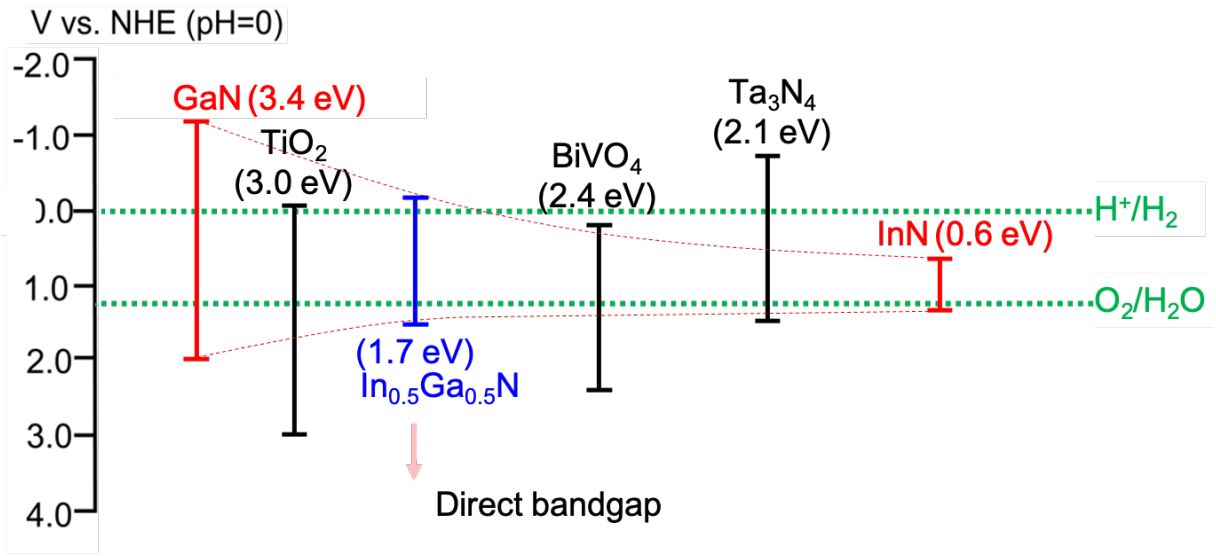

Figure 4.2 The maximum theoretical photocurrent densities of different photoanode materials under AM 1.5G 1-sun illumination[5,164] [reproduced from ref. 5 and 164].

4.2. 1D Nanostructures Grown by Molecular Beam Epitaxy

The growth of highly single crystalline InGaN with high In content is a key to tune the bandgap facilitating the use of entire solar spectrum and large enough overpotentials for PC and PEC activities. However, it is difficult to grow high crystalline InGaN with uniformly homogeneous indium composition. Firstly, the large difference in interatomic spacing between

InN and GaN results in a solid phase miscibility gap. In addition, the relatively high vapor pressure of InN as compared to that of GaN leads to low indium incorporation in the InGaN composite[165]. Consequently, the immiscibility of InN and GaN combined with the difference of the vapor pressures generally causes high density threading dislocations and phase separation with In-rich clusters, leading to the inefficient light absorption to largely limit the performance for water oxidation. Hence, much progress has been made in incorporating indium into GaN crystal by metal-organic chemical vapor deposition (MOCVD), hydride vapor-phase epitaxy, or MBE in a form of thin film, quantum well (QW), or nanowires[3-5,164]. However, QW structure makes it difficult to fabricate practical devices and thin film and nanowires because it shows phase segregations to hinder to achieve a desirable bandgap structure.

Alternatively, using plasma-assisted molecular beam epitaxy (MBE) which is self-catalytic growth, highly crystalline InGaN can be grown with controllable sizes, densities, and surface morphology by optimizing growth parameter such as temperature, time and composition of reactants[5,164]. In particular, the low substrate temperature (~550 °C) and optimal N_2 flow rate (~0.45 - 0.55 sccm) can promote the strain relaxation growth which is the formation of the non-thermodynamically-stable products[5,167]. Moreover, confined structure of heteroepitaxial materials is more effective at relieving mismatch strain coherently compared to planar system such as film[5,168]. Therefore, the optimal growth condition together with the confined geometry allow to reduce phase separation, leading to uniformly homogenous indium concentration in In-rich InGaN growth.

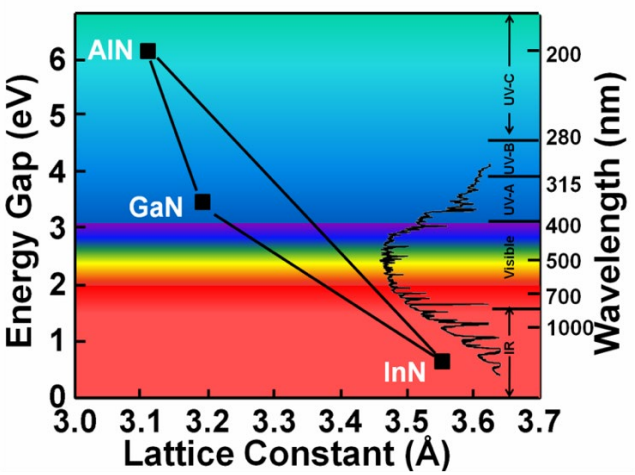

Figure 4.3 Energy bandgap of group III-nitrides verses lattice constant[169] [adapted from ref. 169].

In this chapter, three different type of InGaN photoelectrode system for PC and PEC performance are discussed. The preliminary results demonstrate synthetic hierarchical architectures at each level of structure in InGaN photoelectrode system to enhance PC and PEC activities. In particular, using high resolution electron microscopy combined with analytical spectroscopy using EDX or EELS, the hierarchical structure and their chemistry are investigated at meso-, nano-, and atomic scale to lay the framework for photovoltaic devices harnessing this unique PC and PEC properties. Nanoscale characterization using SEM is implemented to provide morphology and structure of the InGaN open pillars. Cross sectioning techniques developed specifically for nanowire or nanowall geometries are conducted to prepare thin and clean cross-section for high-resolution imaging. The requirements for high-resolution Z-contrast and spectroscopic imaging, a specimen needs to be thin and clean. A specimen become as thin as an electron-transparent thickness that the incident electrons are scattered with matters one time by wedge mechanical polishing. Then, the cross-sectional specimen is precisely milled by Ar ion to get them thinner and clean. Moreover, a wedge-polishing technique provides unprecedented, large-area specimens required to span the entire interface. Lastly, the specialized STEM skills such as putting the specimen on the incident beam axis and confining the electron

beam within sub-angstrom level enable us to identify the structure and chemistry of the nanowall at atomic scale, even on individual atoms followed by data analysis with critical interpretation using STEM with aberration corrected lens.

4.3. Results and Discussion

4.3.1. IrO_2 Coated InGaN/Si Photoanode for Highly Reactive PEC Performance

Here we show low-dimensional nanostructures accommodate crystalline InGaN nanowires capable of enhanced water splitting performance (highest reported value of 10.9 mA/cm^2 at 1.23 V versus reversible hydrogen electrode (RHE)) and photoluminescence (a single emission peak at 720 nm)[5]. Using plasma-assisted molecular beam epitaxy (MBE), highly crystalline InGaN can be grown as one dimensional (1D) nanostructures. This allows high quantum efficiency with a larger surface area for PEC reaction. Cross-sectional electron microscopy of InGaN/Si (Fig. 4.4a-c) reveals that the crystalline InGaN nanowires have an approximate height of ~700 nm tall and diameter of ~200 nm wide which extend atop a polycrystalline growth layer on the Si substrate. The low-dimensional geometry not only allows high In concentrations, but also provides more catalytically active surface area. IrO_2 co-catalysts with a size of 1-2 nm were uniformly loaded on the InGaN surface (Fig. 4.4b) to further enhance performance. The current-potential (J-V) curves of IrO_2 (Fig. 4.4e) show that the photocurrent density of IrO_2/InGaN reaches 10.9 mA/cm^2 at 1.23 V versus RHE due to the lower onset potential of the IrO_2 co-catalyst combined with the sufficient InGaN bandgap of ~1.7 eV. The maximum applied bias photon-to-current efficiency (ABPE) of the IrO_2/InGaN photoanode calculated from the J−V curve is 3.6%, which is the highest among those of previously reported photoelectrodes (Fig. 4.4f).

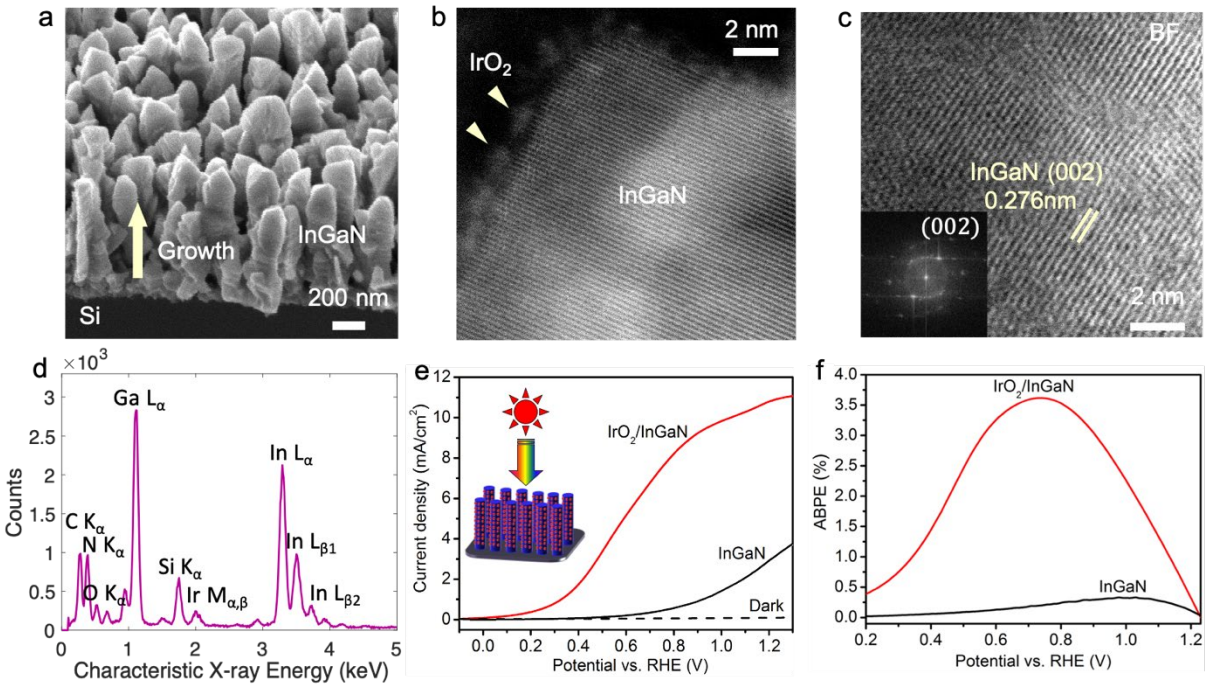

Figure 4.4 InGaN nanowires with IrO_2 nanoparticles provide enhanced water splitting[5]. **a** Side-view SEM reveals epitaxial growth of IrO_2-InGaN nanowires across a silicon wafer. **b** A cross-sectional high-angle annular dark field (HAADF) STEM image shows the ~1-2 nm IrO_2 nanoparticles adsorbed to the InGaN surface. **c** Bright-field scanning-TEM (BF-STEM) images of IrO_2/InGaN sample. Lattice spacing of 0.276 nm correspond to the InGaN (002) plane. Insets are corresponding electron-diffraction patterns. **d** Simultaneous STEM EDS spectrum showing the grown InGaN nanopillars primarily comprised of Ga, In, and N and coated by Pt. **e** J-V curves of InGaN and IrO_2/InGaN in 0.5 M H_2SO_4 under AM 1.5G 1-sun illumination. **f** ABPE of the photoanodes derived from the J–V curves [S. Chu et al. ref. 5].

4.3.2. Pt Coated InGaN Photocathode Monolithically Integrated on a Nonplanar Si Wafer

An efficient p-type InGaN nanowire photocathode is monolithically integrated on an n-type nonplanar Si wafer with an open-pillar design to maximize light trapping[3]. Moreover, photogenerated electrons more efficiently extracted through a GaN nanowire tunnel junction (Fig. 4.5a). The nanowire photocathode exhibits a photocurrent density of 12.3 mA cm^{-2} at 0 V vs. RHE and a large onset potential of 0.79 V vs. RHE under AM 1.5G one-sun illumination. The maximum applied bias photon-to-current efficiency reaches 4% at ~0.52 V vs. RHE, which is nearly one order of magnitude higher than the previously reported values for III-nitride photocathodes. Top-view SEM shows the wires well separated (Fig. 4.5d) and SEM EDS maps

out the top plane of InGaN nanowires with the presence of Pt nanoparticles (Fig. 4.5e). The cross-sectional HAADF-STEM image of InGaN nanowires reveals that the crystalline InGaN nanowires (width ~200 ± 40 nm, height ~800 nm, spacing ~800 ± 80 nm) extend atop an early growth of GaN nanowires (Fig. 4.5b).

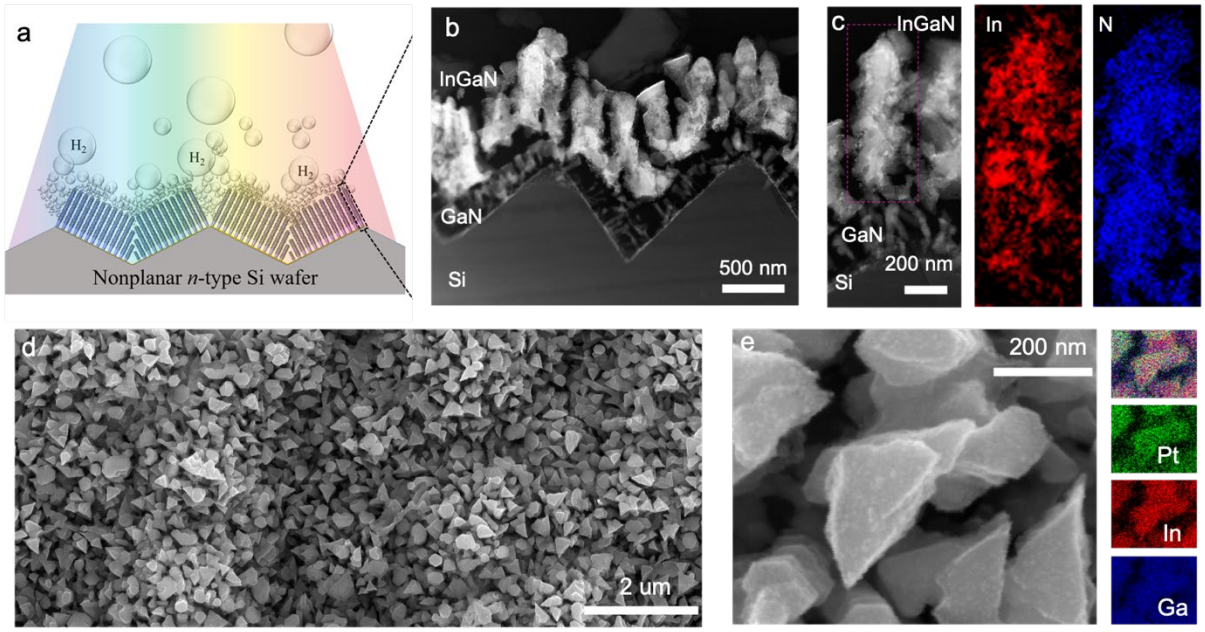

Figure 4.5 Hierarchical architectures of Pt-decorated InGaN nanowires[3]. **a** Schematic of proton reduction on p-InGaN nanowires on a nonplanar Si wafer. **b** Top-view SEM image with EDX elemental mapping, where Ga-L, In-L, and Pt-M characteristic X-ray spectra were measured. **c** HAADF-STEM image of cross-sectional InGaN nanowires with simultaneous EELS mapping images of In and N atoms. **d** Atomic resolution HAADF-STEM image highlighting the crystalline lattice spacing consistent with InGaN crystal and the Pt nanoparticles adsorbed onto InGaN surface [Y. Wang et al. Ref. 3].

Using the characteristic X-rays obtained on pure GaN as a reference specimen, the elemental composition of InGaN was quantitatively estimated, showing that 62.7 ± 10.5% of Ga and 37.3 ± 10.5% of In are present in the InGaN nanowire. Figure 4.6a shows the atomic structure within a InGaN nanowire and a lattice spacing of 2.63 Å corresponding to the InGaN (002) wurtzite lattice planes along the preferred <0001> growth direction (c-axis)[5]. In the low-dimensional geometry heteroepitaxy, increased In incorporation can occur due to the onset of strain relaxed growth[165]. The low substrate temperature (530-670 ºC) and relatively high N_2

flow rate (1 sccm) used for InGaN growth combined with 1D nanowire geometry allow for effective strain relaxation and reduce phase separation. Furthermore, Pt co-catalysts with a size of 2-6 nm were uniformly loaded on InGaN nanowire surface to further enhance the performance (Fig. 4.5e, 4.6a,b).

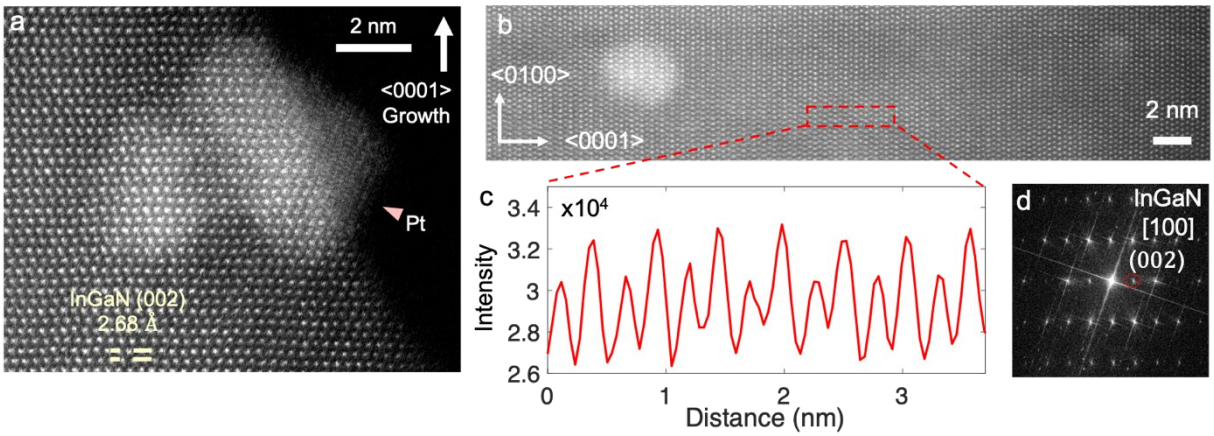

Figure 4.6 Atomic resolution HAADF-STEM of Pt-decorated InGaN nanowires. **a** Atomic resolution HAADF-STEM image highlighting the crystalline lattice spacing consistent with InGaN crystal and the Pt nanoparticles adsorbed onto InGaN surface. **b** Periodic ordering of In and Ga atoms in InGaN crystal. **c** HAADF intensity profile of the atomic ordering **d** Fast Fourier transform (FFT) of the InGaN nanowire in (a) shows the superlattice peak (*circled*) associated with atomic ordering in wurtzite InGaN along *c*-plane direction.

High resolution HAADF-STEM and HAADF intensity profile on the red box shows periodic atomic ordering along the c-axis caused by a nonrandom atomic site occupancy of indium and gallium (Fig. 4.6b,c). Fast Fourier transform (FFT) patterns of the HAADF-STEM image exhibit InGaN (001) reflection peak which is a forbidden peak in electron diffraction pattern of wurtzite hexagonal symmetry (Fig. 4.6d). The reflection peak demonstrates the existence of periodic atomic ordering along the c-axis caused by a nonrandom atomic site occupancy of indium and gallium within the two unique cation sublattice positions ((0,0,0) and (1/3,2/3,1/2)) in a wurtzite unit cell[170]. This confirms the periodic ordering of In and Ga in the crystalline InGaN nanopillars.

4.3.3. Fin-shaped InGaN Nanoridge through 1D Lithographic Templating

InGaN crystals can also be grown with hierarchical order that spans the nano- to atomic-scale through 1D lithographic templating[6] (Fig. 4.7a-c). Cross-sectional electron microscopy shows the periodic GaN nanowalls (width ~500 nm, height ~1 um, spacing ~400 nm) that template confined InGaN growth (Fig. 4.7a). InGaN grows as triangular prisms atop each nanowall (Fig. 4.7a) because the polar facet (001) has a faster growth rate than that of the semi-polar (101) and non-polar (100) facet sidewalls. It is also interesting that a sharply faceted single crystal InGaN nanoridge (~50 nm width) forms along the top of each nanowalls (Fig. 4.7c). In confined geometry heteroepitaxy, increased In incorporation can occur due to the onset of 'strain relaxed growth'[165]. An energy dispersive x-ray (EDS) map shows that the InGaN nanoridge is composed of Ga, In, and N without phase segregation (Fig. 4.7b). Atomic resolution dark field

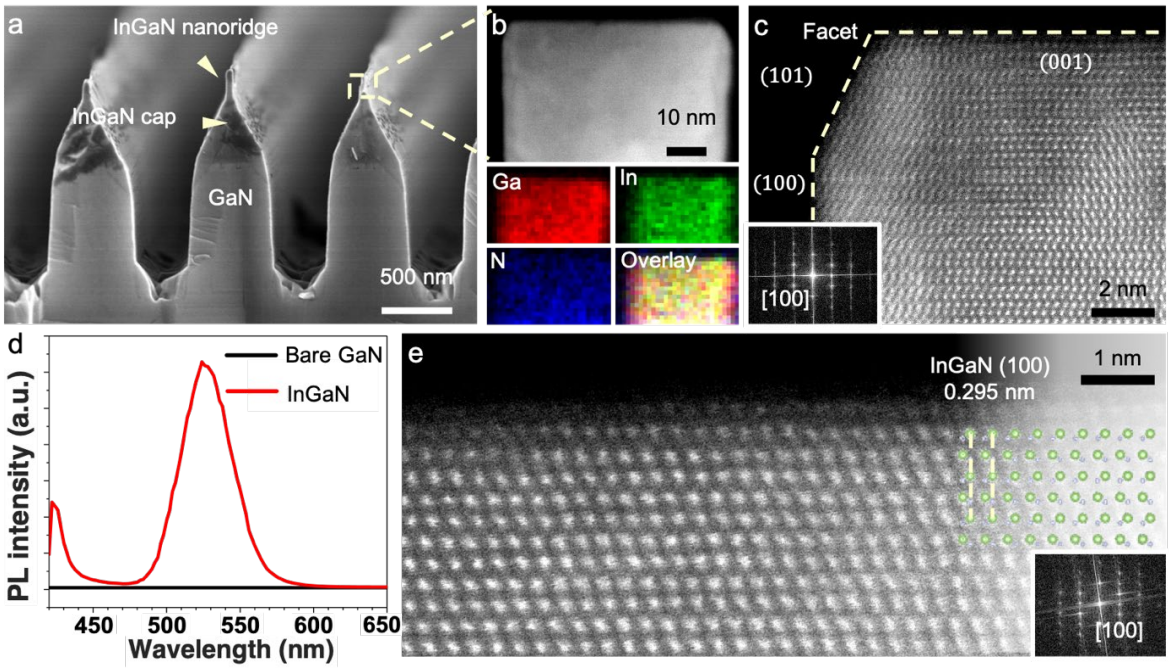

Figure 4.7 Single crystal 1D InGaN nanoridge grown on GaN wall[6]. **a** Side-view SEM **b** HAADF STEM image on cross-sectional InGaN nanowalls and simultaneous STEM EDS spectroscopic mapping showing the grown InGaN tip primarily comprised of Ga (red), In (blue), and N (green). **c** High resolution HAADF STEM on the sharply-faceted InGaN nanoridge in c indicating highly single crystalline. **d** Room temperature micro-PL of InGaN nanowalls and reference GaN wall. **e** Atomic resolution HAADF STEM on the termination of the InGaN tip in c indicating the lattice constant that is consistent with InGaN [Y. Park et al. Ref. 6].

STEM reveals a lattice spacing of 2.95Å (Fig. 4.7e) and confirms an In-rich InGaN crystal (InN spacing is 3.06 Å).

Under optimized growth conditions, PL emission from this InGaN nanoridge structure exhibits much higher intensity than InGaN grown on a planar structure or spontaneously formed InGaN nanowire arrays (Fig. 4.7d). Detailed structural study of this growth regime over the growth time clearly shows the structural evolution of the bulk triangular InGaN nanoprism into a very narrow, fin-shaped InGaN nanoridge. Atomic-resolution HAADF STEM and simultaneous STEM EDS spectroscopic mapping also suggests that this InGaN nanoridge structure is single crystalline with homogeneous In distribution. We envision that our integration of top-down and bottom-up approaches to obtain single-crystalline InGaN nanoridges with high In content will emerge as a viable architecture for designing a broad range of III-nitride devices. Moreover, further reducing the dimensions to the nanometer range may provide an extremely scaled quantum material platform for next-generation ultrahigh efficiency electronic, photonic, and solar energy devices and systems.

CHAPTER V

AlGaN 2D Multilayers for High-efficiency Ultraviolet Light-Emitting Diodes

5.1. Ultraviolet Light Emitting Diodes

Deep-ultraviolet (UV) light sources are important for high density-optical storage, artificial photosynthesis, sterilization, and water purification, in addition to solid-state lighting[7,10-12,171]. III-nitride semiconductors have emerged as the materials of choice for a broad range of device applications, including optoelectronics in the ultraviolet (UV) and visible regions and high power and high frequency electronics[36-39]. Semiconductor optoelectronic devices offer an alternative that is nontoxic, more compact, and more flexible in applications. The AlGaN alloy system is uniquely suited for this purpose, as the alloys are direct bandgap semiconductors spanning from ~200 to ~365 nm in wavelengths[171]. To date, AlGaN light-emitting diodes (LEDs) operating in the UV-C band (200–280 nm), which is of prime importance for sterilization, exhibit low efficiency, which has been attributed to the poor light extraction associated with transverse magnetic (TM)-polarized light emission[172-175], low luminescence efficiency due to the presence of large densities of defects[176,177], and inefficient p-type doping [178-180]. These issues become more severe for LEDs operating at shorter wavelengths, which require higher Al content in the device active region. In this regard, intensive studies have been performed to improve the light-extraction efficiency by engineering the energy band structure[181,182] and by utilizing nanostructures[183-186].

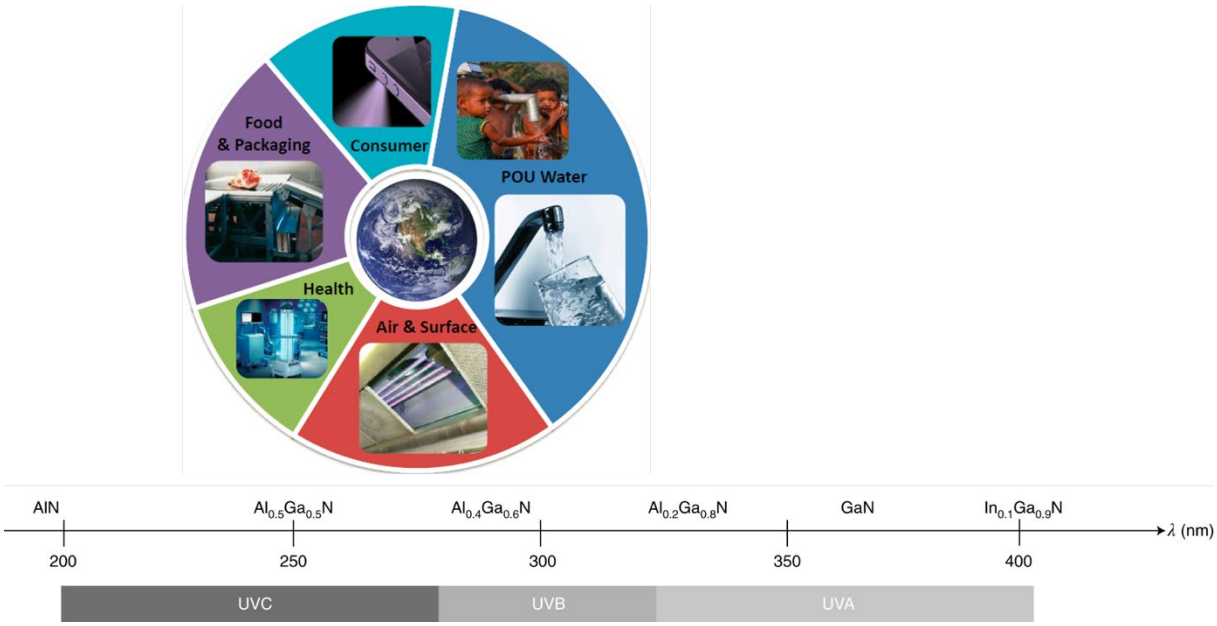

Figure 5.1 Applications of UV light emitting diodes using AlGaN materials[171] [adapted from Ref. 171].

Various techniques, including epitaxy on nanopatterned substrates and high-temperature annealing, have also been developed to reduce the formation of defects[187-190]. Recently, external quantum efficiency (EQE) over 20% was reported for AlGaN LEDs operating at 275 nm, which, however, had a low wall-plug efficiency (WPE) of 5.7%[191]. To our knowledge, the best reported EQE for AlGaN LEDs operating at ~265 nm, an important wavelength for water purification and sterilization[192], is ~6.3% for packaged devices grown using metal–organic chemical vapor deposition (MOCVD)[193,194]. Direct on-wafer measurements, however, typically result in lower efficiencies due to reduced light extraction/collection and severe self-heating of the devices, with the best peak EQE of only ~2% at ~265 nm[195,196]. The maximum wall-plug efficiency of these devices is often much lower, which is fundamentally limited by the large resistance and poor hole injection efficiency, due to the high resistivity of p-type AlGaN. Moreover, the poor p-type conduction, together with the highly asymmetric hole and electron injection efficiencies, can lead to parasitic carrier recombination outside the active region[197,198], which further

exacerbates the heating of the devices and can have a detrimental impact on device performance[199-202]. While using p-GaN as the contact layer may partly alleviate the issue of hole injection to the active region, it has an adverse impact on light extraction efficiency, due to the significant UV light absorption by GaN[203].

5.2. 2D Nanostructures Grown by Molecular Beam Epitaxy

Different type of multilayer at nano- and atomic- scale improve quantum efficiency of Al-rich LEDs. Tunnel junction structure is used to improve hole injection into the valence band of the p-type layer by the inter-band tunneling of electrons to the conduction band of an n-type layer. Multiple quantum-well also improve the efficiency by reducing the electron leakage caused by the low hole concentration. It increases the effective barrier height of the electron blocking layer compared to a single quantum well because the electron barrier height of the single well is determined by the bandgap of the barrier material, and it is not sufficiently high for UVC LED with wavelength shorter than 260 nm. In principle, emission in the deep-UV wavelengths can also be obtained from GaN layers of thickness 1−2 atomic monolayers (MLs), sandwiched by AlN or AlGaN barrier layers. The quantum confinement energy of carriers in such a “thin” quantum well has been shown to be large, leading to a large electronic bandgap in the deep-UV range[179,204-207]. To date, however, due to the lack of native substrates at the economic scale, conventional III-nitride devices are often hetero-epitaxially grown on foreign substrates, such as Al_2O_3, Si, and SiC[208]. The resulting large lattice mismatch and large difference in thermal expansion coefficients produce stressed materials with high density threading dislocations, stacking faults, and point defects,[166,209] which severely limit the device performance.

Molecular beam epitaxy (MBE) offers distinct advantages over metal-organic chemical vapor deposition (MOCVD) to engineer tunnel junction deep UV LEDs, due to the much more efficient incorporation of Mg-dopant incorporation in wide bandgap AlGaN[8,210,211]. Moreover, by varying the growth conditions, nanoscale clusters can be formed in Al-rich AlGaN[212-215], which can provide strong carrier confinement and therefore effectively reduce nonradiative recombination as well as quantum-confined Stark effect (QCSE), resulting in high efficiency deep UV emission. Compared to MOCVD, molecular beam epitaxy (MBE) is a nonequilibrium growth process, which provides unique opportunities to achieve high-quality GaN and AlN epilayers. This is of importance for future realization of deep-UV LEDs using similar growth methods with high Al compositions. In this chapter, we discuss various structure of AlGaN deep-UV LEDs characterized by atomic resolution Z-contrast imaging. AlGaN/GaN/AlGaN tunnel junction exhibits EQE of 11%[7] at ~265 nm and 7% at ~255 nm, which are higher than the previously reported[193-196,200,216]. GaN monolayer are formed between AlGaN barrier to build 4.785 eV in a good agreement with the calculated optical gap[10]. Graphene-assisted molecular beam epitaxy of AlN achieves EQE of 4% at ~260 nm[12].

5.3. Results and Discussion

5.3.1. $Al_{0.56}Ga_{0.44}N/Al_{0.62}Ga_{0.38}N$ Multiquantum Wells

High-angle annular dark-field scanning transmission electron microscopy (HAADF-STEM) show the cross-sectional overview of $Al_{0.56}Ga_{0.44}N/Al_{0.62}Ga_{0.38}N$ multiquantum wells grown by plasma-assisted molecular beam epitaxy[11] (Fig. 5.3a,b). Atomic resolution HAADF-STEM verifies the interface roughness on the three pairs of AlGaN MQW (Fig. 5.3c,d). The QW layers are ∼3 nm with ∼5 nm AlGaN barriers above and below (Fig. 5.3c). The brighter

HAADF intensity of the QWs reflects their increased Ga concentration (Ga elastically scatters more strongly than Al). Atomic-scale step edges at the terminating QW surfaces are shown in Fig. 5.3d with a height of ~0.3–1 nm (~1–3 atomic layers). The maximum height in this range agrees well with the calculated value of δ1 quoted earlier. HAADF-STEM collected across six different growth regions estimates the total growth thickness of the QW to be 2.9 nm ± 0.3 nm. The variation in thickness is due to the presence of ~1–3 atomic layers stepped on either top or bottom QW layers. We note, some Ga-rich atomic layers appear intermittently present within the Al-rich AlGaN barriers and buffer region. Similarly, Ga-rich termination was observed at the top and bottom plane of each quantum well. It is perhaps important to note that the effects of interface roughness might become more severe for $Al_xGa_{1-x}N/Al_yGa_{1-y}N$ quantum wells designed for emission at shorter wavelengths. This prediction is motivated by similar experimental studies made on GaAs-based systems, wherein the values of interface roughness have been found to increase with increasing values of Al composition in the barrier[217]. This phenomenon is partially exacerbated by the greater challenges introduced in the heteroepitaxy of III-V compound semiconductors having higher Al compositions. Temperature-dependent PL measurements on the MQW sample estimates internal quantum efficiency of ~30% assuming that non-radiative channels are frozen at 13.5 K (Fig. 5.3e). The solid curve represents analysis of the measured data in accordance with the Varshni equation including localization effects[218]. Good agreement is observed with the values of α, β and σ listed in the figure. Here, σ is a parameter related to the Stokes shift of the luminescence. In particular, the value of $\sigma = 3.34$ meV suggests the presence of compositional inhomogeneities and localization effects, including those at the MQW interfaces.

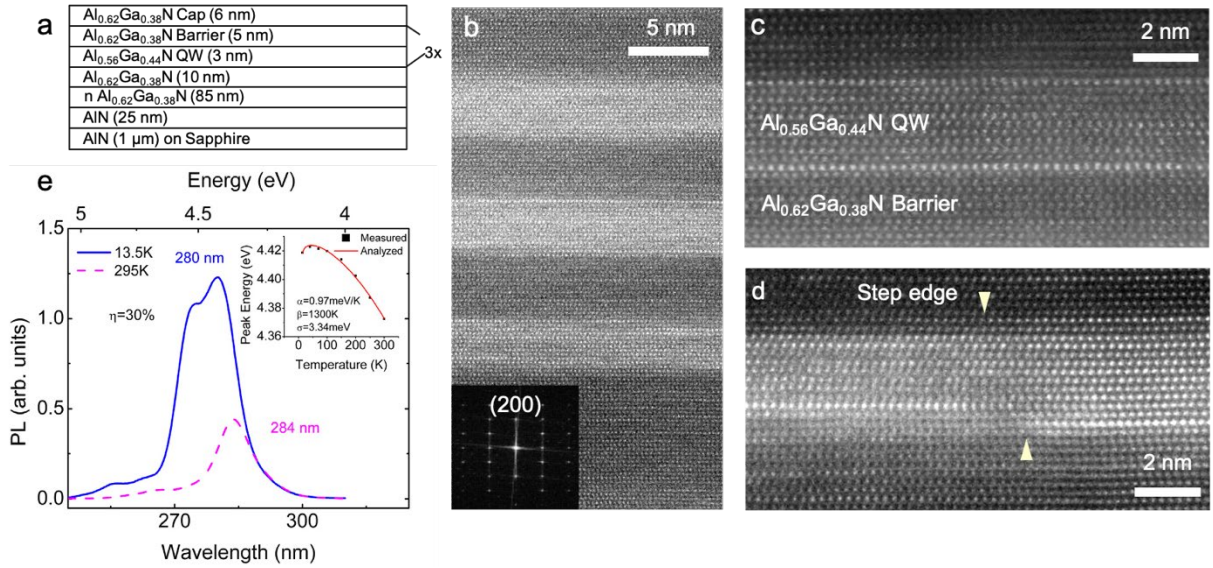

Figure 5.2 $Al_{0.56}Ga_{0.44}N/Al_{0.62}Ga_{0.38}N$ quantum wells with ~ 280 nm emission[11]. **a** schematic representation of the MQW heterostructure with three $Al_{0.56}Ga_{0.44}N/Al_{0.62}Ga_{0.38}N$ quantum wells grown over an AlN on sapphire template. **b** Quantum well AlGaN structure revealed in cross-section by HAADF-STEM. Three quantum wells of ~3 nm is separated by ~5 nm AlGaN barriers. **c** Sharp interfaces at top and bottom of QW. **d** Step edges commonly occurred with step sizes of 1–3 unit cells. Growth direction upward along vertical. **e** low-temperature photoluminescence of the MQW heterostructure with the temperature-dependent Varshni analysis [A. Aiello et al. Ref. 11].

5.3.2. Monolayer $GaN/Al_{0.65}Ga_{0.35}N$ Planar Heterostructures

The monolayer $GaN/Al_{0.65}Ga_{0.35}N$ planar heterostructure exhibits extreme quantum confinement[10] (Fig. 5.4a). Atomic-resolution HAADF-STEM indicate that the GaN layer thickness in the planar sample is ~1−2 ML (Fig. 5.3b,c). The HAADF intensity profile for each STEM image suggests that the nanowire interface is cleaner than that of the planar sample. Note the slow increase of background intensity in Figure 5.3b is due to thickness changes in the specimen. The ML quantum well in Figure 5.3b was imaged in a separate specimen grown under the same conditions and chemistry. Arrows indicate interface roughness, which is expected for these planar layers with large lateral extent, as opposed to nanowires, which may vary 1-2 ML. Additional HAADF-STEM shows the single layer, double, and multiple $GaN/Al_{0.65}Ga_{0.35}N$ layers (Fig. 5.3d,e). HAADF-STEM was collected using a Cs aberration corrected JEOL

3100R05 microscope (300 keV, 22 mrad) with a detector angle from 74 to 200 mrad.

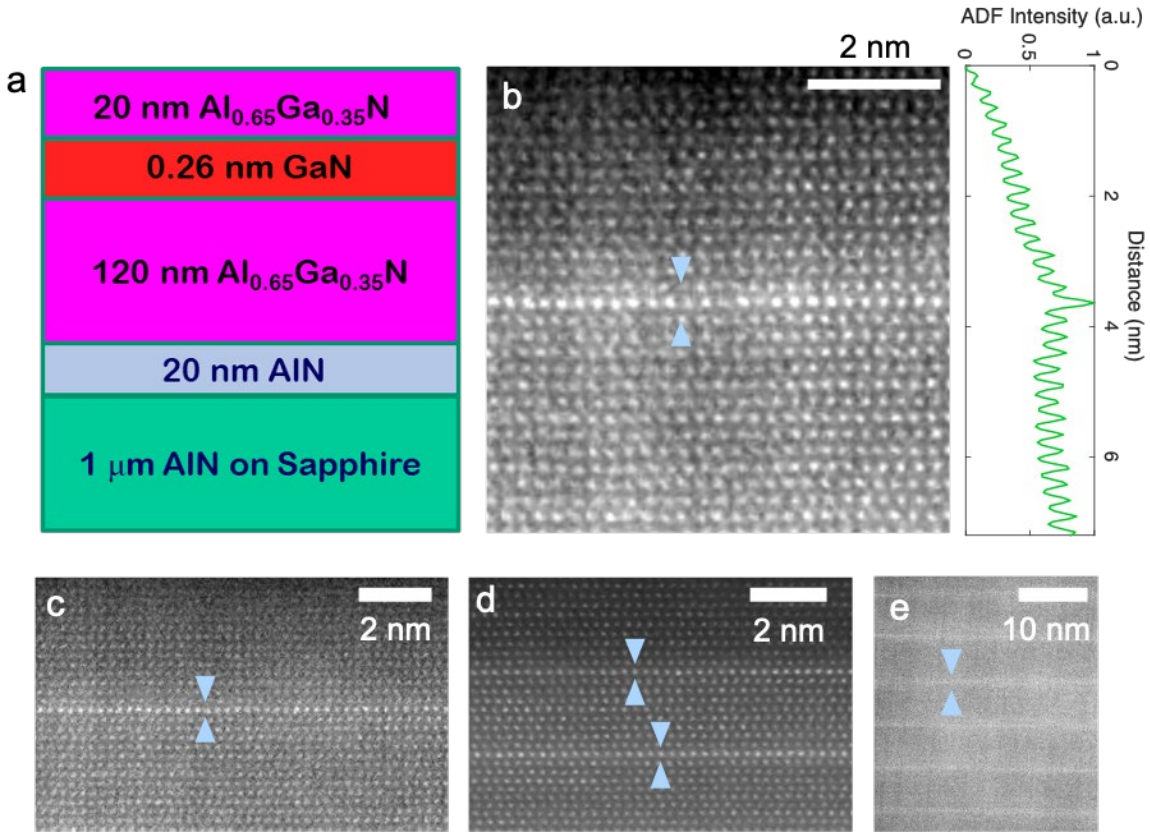

Figure 5.3 GaN monolayer in a planar $Al_{0.65}Ga_{0.35}N$ heterostructure[10]. **a** Schematic heterostructure and **b,c** high-angle annular dark-field (HAADF) STEM image of the monolayer GaN in a planar GaN/$Al_{0.65}Ga_{0.35}N$ heterostructure. Integrated HAADF profile intensity shown alongside image. **d** 2-period planar GaN/AlGaN monolayer structure **e** multiple GaN/$Al_{0.65}Ga_{0.35}N$ periods [A. Aiello et al. Ref. 10].

The measured emission peak at 300 K is 4.785 eV and in good agreement with the calculated optical gap of 4.68 eV and 95 meV below the calculated electronic gap of 4.88 eV (Fig. 5.5). Structure and band diagram of GaN/$Al_{0.67}Ga_{0.33}N$ heterostructure are calculated by density functional theory (DFT)[219] in Fig. 5.5a. Extreme quantum confinement effect increases the electronic gap of GaN to 4.88 eV and blueshifts the luminescence into the deep UV. Electron and hole wave functions ($|\psi|^2$ solid lines) are localized in the monolayer GaN well. Polarization-field-induced separation of electrons and holes reduces the overlap of electron and hole envelope functions ($|\psi|^2$ dashed lines). PL peak energy with temperature follows the Varshni

equation, where E_0, α, and β are 4.87 eV, 1.88 meV/K, and 1600 K respectively (Fig. 5.5.b). That's because carrier confinement in localized states at very low temperatures and their redistribution to GaN ML states at higher temperatures are very small.

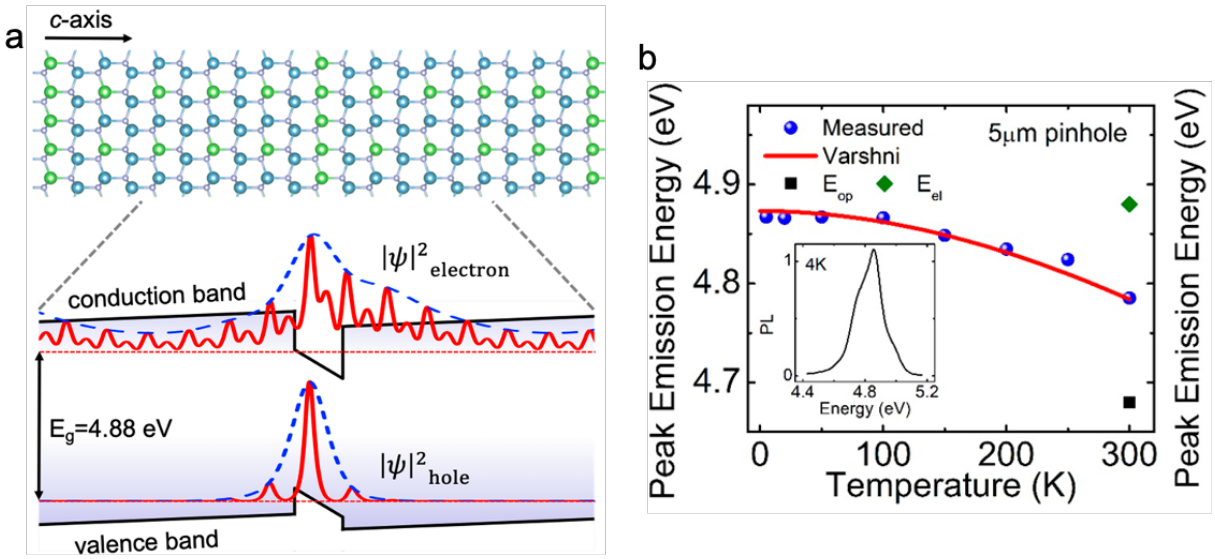

Figure 5.4 Band diagram and variation of PL peak emission in GaN/$Al_{0.67}Ga_{0.33}N$ heterostructure[10]. **a** Structure and band diagram of GaN/$Al_{0.67}Ga_{0.33}N$ heterostructure along the c-axis. **b** Variation of PL peak emission energy with temperature in planar monolayer GaN sample with the measured spectra shown in the inset. The calculated variation in accordance with the Varshni equation and the calculated electronic and optical gaps are also shown [A. Aiello et al. Ref. 10].

5.3.3. AlGaN/GaN/AlGaN Tunnel Junction

The epitaxy of AlGaN deep UV LEDs operating at ~265 nm is directly measured by aberration-corrected STEM[7]. HAADF-STEM confirms the AlGaN multilayer structure with p-AlGaN/GaN/n-AlGaN tunnel junction and AlGaN quantum well layers (Fig 5.6a). The GaN layer (~5 nm) is epitaxially grown between the top n-AlGaN contact and p-AlGaN layer with sharp interfaces (Fig 5.6b). The ratio of HAADF STEM intensity estimates ~64% $\pm$ 6% less Ga in the p-AlGaN layers compared with the Ga concentration in the GaN layer. The high relative Ga content in the tunnel junction is expected to increase the efficiency of charge carrier injection by tunneling; it is demonstrated by the equilibrium band diagram of the tunnel junction

LED structure simulated by Poisson- Schrödinger solver (Fig 5.6d). The grading down from 80% to 65% of the Al composition of the AlGaN provides polarization-induced doping, which enhances the hole concentration[152]. High-resolution cross-sectional STEM also confirms the epitaxial growth of four AlGaN quantum wells (~2 nm) with ~27% $\pm$ 3.5% higher content of Ga relative to adjacent AlGaN barriers (ranging from ~5 nm to ~3 nm) that confine charge carriers (Fig 5.6c). Fast Fourier transform (FFT) of the atomic resolution HAADF STEM images confirms the (100) lattice plane of AlGaN multilayers with an orientation that indicates preferred growth along the [001] c- axis direction. Relative gallium concentration in GaN tunnel junction and AlGaN quantum well/barrier layers was formulated by the HAADF intensity[220] along [100] defined by

$$I_{HAADF} = t \cdot [(f_{Ga}Z_{Ga} + f_{Al}Z_{Al})^{\gamma} + Z_N{}^{\gamma}]$$

where I_{HAADF} is the high-angle annular dark field intensity, t is the cross-section thickness, f is the concentration of Ga or Al in the AlGaN multilayers, Z is the atomic number of Al, Ga, or N in the layers, and γ is between 1.4 and 1.7. HAADF-STEM was collected using a Cs aberration corrected JEOL 3100R05 microscope (300 keV, 22 mrad) with a detector angle from 74 to 200 mrad. GaN layer thickness ~5 nm shows the maximum EQE, 9.8% and is optimum for the presented tunnel junction structures (Fig. 5.6e). This could be due to the degraded material quality with the incorporation of a thicker GaN layer, whereas a thinner GaN layer may not provide sufficiently strong polarization. Moreover, a thicker GaN layer also increases the absorption of UV light emission from the device's active region. A thick GaN layer would also present an obstacle to carrier transport due to the increased distance that electrons would need to tunnel across.

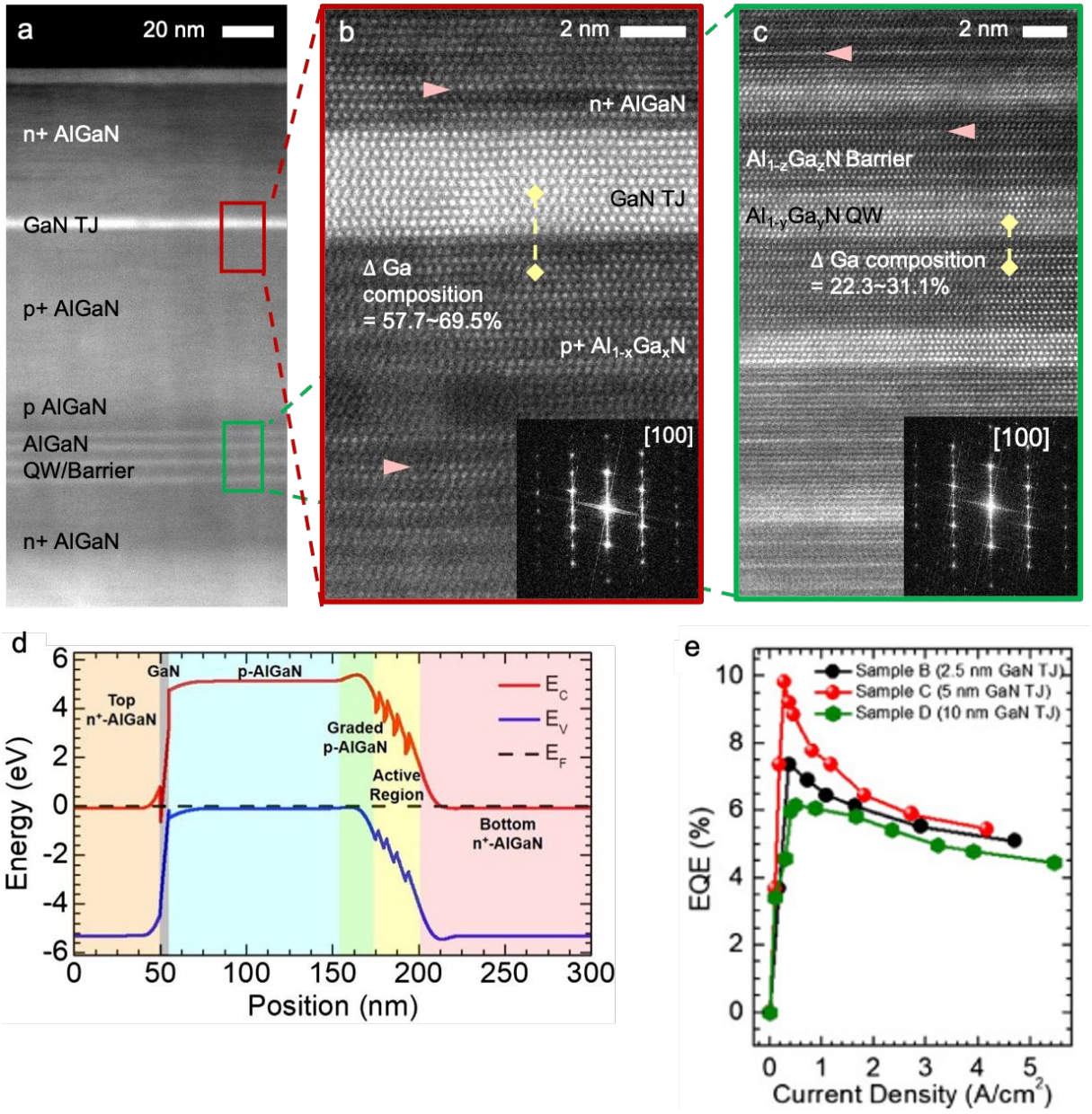

Figure 5.5 Structure and performance of AlGaN/GaN/AlGaN Tunnel Junction operating at ~265 nm[7]. **a** HAADF-STEM overview of cross-sectional AlGaN multilayers shows the complete device structure consistent with the device design. **b** High-resolution HAADF-STEM of the p-AlGaN/GaN/n-AlGaN tunnel junction shows crystalline epitaxial growth with sharp interfaces for enhanced hole injection by tunneling. **c** Atomic-resolution HAADF-STEM of $Al_{0.6}Ga_{0.4}N$ quantum wells coupled to $Al_{0.85}Ga_{0.15}N$ barriers with sharp epitaxial interfaces for carrier confinement. **d** Simulated equilibrium band diagram for a representative LED using a 5 nm GaN layer within the tunnel junction. The different layers used in the structure are labelled and shown with different colors. **e** Variations of EQE with injected current density, for Samples B, C, and D [A. Pandey et al. Ref. 7].

AlGaN-based UV LEDs also operates at ~255 nm and is achieved by slightly Ga-rich

conditions to promote the formation of nanoscale clusters in the active region (Fig 5.7a) [A. Pandey et al, APL accepted (2020)]. The nanoscale clusters are directly measured by atomic-resolution high-angle annular dark-field scanning transmission electron microscopy (HAADF-STEM). It shows the ordering of Ga-rich atomic layers in the $Al_{0.75}Ga_{0.25}N$ layer; it indicates the presence of compositional non-uniformity within the layer and is consistent with previous reports (Fig. 5.7c,d). Low frequency background was removed to reduce contrast loss to thickness variation. The device exhibits highly stable emission at ~255 nm, with virtually no change in the peak emission for injection current density up to 200 A/cm^2. It is attributed to the radiative emission originating from highly localized carriers in Ga-rich regions formed in the active region.

With the incorporation of an AlGaN/GaN tunnel junction, we have demonstrated 255 nm deep UV LEDs with a maximum EQE of 7.2% which are nearly one to two orders of magnitude higher than those reported previously for tunnel junction LEDs operating at this wavelength[200,216] (Fig 5.7b). Fast Fourier transform (FFT) patterns of the HAADF-STEM images exhibit ordering of Ga-rich layer along [001] direction; the peaks are forbidden in electron diffraction pattern of wurtzite hexagonal symmetry. While the Ga-rich growth conditions have distinct advantages, prolonged growth in this regime can lead to the formation of crystalline defects due to the presence of gallium droplets on the sample surface. HAADF-STEM was collected using a Cs aberration-corrected JEOL 3100R05 microscope (300 keV, 22 mrad) with a detector angle from 74 to 200 mrad.

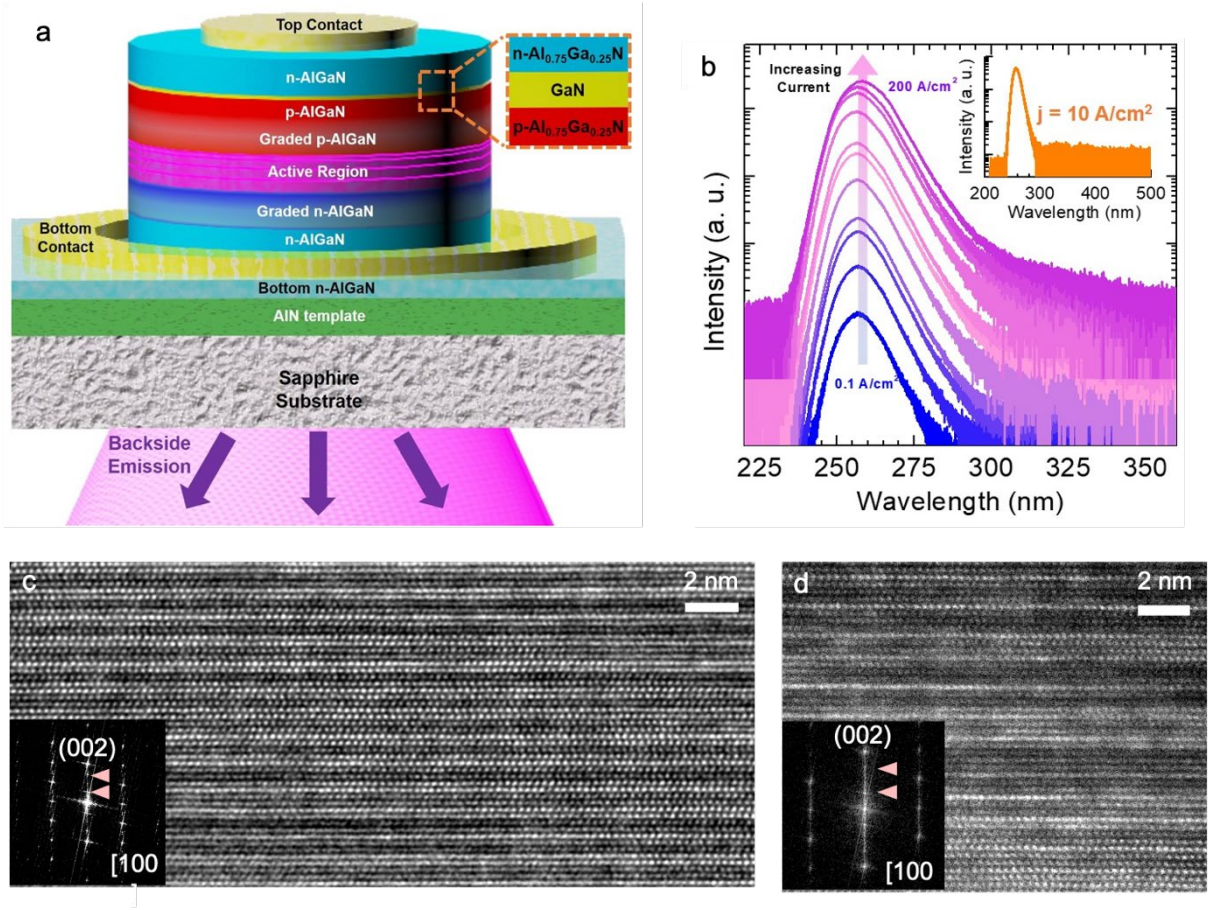

Figure 5.6 Modified AlGaN/GaN/AlGaN Tunnel Junction operating at ~255 nm[9]. **a** Schematic tunnel junction deep UV LED. The tunnel junction is shown in the marked region. **b** Room-temperature electroluminescence spectra measured at different injection currents. Inset: electroluminescence spectrum at an injection current of 10 A/cm^2 measured from 200 nm to 500 nm, showing the absence of defect-related emission. **c,d** Atomic scale HAADF-STEM images of an $Al_{0.75}Ga_{0.25}N$ layer showing the presence of nanoscale Ga-rich layers due to compositional variation. The brighter regions correspond to higher Ga content. FFT shows the superlattice peak (red arrows) associated with atomic ordering in wurtzite AlGaN along c-plane direction [A. Pandey et al. Ref. 9].

5.3.4. Graphene-assisted MBE of AlN for AlGaN Deep-UV LEDs

The van der Waals epitaxy (vdWE) of AlN on graphene is directly measured by scanning transmission electron microscopy (STEM)[12]. High-quality single crystalline AlN grown on Gr was achieved through controlled nucleation by migration enhanced epitaxy (MEE) on Gr. The effect of the crystallographic structure underneath Gr on the vdWE of AlN is explored using Gr/sapphire and Gr/AlN templates as substrates. Cross-sectional high-angle annular dark field

scanning transmission electron microscopy (HAADF- STEM) confirms the epitaxial registry from the underlying template. The HAADF-STEM images highlight the AlN/Gr/AlN structure showing the interface density consistent with the lighter atomic weight of carbon (Figs. 5.8a, b). The atomic-resolution STEM reveals the highly parallel epitaxial relationship of the AlN epilayer with the AlN template beneath Gr exhibiting the stacking manner of Al atoms is consistent on both sides of the Gr layer nearly without any shift or rotation (Fig. 5.8b). Fast Fourier transform (FFT) of the HAADF-STEM image in the interface region illustrates a highly single crystalline wurtzite structure, indicating that AlN/Gr/AlN share the same crystallographic orientation (Fig. 5.8c). Although a carbon layer is clearly visible in the STEM image (a projection of the crystal), the Gr lattice was not noticeable, and the layer thickness corresponds to ~1 nm—likely due to the defects generated during the growth and the atomic steps on the AlN template surface.

Bright field STEM image of the AlN/Gr/AlN interface shows two filtering effects of the threading dislocations. The reduction of edge dislocations is likely attributed to (i) the lattice continuity of conventional epitaxy that is interrupted by the Gr layer and van der Waals interface, providing a possible path to block the propagation of edge dislocations from the underlying AlN template; (ii) the three-dimensional nucleation, which is often used in Al(Ga)N epilayer growth, offering another approach to reduce the edge dislocations[221]. Dislocations marked by green arrows were blocked at the interface from the underlying substrate. Most of the new dislocations generated from the interface (red arrows) terminate near the initial 30-nm-thick nucleation region and the following coalescence region (yellow arrows). The dislocations labelled by brown arrows penetrate the Gr layer and extend into the top AlN layer.

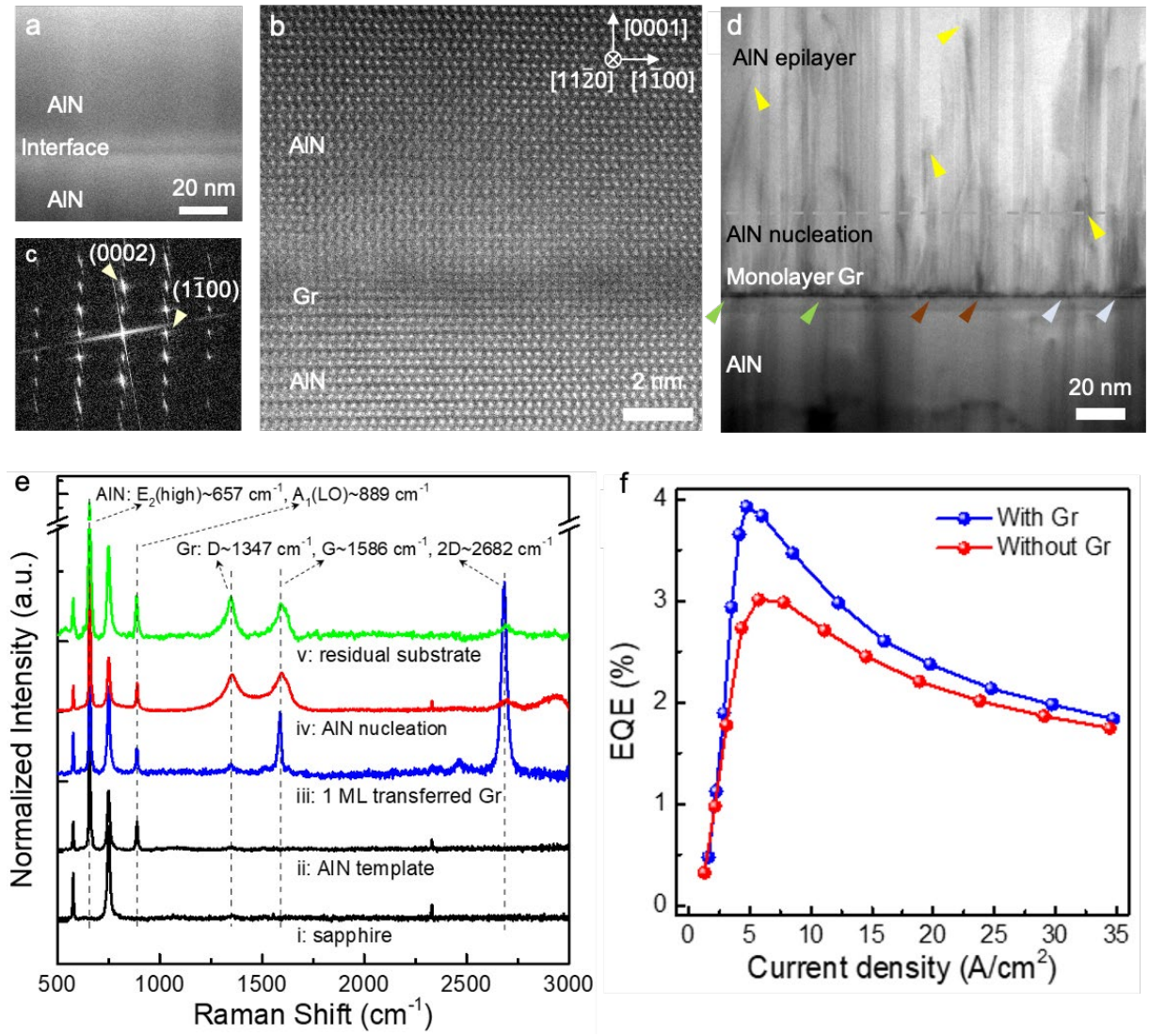

Figure 5.7 Graphene-assisted molecular beam epitaxy of AlN for AlGaN deep-UV LEDs[12] **a** HAADF-STEM overview of the cross-sectional AlN/Gr/AlN structure shows a darker contrast consistent with a carbon layer. **b** Atomic-resolution HAADF-STEM on the interface exhibiting the parallel epitaxial relationship of the top AlN. **c** FFT of the atomic-resolution image presented in (b) indicating the crystallographic orientation of the AlN epilayer consistent with that of the underlying AlN template. **d** The evolution of dislocations for AlN/Gr/AlN template. The green, brown, and red arrows represent the annihilated, penetrated, and new generated dislocations at the AlN/Gr/AlN interface, respectively, while the yellow arrows correspond to the bended or terminated dislocations near the nucleation region and the following coalescence region. **e** Comparison of Raman spectra at different stages **f** EQE versus current density of deep-UV LEDs with and without Gr interlayer [P. Wang et al. Ref. 12].

Raman spectroscopy presents two characteristic peaks at the G band (1586 cm^{-1}) and 2D band (2682 cm^{-1}) on the transferred Gr, but the defect-related D band peak (1347 cm^{-1}) is negligible (Fig. 5.8d). The intensity ratio of 2D peak to G peak (I_{2D}/I_G) is around 2, confirming

that it is single layer Gr (Fig. 5.8d-iv). The Raman spectrum acquired after the AlN nucleation exhibits clear peaks of the D band and G band with a dramatic reduction of the 2D band peak. It confirms the presence of Gr after the epitaxy of AlN although the defects increased on the Gr surface after AlN epitaxy. To further confirm the high material quality of AlN, AlGaN- based deep-UV LED structures were grown on the AlN/Gr/AlN template. The maximum measured EQE is 4% for deep-UV LEDs on Gr, which is significantly higher than that of the LEDs without the Gr interlayer (3%), and it is among the best reported values for AlGaN deep-UV LEDs operating at this wavelength[39]. The improved device performance may originate from the reduction of dislocations and defects, as well as the relaxation of strain[221-223].

The substrate/template beneath Gr plays a critical role in governing the initial AlN nucleation to form a high density of large-size nuclei with uniform in-plane domains. The strong surface electrostatic potential of the underlying AlN template enables a large-scale parallel epitaxial relationship for AlN/Gr/AlN. This epitaxial registry is further ver- ified by detailed RHEED and STEM studies. The high-quality AlN grown on Gr is also confirmed by the demonstration of AlGaN TJ deep-UV LEDs operating at ~260 nm, which exhibit a maximum EQE of 4% for the direct on-wafer measurement. Such devices can also be readily peeled off, thereby providing efficient thermal management and enabling high efficiency flexible deep-UV LEDs, high performance UV laser diodes, and high frequency and high-power electronics.

CHAPTER VI

Experimental Methods for Advanced TEM

6.1. Nano-Fabrication of TEM Grid

Using in-house fabrication of TEM grids, in situ TEM allows us to investigate exotic property of materials such as phase-transition with a change of applied electric bias or temperature. Stable wafer-scale fabrication of TEM grids with Si_3N_4 membranes through process flow described in Figure 6.1. The resulting grids fit well into commercial TEM holders and have windows and electrodes larger than that of commercial grids (Figure 6.2).

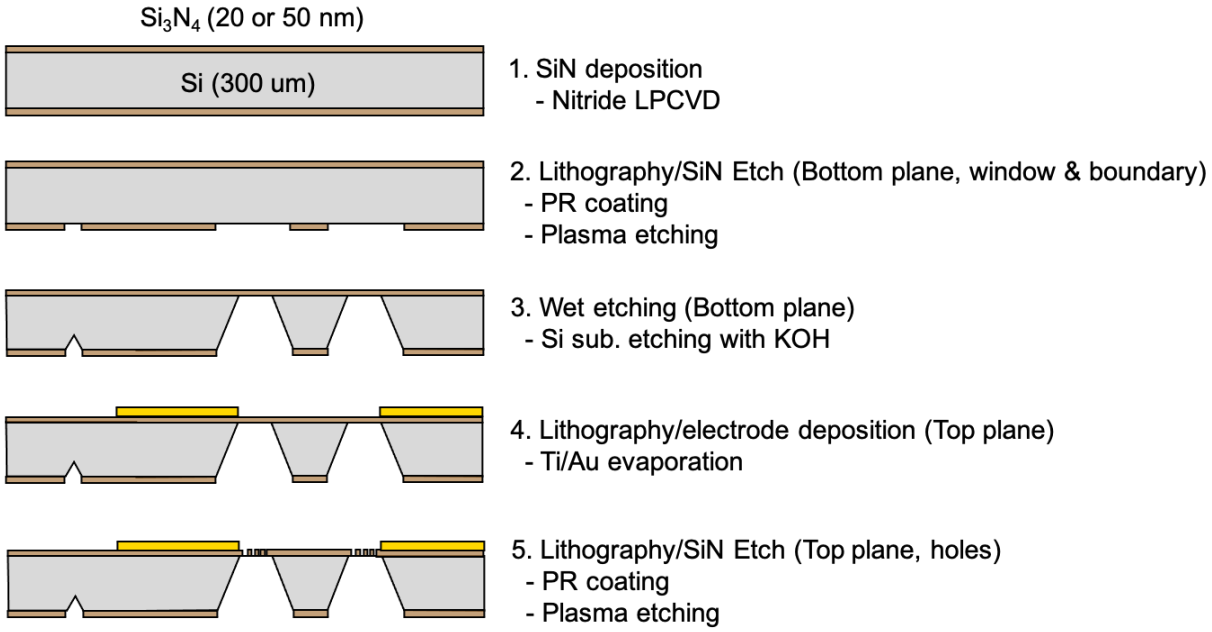

Figure 6.1 Process flow of in situ TEM grid. **(1)** The Si_3N_4 layer is formed via low-pressure chemical vapor deposition (LPCVD). **(2)** Patterning and plasma-etching for back Si_3N_4 layer to open windows. **(3)** potassium hydroxide (KOH) aqueous solution etches the back of the Si wafer all the way to the front Si_3N_4 membrane. **(4)** Patterning and deposition of Ti/Au electrodes. **(5)** Patterning and plasma etching of the front Si_3N_4 membrane to create nanopores.

Deposition of Si_3N_4 membrane. The schematic process flow is described in Figure 1.7. Using low-pressure chemical vapor deposition (LPCVD), we grow low stressed silicon nitride films on 6-inch 300 μm Si wafers. The growth condition is 700 ℃ with a rate of ~40 Å/sec. Tempress S2T4 furnace in Lurie Nanofabrication Facility (LNF) is a CMOS clean tool so the Si wafers need to be cleaned in Prefurnace Clean (PFC) Bench. The three-stage cleaning process composed of (1) a 5:1:1 mixture of water, ammonium hydroxide, and hydrogen peroxide at 85 ℃ (known as Standard Clean 1, SC-1, or the 'Organic' clean), (2) a brief etch in dilute, room temperature hydrofluoric acid (either 10:1 or 100:1), and (3) a 6:1:1 mixture of water, hydrochloric acid, and hydrogen peroxide at 85 ℃ (known as Standard Clean 2, SC-2, or the 'Ionic' clean).

The backplane etching by KOH solution for Si_3N_4 membrane window. Patterns for opening the Si_3N_4 window are applied on the back of the Si wafer. Based on the pattern, the Si_3N_4 layer on the back is removed by plasma-etching. KOH etching is an anisotropic Si etch process and conducted in Robin lab at LNF. The fastest etch plane is the <110> plane and <111> plane etches extremely slow because <110> has a highest polarity, resulting in <100> plane etched at 54.7 ° relative to the <111> plane. The etch rate for (110) surface in 50% KOH solution at 70 °C is ~ 0.87 μm/min. In order to make a target sized Si_3N_4 window on the top, the region open to be etched is required to be larger than the target sized depending on the thickness of wafer. For 300 μm wafer, the appropriate size for 100×100 μm window is $100+2\times300\times \frac{300\ \mu m}{\cos(90°-54.7°)} \cong$ 835 μm .

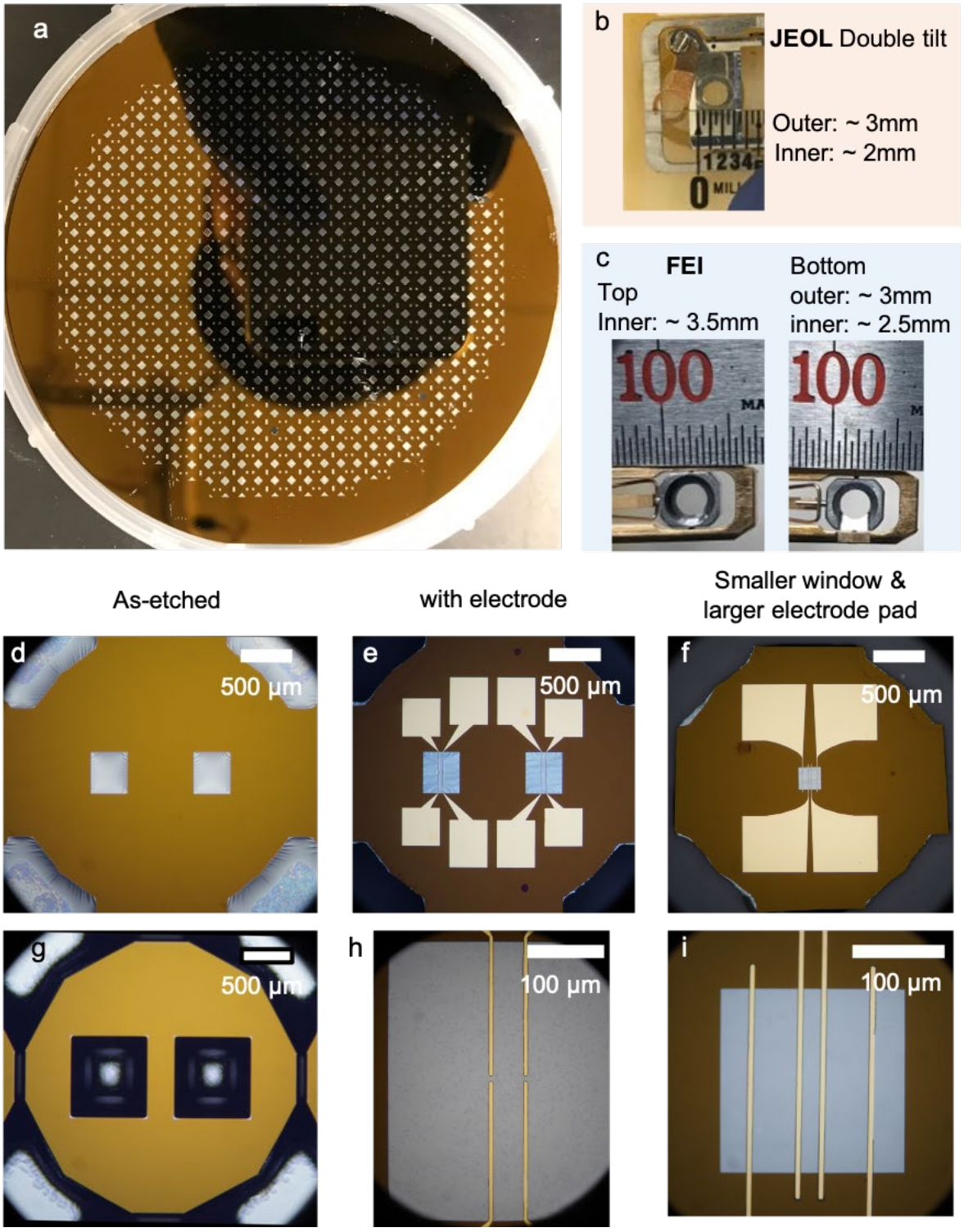

Figure 6.2 Fabricated in situ TEM grid with Si_3N_4 membrane. **a** Approximately 900 TEM grids fabricated in a 6 inch wafer. **b,c** Measurement of dimension for TEM holder head to avoid any mismatch between the fabricated TEM grid and the loading part. **d,g** Top and bottom of the as-etched grids. The shape of the grids is circle and the size is larger than the inner radius and smaller than the outer diameter, so it stably stays in the loading part. **e,f,h,i** Various size of window size and different number of windows and electrodes customized depending on the experimental plan such as tomography or external electrical bias setup.

Deposition of the electrode for electric contact. Patterns for the electrodes are applied on the top of the Si wafer. Using Angstrom Engineering Evovac Evaporator, 80 nm thick Ti/Au electrode is deposited with a ratio of 5:1; deposition of titanium is followed by gold. When we lift off the photoresist, we should gently rinse the wafer with Acetone because the Si_3N_4 window is only 20~50 nm that is easily damaged, resulting in a poor yield.

Creating nanopores for imaging. Patterns for the micropores are applied on the Si_3N_4 window at the top of the Si wafer. Using plasma-etching, we create micron-sized pores that avoid from Si_3N_4 background which is advantageous for atomic resolution imaging.

6.2. Wedge Polishing

Before polishing. We cut our material approximately in 3 mm × 3 mm as large as TEM grid because it needs to be fit in TEM grid after polishing. For the materials grown on a substrate such as thin films or nanowires, we should 'make a sandwich' of two pieces of material. The materials of our interest have to face each other with epoxy resins at the interface. We typically use M-bond 610 that is chemically resistant after curing and provides a thin layer of glue with good ion milling properties. The glue line is required to be as thin as possible because smaller interface provides better protecting of the materials from damage during polishing. Thus, we should clean the surface of the materials (i.e. your thin films or nanowires) before making a sandwich using chemicals such as Aceton and Methanol. Immediately after applying glues on the surface of the material, we should make a sandwich immediately, clamp it using alligator clips, and cure it on a 180 ℃ hotplate for 2 hours. For bulk materials such as mollusk shells or metal alloy, we dice it in a 3 mm × 3 mm piece.

First-side polishing. We mount the sandwich to an Allied aluminum stub in the direction in which the glue line is perpendicular to the stub using the Crystal Bond. We plan to polish the sample around 1 mm thick before second-side polishing. In order to mechanically polish the material, we use diamond lapping films that have diamond particles bonded to the surface grading from 0.1 μm to 60 μm. In general, the diamond lapping film remove the materials by a thickness approximately three times larger than its grade, i.e. the 30 μm film leaves at least 90 μm of damage to the polished surface. Hence, we should polish at least 90 μm to remove the scratches left by the 30 μm film.

We attach the diamond lapping film on the plate of Allied Multiprep polishing station by a rubber squeezer. We should calibrate the plate based on the standard procedure described in the Multiprep manual, and clean the surface using filtered water because any debris introduced between the film and the plate cause damages to the polishing surface. Using coarse diamond lapping films (> ~3 μm), we get the sandwich to be a little over 1 mm. Using smaller grit diamond films (1 μm, 0.5 μm, and 0.1 μm), we repeat fine polishing to achieves scratch-free surface. Appropriate load on the Multiprep polishing head is around 5-10 μm for coarce milling and 1-3 μm for fine milling as the value on the micrometer. Rotation speed of the plate is around 50-90 rpm for coarse milling and 20-40 rpm for fine milling. During polishing, we should remove polished debris by placing Kimwipes so that the debris don't introduce the next rotation of polishing. Once we get the scratch-free surface, the sandwich will be rinsed with Acetone and Methanol.

Second-side polishing. For second-side polishing, the sample is mounted to an Allied Pyrex flat using epoxy resin because the transparent stub allows us to see the thickness of the specimen using the transmitted light. For the epoxy resin, Cyanoacrylate super glue is

appropriate because it provides a thin layer with no trapped air bubbles. Using a toothpick or a pipet, we apply a small amount of the glue on the Pyrex and immediately mount the specimen with the polished plane facing down. The excess glue is gently removed by Kimwipes. Then, we cure the stub on a 180 ℃ hotplate for 1 hours.

We tilt the polishing head by ~2-4 ° and polish the second-side of the specimen. As the head approach to the plate, the front edge of the specimen gets thinner. When the specimen gets thinner than 60 μm, we switch to the 3 μm diamond lapping film to remove a large scratch for fine milling. Then we decrease the load to 0-2 μm to prevent damage from occurring at the edge of the wedge because the leading wedge is just tens of micron. We repeat find polishing with the 1 μm, 0.5 μm, and 0.1 μm lapping films until we see rainbow interference fringes along the glue line. If you see around 8-10 fringes, the leading edge is as thin as ~100 nm (Figure. 6.3).

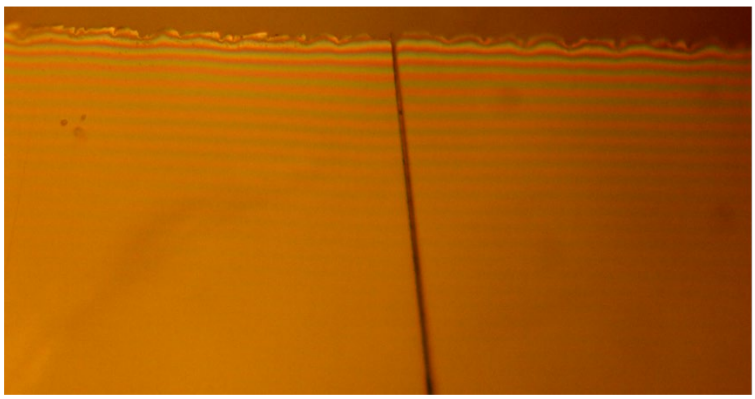

Figure 6.3 Wedge polished specimen of InGaN nanowires grown on GaN/sapphire substrate. The vertical line at the center is the glue line where the InGaN nanowires face each other.

Precise Ion Milling. For atomic resolution HAADF-STEM imaging, the specimen is needed to be thinner than 100 nm. In that case, we should apply ion-milling for the sample using PIPS (Precise Ion Polishing System). Ion beam is required to be aligned to the center of rotation and our region of interest also need to be aligned to the center of rotation. Ion gun is tilted by

~6-8 degree that is higher than the wedge angle. If gun angle is smaller than the wedge angle, the ion beam cannot reach to the specimen. For precise milling, we apply 3, 1, and 0.5 kV of voltage for ~1-3 min for each step. In general, it provides ~50 nm thickness that is electron-transparent even for low voltage below 100 kV.

BIBLIOGRAPHY

1 Gim, J. *et al.* Nanoscale deformation mechanics reveal resilience in nacre of Pinna nobilis shell. *Nature Communications* **10**, 4822, doi:10.1038/s41467-019-12743-z (2019).

2 J.Gim, A. K., L. Otter, B.H. Savitzky, S. Erland, L.A. Estroff, D.E. Jacob, R. Hovden. (submitted, 2021).

3 Wang, Y. *et al.* An In0.42Ga0.58N tunnel junction nanowire photocathode monolithically integrated on a nonplanar Si wafer. *Nano Energy* **57**, 405-413, doi:10.1016/j.nanoen.2018.12.067 (2019).

4 Wang, Y., Schwartz, J., Gim, J., Hovden, R. & Mi, Z. Stable Unassisted Solar Water Splitting on Semiconductor Photocathodes Protected by Multifunctional GaN Nanostructures. *ACS Energy Letters* **4**, 1541-1548, doi:10.1021/acsenergylett.9b00549 (2019).

5 Chu, S. *et al.* Solar Water Oxidation by an InGaN Nanowire Photoanode with a Bandgap of 1.7 eV. *ACS Energy Letters* **3**, 307-314, doi:10.1021/acsenergylett.7b01138 (2018).

6 Park, Y.-B., Gim, J., Yalisove, R., Hovden, R. & Mi, Z. Heteroepitaxy of Fin-Shaped InGaN Nanoridge Using Molecular Beam Epitaxy. *Crystal Growth & Design* **18**, 5750-5756, doi:10.1021/acs.cgd.8b01211 (2018).

7 Pandey, A., Shin, W. J., Gim, J., Hovden, R. & Mi, Z. High-efficiency AlGaN/GaN/AlGaN tunnel junction ultraviolet light-emitting diodes. *Photonics Research* **8**, 331-337, doi:10.1364/PRJ.383652 (2020).

8 Pandey, A. *et al.* Enhanced doping efficiency of ultrawide band gap semiconductors by metal-semiconductor junction assisted epitaxy. *Physical Review Materials* **3**, 053401, doi:10.1103/PhysRevMaterials.3.053401 (2019).

9 Pandey, A., Gim, J., Hovden, R. & Mi, Z. An AlGaN tunnel junction light emitting diode operating at 255 nm. *Applied Physics Letters* **117**, 241101, doi:10.1063/5.0036286 (2020).

10 Aiello, A. *et al.* Deep Ultraviolet Luminescence Due to Extreme Confinement in Monolayer GaN/Al(Ga)N Nanowire and Planar Heterostructures. *Nano Letters* **19**, 7852-7858, doi:10.1021/acs.nanolett.9b02847 (2019).

11 Aiello, A. *et al.* Optical and interface characteristics of Al0.56Ga0.44N/Al0.62Ga0.38N multiquantum wells with ∼280 nm emission grown by plasma-assisted molecular beam epitaxy. *Journal of Crystal Growth* **508**, 66-71, doi:10.1016/j.jcrysgro.2018.12.025 (2019).

12 Wang, P. *et al.* Graphene-assisted molecular beam epitaxy of AlN for AlGaN deep-ultraviolet light-emitting diodes. *Applied Physics Letters* **116**, 171905, doi:10.1063/1.5144906 (2020).

13 Lakes, R. Materials with structural hierarchy. *Nature* (1993).

14 Gao, H., Ji, B., Jäger, I. L., Arzt, E. & Fratzl, P. Materials become insensitive to flaws at nanoscale: Lessons from nature. *Proceedings of the National Academy of Sciences* **100**, 5597-5600, doi:10.1073/pnas.0631609100 (2003).

15 Snow, M. R., Pring, A., Self, P., Losic, D. & Shapter, J. The origin of the color of pearls in iridescence from nano-composite structures of the nacre. *American Mineralogist* **89**, 1353-1358, doi:10.2138/am-2004-1001 (2004).

16 Xu, F., Fu, C. & Yang, Y. Water Affects Morphogenesis of Growing Aquatic Plant Leaves. *Physical Review Letters* **124**, 038003, doi:10.1103/PhysRevLett.124.038003 (2020).

17 Espinosa, H. D., Rim, J. E., Barthelat, F. & Buehler, M. J. Merger of structure and material in nacre and bone – Perspectives on de novo biomimetic materials. *Progress in Materials Science* **54**, 1059-1100, doi:10.1016/j.pmatsci.2009.05.001 (2009).

18 Nalla, R. K., Kinney, J. H. & Ritchie, R. O. Effect of orientation on the in vitro fracture toughness of dentin: the role of toughening mechanisms. *Biomaterials* **24**, 3955-3968, doi:10.1016/S0142-9612(03)00278-3 (2003).

19 "File:GaN Wurtzite polyhedra.png" by https://commons.wikimedia.org/wiki/User:Solid_State is licensed with CC BY-SA 4.0. To view a copy of this license, visit https://creativecommons.org/licenses/by-sa/4.0

20 "Peacock Feather" by Thom Watson is licensed with CC BY-NC-SA 2.0. To view a copy of this license, visit https://creativecommons.org/licenses/by-nc-sa/2.0/

21 "Lotus leaf in the rainy season" by tanakawho is licensed with CC BY-NC 2.0. To view a copy of this license, visit https://creativecommons.org/licenses/by-nc/2.0/

22 "Collagen fibrils" is licensed with CC BY-NC 4.0. To view a copy of this license, visit http://creativecommons.org/licenses/by-nc/4.0/

23 "Intel@14nm@Skylake@Skylake-S@Core_i7-6700@SR2BT___Stack-DSC02930-DSC02972_-_ZS-retouched##"by FritzchensFritz is marked under CC0 1.0. To view the terms, visit https://creativecommons.org/licenses/cc0/1.0/

24 Wegst, U. G. K., Bai, H., Saiz, E., Tomsia, A. P. & Ritchie, R. O. Bioinspired structural materials. *Nature Materials* **14**, 23-36, doi:10.1038/nmat4089 (2015).

25 Roozeboom, F., Bruele, F. v. d., Creyghton, Y., Poodt, P. & Kessels, W. M. M. Cyclic Etch/Passivation-Deposition as an All-Spatial Concept toward High-Rate Room Temperature Atomic Layer Etching. *ECS Journal of Solid State Science and Technology* **4**, N5067, doi:10.1149/2.0111506jss (2015).

26 Garg, P., Ghatmale, P., Tarwadi, K. & Chavan, S. Influence of Nanotechnology and the Role of Nanostructures in Biomimetic Studies and Their Potential Applications. *Biomimetics* **2**, 7, doi:10.3390/biomimetics2020007 (2017).

27 Gilbert, P. U. P. A., Abrecht, M. & Frazer, B. H. The Organic-Mineral Interface in Biominerals. *Reviews in Mineralogy and Geochemistry* **59**, 157-185, doi:10.2138/rmg.2005.59.7 (2005).

28 Ritchie, R. O. The conflicts between strength and toughness. *Nature Materials* **10**, 817-822, doi:10.1038/nmat3115 (2011).

29 Wegst, U. G. K. & Ashby, M. F. The mechanical efficiency of natural materials. *Philosophical Magazine* **84**, 2167-2186, doi:10.1080/14786430410001680935 (2004).

30 Meyers, M. A., McKittrick, J. & Chen, P.-Y. Structural Biological Materials: Critical Mechanics-Materials Connections. *Science* **339**, 773-779, doi:10.1126/science.1220854 (2013).

31 Hovden, R. *et al.* Nanoscale assembly processes revealed in the nacroprismatic transition

zone of *Pinna nobilis* mollusc shells. *Nature Communications* **6**, 10097, doi:10.1038/ncomms10097 (2015).

32 Sun, J. & Bhushan, B. Hierarchical structure and mechanical properties of nacre: a review. *RSC Advances* **2**, 7617-7632, doi:10.1039/C2RA20218B (2012).

33 Jackson, A. P., Vincent Julian, F. V., Turner, R. M. & Alexander Robert, M. The mechanical design of nacre. *Proceedings of the Royal Society of London. Series B. Biological Sciences* **234**, 415-440, doi:10.1098/rspb.1988.0056 (1988).

34 Meyers, M. A., Chen, P.-Y., Lin, A. Y.-M. & Seki, Y. Biological materials: Structure and mechanical properties. *Progress in Materials Science* **53**, 1-206, doi:10.1016/j.pmatsci.2007.05.002 (2008).

35 Barthelat, F., Tang, H., Zavattieri, P., Li, C. & Espinosa, H. On the mechanics of mother-of-pearl: A key feature in the material hierarchical structure. *Journal of the Mechanics and Physics of Solids* **55**, 306-337, doi:10.1016/j.jmps.2006.07.007 (2007).

36 Akasaki, I. Nobel Lecture: Fascinated journeys into blue light. *Reviews of Modern Physics* **87**, 1119-1131, doi:10.1103/RevModPhys.87.1119 (2015).

37 Nakamura, S. Nobel Lecture: Background story of the invention of efficient blue InGaN light emitting diodes. *Reviews of Modern Physics* **87**, 1139-1151, doi:10.1103/RevModPhys.87.1139 (2015).

38 Sun, Y. *et al.* Room-temperature continuous-wave electrically injected InGaN-based laser directly grown on Si. *Nature Photonics* **10**, 595-599, doi:10.1038/nphoton.2016.158 (2016).

39 Li, D., Jiang, K., Sun, X. & Guo, C. AlGaN photonics: recent advances in materials and ultraviolet devices. *Advances in Optics and Photonics* **10**, 43-110, doi:10.1364/AOP.10.000043 (2018).

40 Zhu, D. & Humphreys, C. J. in *Optics in Our Time* (eds Mohammad D. Al-Amri, Mohamed El-Gomati, & M. Suhail Zubairy) 87-118 (Springer International Publishing, 2016).

41 Batson, P. E., Dellby, N. & Krivanek, O. L. Sub-ångstrom resolution using aberration corrected electron optics. *Nature* **418**, 617-620, doi:10.1038/nature00972 (2002).

42 Muller, D. A. *et al.* Atomic-Scale Chemical Imaging of Composition and Bonding by Aberration-Corrected Microscopy. *Science* **319**, 1073-1076, doi:10.1126/science.1148820 (2008).

43 Mundy, J. A. *et al.* Visualizing the interfacial evolution from charge compensation to metallic screening across the manganite metal–insulator transition. *Nature Communications* **5**, 3464, doi:10.1038/ncomms4464 (2014).

44 Feynman, R. P., Leighton, R. B. & Sands, M. *The Feynman Lectures on Physics, Vol. I: The New Millennium Edition: Mainly Mechanics, Radiation, and Heat*. (Basic Books, 2011).

45 Reimer, L. *Scanning Electron Microscopy: Physics of Image Formation and Microanalysis*. (Springer, 2013).

46 Batson, P. E. Simultaneous STEM imaging and electron energy-loss spectroscopy with atomic-column sensitivity. *Nature* **366**, 727-728, doi:10.1038/366727a0 (1993).

47 Keast, V. J., Scott, A. J., Brydson, R., Williams, D. B. & Bruley, J. Electron energy-loss near-edge structure – a tool for the investigation of electronic structure on the nanometre scale. *Journal of Microscopy* **203**, 135-175, doi:10.1046/j.1365-2818.2001.00898.x (2001).

48 Muller, D. A., Singh, D. J. & Silcox, J. Connections between the electron-energy-loss spectra, the local electronic structure, and the physical properties of a material: A study of nickel aluminum alloys. *Physical Review B* **57**, 8181-8202, doi:10.1103/PhysRevB.57.8181 (1998).

49 Keast, V. J., Kappers, M. J. & Humphreys, C. J. Electron energy-loss near edge structure (ELNES) of InGaN quantum wells. *Journal of Microscopy* **210**, 89-93, doi:10.1046/j.1365-2818.2003.01180.x (2003).

50 Egerton, R. F. *Electron Energy-Loss Spectroscopy in the Electron Microscope*. (Springer Science & Business Media, 2011).

51 Goldstein, J. *et al. Scanning Electron Microscopy and X-ray Microanalysis: Third Edition*. (Springer US, 2003).

52 Valiev, R. Nanostructuring of metals by severe plastic deformation for advanced properties. *Nature Materials* **3**, 511-516, doi:10.1038/nmat1180 (2004).

53 Hofmann, D. C. *et al.* Designing metallic glass matrix composites with high toughness and tensile ductility. *Nature* **451**, 1085-1089, doi:10.1038/nature06598 (2008).

54 Barthelat, F., Tang, H., Zavattieri, P. D., Li, C. M. & Espinosa, H. D. On the mechanics of mother-of-pearl: A key feature in the material hierarchical structure. *Journal of the Mechanics and Physics of Solids* **55**, 306-337, doi:10.1016/j.jmps.2006.07.007 (2007).

55 Currey, J. D. Mechanical properties of mother of pearl in tension. *Proc. R. Soc. Lond. B* **196**, 443-463, doi:10.1098/rspb.1977.0050 (1977).

56 Wang, R. Z., Suo, Z., Evans, A. G., Yao, N. & Aksay, I. A. Deformation mechanisms in nacre. *Journal of Materials Research* **16**, 2485-2493, doi:10.1557/JMR.2001.0340 (2001).

57 Song, F., Soh, A. K. & Bai, Y. L. Structural and mechanical properties of the organic matrix layers of nacre. *Biomaterials* **24**, 3623-3631, doi:10.1016/S0142-9612(03)00215-1 (2003).

58 Li, X., Chang, W.-C., Chao, Y. J., Wang, R. & Chang, M. Nanoscale Structural and Mechanical Characterization of a Natural Nanocomposite Material: The Shell of Red Abalone. *Nano Letters* **4**, 613-617, doi:10.1021/nl049962k (2004).

59 Evans, A. G. *et al.* Model for the robust mechanical behavior of nacre. *Journal of Materials Research* **16**, 2475-2484, doi:10.1557/JMR.2001.0339 (2001).

60 Smith, B. L. *et al.* Molecular mechanistic origin of the toughness of natural adhesives, fibres and composites. *Nature* **399**, 761-763, doi:10.1038/21607 (1999).

61 Li, X., Xu, Z.-H. & Wang, R. In Situ Observation of Nanograin Rotation and Deformation in Nacre. *Nano Letters* **6**, 2301-2304, doi:10.1021/nl061775u (2006).

62 Espinosa, H. D. *et al.* Tablet-level origin of toughening in abalone shells and translation to synthetic composite materials. *Nature Communications* **2**, 173, doi:10.1038/ncomms1172 (2011).

63 Jacob, D. E. *et al.* Nanostructure, composition and mechanisms of bivalve shell growth. *Geochimica et Cosmochimica Acta* **72**, 5401-5415, doi:10.1016/j.gca.2008.08.019 (2008).

64 Hovden, R. *et al.* Nanoscale assembly processes revealed in the nacroprismatic transition zone of Pinna nobilis mollusc shells. *Nature Communications* **6**, doi:10.1038/ncomms10097 (2015).

65 Wolf, S. E. *et al.* Nonclassical crystallization in vivo et in vitro (I): Process-structure-property relationships of nanogranular biominerals. *Journal of Structural Biology* **196**, 244-259, doi:10.1016/j.jsb.2016.07.016 (2016).

66 Dauphin, Y. Nanostructures de la nacre des tests de céphalopodes actuels. *PalZ* **75**, 113-122, doi:10.1007/BF03022601 (2001).

67 Yang, L., E. Killian, C., Kunz, M., Tamura, N. & A. Gilbert, P. U. P. Biomineral nanoparticles are space-filling. *Nanoscale* **3**, 603-609, doi:10.1039/C0NR00697A (2011).

68 Barthelat, F., Li, C.-M., Comi, C. & Espinosa, H. D. Mechanical properties of nacre constituents and their impact on mechanical performance. *Journal of Materials Research* **21**, 1977-1986, doi:10.1557/jmr.2006.0239 (2006).

69 Checa, A. G., Cartwright, J. H. E. & Willinger, M.-G. Mineral bridges in nacre. *Journal of Structural Biology* **176**, 330-339, doi:10.1016/j.jsb.2011.09.011 (2011).

70 Younis, S., Kauffmann, Y., Bloch, L. & Zolotoyabko, E. Inhomogeneity of Nacre Lamellae on the Nanometer Length Scale. *Crystal Growth & Design* **12**, 4574-4579, doi:10.1021/cg3007734 (2012).

71 Nudelman, F. Nacre biomineralisation: A review on the mechanisms of crystal nucleation. *Seminars in Cell & Developmental Biology* **46**, 2-10, doi:10.1016/j.semcdb.2015.07.004 (2015).

72 Gu, G. X., Libonati, F., Wettermark, S. D. & Buehler, M. J. Printing nature: Unraveling the role of nacre's mineral bridges. *Journal of the Mechanical Behavior of Biomedical Materials* **76**, 135-144, doi:10.1016/j.jmbbm.2017.05.007 (2017).

73 Barthelat, F. & Espinosa, H. D. An Experimental Investigation of Deformation and Fracture of Nacre–Mother of Pearl. *Experimental Mechanics* **47**, 311-324, doi:10.1007/s11340-007-9040-1 (2007).

74 Menig, R., Meyers, M. H., Meyers, M. A. & Vecchio, K. S. Quasi-static and dynamic mechanical response of Haliotis rufescens (abalone) shells. *Acta Materialia* **48**, 2383-2398, doi:10.1016/S1359-6454(99)00443-7 (2000).

75 Stach, E. A. *et al.* Development of a Nanoindenter for In Situ Transmission Electron Microscopy. *Microscopy and Microanalysis* **7**, 507-517, doi:10.1007/S10005-001-0012-4 (2001).

76 Minor, A. M. *et al.* A new view of the onset of plasticity during the nanoindentation of aluminium. *Nature Materials* **5**, 697-702, doi:10.1038/nmat1714 (2006).

77 Jackson, A. P., Vincent, J. F. V. & Turner, R. M. Comparison of nacre with other ceramic composites. *Journal of Materials Science* **25**, 3173-3178, doi:10.1007/BF00587670 (1990).

78 Lin, A. Y.-M. *Structural and functional biological materials : abalone nacre, sharp materials, and abalone foot adhesion*, UC San Diego, (2008).

79 Cueva, P., Hovden, R., Mundy, J. A., Xin, H. L. & Muller, D. A. Data Processing for Atomic Resolution Electron Energy Loss Spectroscopy. *Microscopy and Microanalysis* **18**, 667-675, doi:10.1017/S1431927612000244 (2012).

80 Agbaje, O. B. A. *et al.* Architecture of crossed-lamellar bivalve shells: the southern giant clam (Tridacna derasa, Röding, 1798). *Royal Society Open Science* **4**, 170622, doi:10.1098/rsos.170622.

81 Dauphin, Y., Cuif, J.-P. & Massard, P. Persistent organic components in heated coral aragonitic skeletons–Implications for palaeoenvironmental reconstructions. *Chemical Geology* **231**, 26-37, doi:10.1016/j.chemgeo.2005.12.010 (2006).

82 Bourrat, X. *et al.* Nacre biocrystal thermal behaviour. *CrystEngComm* **9**, 1205-1208, doi:10.1039/B709388H (2007).

83 Hall, E. O. The Deformation and Ageing of Mild Steel: III Discussion of Results. *Proceedings of the Physical Society. Section B* **64**, 747-753, doi:10.1088/0370-1301/64/9/303 (1951).

84 Petch, N. The Cleavage Strength of Polycrystals. *Journal of the Iron and Steel Institute* **174**, 4 (1953).

85 Fantner, G. E. *et al.* Sacrificial bonds and hidden length dissipate energy as mineralized fibrils separate during bone fracture. *Nature Materials* **4**, 612-616, doi:10.1038/nmat1428 (2005).

86 Evans, A. G. & Charles, E. A. Fracture Toughness Determinations by Indentation. *Journal of the American Ceramic Society* **59**, 371-372, doi:10.1111/j.1151-2916.1976.tb10991.x (1976).

87 Okumura, K. & de Gennes, P. G. Why is nacre strong? Elastic theory and fracture mechanics for biocomposites with stratified structures. *The European Physical Journal E* **4**, 121-127, doi:10.1007/s101890170150 (2001).

88 Fitzer, S. C. *et al.* Ocean acidification alters the material properties of Mytilus edulis shells. *Journal of the Royal Society Interface* **12**, doi:10.1098/rsif.2014.1227 (2015).

89 Stempflé, P., Pantalé, O., Rousseau, M., Lopez, E. & Bourrat, X. Mechanical properties of the elemental nanocomponents of nacre structure. *Materials Science and Engineering: C* **30**, 715-721, doi:10.1016/j.msec.2010.03.003 (2010).

90 Sun, J.-y. & Tong, J. Fracture toughness properties of three different biomaterials measured by nanoindentation. *Journal of Bionic Engineering* **4**, 11-17, doi:10.1016/S1672-6529(07)60007-9 (2007).

91 Kunitake, M. E., Mangano, L. M., Peloquin, J. M., Baker, S. P. & Estroff, L. A. Evaluation of strengthening mechanisms in calcite single crystals from mollusk shells. *Acta Biomaterialia* **9**, 5353-5359, doi:10.1016/j.actbio.2012.09.030 (2013).

92 Merkel, C. *et al.* Mechanical properties of modern calcite- (Mergerlia truncata) and phosphate-shelled brachiopods (Discradisca stella and Lingula anatina) determined by nanoindentation. *Journal of Structural Biology* **168**, 396-408, doi:10.1016/j.jsb.2009.08.014 (2009).

93 Wu, B., Heidelberg, A. & Boland, J. J. Mechanical properties of ultrahigh-strength gold nanowires. *Nature Materials* **4**, 525, doi:10.1038/nmat1403 (2005).

94 Espinosa, H. D., Prorok, B. C. & Peng, B. Plasticity size effects in free-standing submicron polycrystalline FCC films subjected to pure tension. *Journal of the Mechanics and Physics of Solids* **52**, 667-689, doi:10.1016/j.jmps.2003.07.001 (2004).

95 Peng, B. *et al.* Measurements of near-ultimate strength for multiwalled carbon nanotubes and irradiation-induced crosslinking improvements. *Nature Nanotechnology* **3**, 626-631, doi:10.1038/nnano.2008.211 (2008).

96 Minor, A. M. & Dehm, G. Advances in in situ nanomechanical testing. *MRS Bulletin* **44**, 438-442, doi:10.1557/mrs.2019.127 (2019).

97 Bhowmick, S., Espinosa, H., Jungjohann, K., Pardoen, T. & Pierron, O. Advanced microelectromechanical systems-based nanomechanical testing: Beyond stress and strain

measurements. *MRS Bulletin* **44**, 487-493, doi:10.1557/mrs.2019.123 (2019).

98 Liu, L.-g., Chen, C.-c., Lin, C.-C. & Yang, Y.-j. Elasticity of single-crystal aragonite by Brillouin spectroscopy. *Physics and Chemistry of Minerals* **32**, 97-102, doi:10.1007/s00269-005-0454-y (2005).

99 Kearney, C. *et al.* Nanoscale Anisotropic Plastic Deformation in Single Crystal Aragonite. *Physical Review Letters* **96**, 255505, doi:10.1103/PhysRevLett.96.255505 (2006).

100 Lin, A. & Meyers, M. A. Growth and structure in abalone shell. *Materials Science and Engineering: A* **390**, 27-41, doi:10.1016/j.msea.2004.06.072 (2005).

101 Wang, J., Cheng, Q. & Tang, Z. Layered nanocomposites inspired by the structure and mechanical properties of nacre. *Chemical Society Reviews* **41**, 1111-1129, doi:10.1039/C1CS15106A (2012).

102 Nukala, P. K. V. V. & Simunovic, S. A continuous damage random thresholds model for simulating the fracture behavior of nacre. *Biomaterials* **26**, 6087-6098, doi:10.1016/j.biomaterials.2005.03.013 (2005).

103 Blake, J. M. Brick (José Cornejo Franco Library, Guadalajara, Maxico, 2007).

104 Bellini, T., Radzihovsky, L., Toner, J. & Clark, N. A. Universality and Scaling in the Disordering of a Smectic Liquid Crystal. *Science* **294**, 1074-1079, doi:10.1126/science.1057480 (2001).

105 Keen, D. A. & Goodwin, A. L. The crystallography of correlated disorder. *Nature* **521**, 303-309, doi:10.1038/nature14453 (2015).

106 Hosemann, R., Vogel, W., Weick, D. & Baltá-Calleja, F. J. Novel aspects of the real paracrystal. *Acta Crystallographica Section A: Crystal Physics, Diffraction, Theoretical and General Crystallography* **37**, 85-91, doi:10.1107/S0567739481000156 (1981).

107 Wilson, J. S. Stability of Structures. *Nature* **136**, 568-571, doi:10.1038/136568a0 (1935).

108 Hendry, A. W. in *Structural Masonry* (ed Arnold W. Hendry) 1-15 (Macmillan Education UK, 1998).

109 Mark, R. & Hutchinson, P. On the Structure of the Roman Pantheon. *The Art Bulletin* **68**, 24-34, doi:10.1080/00043079.1986.10788309 (1986).

110 Whitesides, G. M. & Grzybowski, B. Self-Assembly at All Scales. *Science* **295**, 2418-2421, doi:10.1126/science.1070821 (2002).

111 Bayerlein, B. *et al.* Self-similar mesostructure evolution of the growing mollusc shell reminiscent of thermodynamically driven grain growth. *Nature Materials* **13**, 1102-1107, doi:10.1038/nmat4110 (2014).

112 Zhou, G.-T., Yao, Q.-Z., Ni, J. & Jin, G. Formation of aragonite mesocrystals and implication for biomineralization. *American Mineralogist* **94**, 293-302, doi:10.2138/am.2009.2957 (2009).

113 Addadi, L. & Weiner, S. A pavement of pearl. *Nature* **389**, 912-913, doi:10.1038/40010 (1997).

114 Gilbert, P. U. P. A. *et al.* Nacre tablet thickness records formation temperature in modern and fossil shells. *Earth and Planetary Science Letters* **460**, 281-292, doi:10.1016/j.epsl.2016.11.012 (2017).

115 Olson, I. C., Kozdon, R., Valley, J. W. & Gilbert, P. U. P. A. Mollusk Shell Nacre Ultrastructure Correlates with Environmental Temperature and Pressure. *Journal of the American Chemical Society* **134**, 7351-7358, doi:10.1021/ja210808s (2012).

116 Salman, J. *et al.* Hyperspectral interference tomography of nacre. *arXiv:2010.08170 [physics]* (2020).

117 Barthelat, F., Yin, Z. & Buehler, M. J. Structure and mechanics of interfaces in biological materials. *Nature Reviews Materials* **1**, 1-16, doi:10.1038/natrevmats.2016.7 (2016).

118 Deng, Z. *et al.* Strategies for simultaneous strengthening and toughening via nanoscopic intracrystalline defects in a biogenic ceramic. *Nature Communications* **11**, 5678, doi:10.1038/s41467-020-19416-2 (2020).

119 Munch, E. *et al.* Tough, Bio-Inspired Hybrid Materials. *Science* **322**, 1516-1520, doi:10.1126/science.1164865 (2008).

120 Bouville, F. *et al.* Strong, tough and stiff bioinspired ceramics from brittle constituents. *Nature Materials* **13**, 508-514, doi:10.1038/nmat3915 (2014).

121 Zhao, C. *et al.* Layered nanocomposites by shear-flow-induced alignment of nanosheets.

Nature **580**, 210-215, doi:10.1038/s41586-020-2161-8 (2020).

122 Beliaev, M., Zöllner, D., Pacureanu, A., Zaslansky, P. & Zlotnikov, I. Dynamics of topological defects and structural synchronization in a forming periodic tissue. *Nature Physics*, 1-6, doi:10.1038/s41567-020-01069-z (2021).

123 Hänni, H. A. A short review of the use of 'keshi' as a term to describe pearls. *The Journal of Gemmology* **30**, 51-58, doi:10.15506/JoG.2006.30.1.51 (2006).

124 Otter, L. M., Oluwatooshin, B. A. A., Huong, L. T.-T., Hager, T. & Jacob, D. E. Akoya Cultured Pearl Farming in Eastern Australia | Gems & Gemology. *Gem & Gemology* **53** (2017).

125 Runnegar, B. in *Origin, Evolution, and Modern Aspects of Biomineralization in Plants and Animals* (ed Rex E. Crick) 75-94 (Springer US, 1989).

126 Savitzky, B. H. *et al.* Propagation of Structural Disorder in Epitaxially Connected Quantum Dot Solids from Atomic to Micron Scale. *Nano Letters* **16**, 5714-5718, doi:10.1021/acs.nanolett.6b02382 (2016).

127 Schwartz, J. *et al.* Removing Stripes, Scratches, and Curtaining with Nonrecoverable Compressed Sensing. *Microscopy and Microanalysis* **25**, 705-710, doi:10.1017/S1431927619000254 (2019).

128 Otter, L. M., Wehrmeister, U., Enzmann, F., Wolf, M. & Jacob, D. E. A Look Inside a Remarkably Large Beaded South Sea Cultured Pearl. *Gems & Gemology* **50**, 58-62, doi:10.5741/GEMS.50.1.58 (2014).

129 Krzemnicki, M., Friess, D., Chalus, P., Hänni, H. & Karampelas, S. X-Ray Computed Microtomography: Distinguishing Natural Pearls from Beaded and Non-Beaded Cultured Pearls. *Gems and Gemology* **46**, 128, doi:10.5741/GEMS.46.2.128 (2010).

130 Checa, A. G. Physical and Biological Determinants of the Fabrication of Molluscan Shell Microstructures. *Frontiers in Marine Science* **5**, doi:10.3389/fmars.2018.00353 (2018).

131 Meyers, M. A. *et al.* The role of organic intertile layer in abalone nacre. *Materials Science and Engineering: C* **29**, 2398-2410, doi:10.1016/j.msec.2009.07.005 (2009).

132 De Yoreo, J. J. *et al.* Crystallization by particle attachment in synthetic, biogenic, and geologic environments. *Science* **349**, aaa6760-aaa6760, doi:10.1126/science.aaa6760

(2015).

133 Gal, A. *et al.* Particle Accretion Mechanism Underlies Biological Crystal Growth from an Amorphous Precursor Phase. *Advanced Functional Materials* **24**, 5420-5426, doi:10.1002/adfm.201400676 (2014).

134 Schoeppler, V. *et al.* Crystal growth kinetics as an architectural constraint on the evolution of molluscan shells. *Proceedings of the National Academy of Sciences* **116**, 20388-20397, doi:10.1073/pnas.1907229116 (2019).

135 Willinger, M. G., Checa, A. G., Bonarski, J. T., Faryna, M. & Berent, K. Biogenic Crystallographically Continuous Aragonite Helices: The Microstructure of the Planktonic Gastropod Cuvierina. *Advanced Functional Materials* **26**, 553-561, doi:https://doi.org/10.1002/adfm.201504034 (2016).

136 Freer, A., Greenwood, D., Chung, P., Pannell, C. L. & Cusack, M. Aragonite Prism−Nacre Interface in Freshwater Mussels Anodonta anatina (Linnaeus, 1758) and Anodonta cygnea (L. 1758). *Crystal Growth & Design* **10**, 344-347, doi:10.1021/cg901265x (2010).

137 Voyles, P. M. *et al.* Structure and physical properties of paracrystalline atomistic models of amorphous silicon. *Journal of Applied Physics* **90**, 4437-4451, doi:10.1063/1.1407319 (2001).

138 Hindeleh, A. M. & Hosemann, R. Microparacrystals: The intermediate stage between crystalline and amorphous. *Journal of Materials Science* **26**, 5127-5133, doi:10.1007/BF01143202 (1991).

139 Cartwright, J. H. E., Checa, A. G., Escribano, B. & Sainz-Díaz, C. I. Spiral and target patterns in bivalve nacre manifest a natural excitable medium from layer growth of a biological liquid crystal. *Proceedings of the National Academy of Sciences* **106**, 10499-10504, doi:10.1073/pnas.0900867106 (2009).

140 Wada, K. Spiral Growth of Nacre. *Nature* **211**, 1427-1427, doi:10.1038/2111427a0 (1966).

141 Yao, N., Epstein, A. & Akey, A. Crystal growth via spiral motion in abalone shell nacre. *Journal of Materials Research* **21**, 1939-1946, doi:10.1557/jmr.2006.0252 (2006).

142 Yang, N. & Lu, K. Effects of transition metals on the evolution of polymer-derived SiOC ceramics. *Carbon* **171**, 88-95, doi:10.1016/j.carbon.2020.08.072 (2021).

143 Ikuhara, Y. Oxide Ceramics with High Density Dislocations and Their Properties. *Materials Transactions* **50**, 1626-1632, doi:10.2320/matertrans.MF200928 (2009).

144 Erland, S. & Greenwood, P. E. Constructing $1/{\ensuremath{\omega}}^{\ensuremath{\alpha}}$ noise from reversible Markov chains. *Physical Review E* **76**, 031114, doi:10.1103/PhysRevE.76.031114 (2007).

145 Erland, S., Greenwood, P. E. & Ward, L. M. "1/f $\upalpha$ noise" is equivalent to an eigenstructure power relation. *EPL (Europhysics Letters)* **95**, 60006, doi:10.1209/0295-5075/95/60006 (2011).

146 Bak, P., Tang, C. & Wiesenfeld, K. Self-organized criticality: An explanation of the 1/f noise. *Physical Review Letters* **59**, 381-384, doi:10.1103/PhysRevLett.59.381 (1987).

147 Bak, P., Tang, C. & Wiesenfeld, K. Self-organized criticality. *Physical Review A* **38**, 364-374, doi:10.1103/PhysRevA.38.364 (1988).

148 Cajochen, C. *et al.* Evidence that the Lunar Cycle Influences Human Sleep. *Current Biology* **23**, 1485-1488, doi:10.1016/j.cub.2013.06.029 (2013).

149 Tran, D. *et al.* Field Chronobiology of a Molluscan Bivalve: How the Moon and Sun Cycles Interact to Drive Oyster Activity Rhythms. *Chronobiology International* **28**, 307-317, doi:10.3109/07420528.2011.565897 (2011).

150 Nakajima, M. *et al.* Reconstitution of Circadian Oscillation of Cyanobacterial KaiC Phosphorylation in Vitro. *Science* **308**, 414-415, doi:10.1126/science.1108451 (2005).

151 Scott, M., Gunderson, C. W., Mateescu, E. M., Zhang, Z. & Hwa, T. Interdependence of Cell Growth and Gene Expression: Origins and Consequences. *Science* **330**, 1099-1102, doi:10.1126/science.1192588 (2010).

152 Zhang, L. *et al.* Dissociation of Circadian and Circatidal Timekeeping in the Marine Crustacean Eurydice pulchra. *Current Biology* **23**, 1863-1873, doi:10.1016/j.cub.2013.08.038 (2013).

153 Tu, B. P. & McKnight, S. L. Metabolic cycles as an underlying basis of biological oscillations. *Nature Reviews Molecular Cell Biology* **7**, 696-701, doi:10.1038/nrm1980 (2006).

154 Carey, H. V., Andrews, M. T. & Martin, S. L. Mammalian Hibernation: Cellular and

Molecular Responses to Depressed Metabolism and Low Temperature. *Physiological Reviews* **83**, 1153-1181, doi:10.1152/physrev.00008.2003 (2003).

155 Storey, K. B. & Storey, J. M. Aestivation: signaling and hypometabolism. *Journal of Experimental Biology* **215**, 1425-1433, doi:10.1242/jeb.054403 (2012).

156 Withers, P., Pedler, S. & Guppy, M. Physiological Adjustments during Aestivation by the Australian Land Snail Rhagada tescorum (Mollusca : Pulmonata : Camaenidae). *Australian Journal of Zoology* **45**, 599-611, doi:10.1071/zo97009 (1997).

157 van der Weijden, A., Winkens, M., Schoenmakers, S. M. C., Huck, W. T. S. & Korevaar, P. A. Autonomous mesoscale positioning emerging from myelin filament self-organization and Marangoni flows. *Nature Communications* **11**, 4800, doi:10.1038/s41467-020-18555-w (2020).

158 Karsenti, E. Self-organization in cell biology: a brief history. *Nature Reviews Molecular Cell Biology* **9**, 255-262, doi:10.1038/nrm2357 (2008).

159 te Brinke, E. *et al.* Dissipative adaptation in driven self-assembly leading to self-dividing fibrils. *Nature Nanotechnology* **13**, 849-855, doi:10.1038/s41565-018-0192-1 (2018).

160 Liu, M., Li, Q. & Zhu, F. Threshold negative binomial autoregressive model. *Statistics* **53**, 1-25, doi:10.1080/02331888.2018.1546307 (2019).

161 Qiu, F., Sridharan, H. & Chun, Y. Spatial Autoregressive Model for Population Estimation at the Census Block Level Using LIDAR-derived Building Volume Information. *Cartography and Geographic Information Science* **37**, 239-257, doi:10.1559/152304010792194949 (2010).

162 Hayes, R. J. Methods for assessing whether change depends on initial value. *Statistics in Medicine* **7**, 915-927, doi:https://doi.org/10.1002/sim.4780070903 (1988).

163 Montoya, J. H. *et al.* Materials for solar fuels and chemicals. *Nature Materials* **16**, 70-81, doi:10.1038/nmat4778 (2017).

164 G. Kibria, M. & Mi, Z. Artificial photosynthesis using metal/nonmetal-nitride semiconductors: current status, prospects, and challenges. *Journal of Materials Chemistry A* **4**, 2801-2820, doi:10.1039/C5TA07364B (2016).

165 Kuykendall, T., Ulrich, P., Aloni, S. & Yang, P. Complete composition tunability of InGaN

nanowires using a combinatorial approach. *Nature Materials* **6**, 951-956, doi:10.1038/nmat2037 (2007).

166 Hu, S., Xiang, C., Haussener, S., Berger, A. D. & Lewis, N. S. An analysis of the optimal band gaps of light absorbers in integrated tandem photoelectrochemical water-splitting systems. *Energy & Environmental Science* **6**, 2984-2993, doi:10.1039/C3EE40453F (2013).

167 Caetano, C., Teles, L. K., Marques, M., Dal Pino, A. & Ferreira, L. G. Phase stability, chemical bonds, and gap bowing of ${\mathrm{In}}_{x}{\mathrm{Ga}}_{1\ensuremath{-}x}\mathrm{N}$ alloys: Comparison between cubic and wurtzite structures. *Physical Review B* **74**, 045215, doi:10.1103/PhysRevB.74.045215 (2006).

168 Ertekin, E., Greaney, P. A., Chrzan, D. C. & Sands, T. D. Equilibrium limits of coherency in strained nanowire heterostructures. *Journal of Applied Physics* **97**, 114325, doi:10.1063/1.1903106 (2005).

169 Light emitting diodes 2nd edition | Electronic, optoelectronic devices, and nanotechnology | Cambridge University Press.

170 Woo, S. Y., Bugnet, M., Nguyen, H. P. T., Mi, Z. & Botton, G. A. Atomic Ordering in InGaN Alloys within Nanowire Heterostructures. *Nano Letters* **15**, 6413-6418, doi:10.1021/acs.nanolett.5b01628 (2015).

171 Kneissl, M., Seong, T.-Y., Han, J. & Amano, H. The emergence and prospects of deep-ultraviolet light-emitting diode technologies. *Nature Photonics* **13**, 233-244, doi:10.1038/s41566-019-0359-9 (2019).

172 Shakya, J. *et al.* Polarization of III-nitride blue and ultraviolet light-emitting diodes. *Applied Physics Letters* **86**, 091107, doi:10.1063/1.1875751 (2005).

173 Zhao, P., Han, L., McGoogan, M. R. & Zhao, H. Analysis of TM mode light extraction efficiency enhancement for deep ultraviolet AlGaN quantum wells light-emitting diodes with III-nitride micro-domes. *Optical Materials Express* **2**, 1397-1406, doi:10.1364/OME.2.001397 (2012).

174 Guttmann, M. *et al.* Optical light polarization and light extraction efficiency of AlGaN-based LEDs emitting between 264 and 220 nm. *Japanese Journal of Applied Physics* **58**, SCCB20, doi:10.7567/1347-4065/ab0d09 (2019).

175 Northrup, J. E. *et al.* Effect of strain and barrier composition on the polarization of light emission from AlGaN/AlN quantum wells. *Applied Physics Letters* **100**, 021101, doi:10.1063/1.3675451 (2012).

176 Ban, K. *et al.* Internal Quantum Efficiency of Whole-Composition-Range AlGaN Multiquantum Wells. *Applied Physics Express* **4**, 052101, doi:10.1143/APEX.4.052101 (2011).

177 Hirayama, H. *et al.* 222–282 nm AlGaN and InAlGaN-based deep-UV LEDs fabricated on high-quality AlN on sapphire. *physica status solidi (a)* **206**, 1176-1182, doi:https://doi.org/10.1002/pssa.200880961 (2009).

178 Nakarmi, M. L. *et al.* Correlation between optical and electrical properties of Mg-doped AlN epilayers. *Applied Physics Letters* **89**, 152120, doi:10.1063/1.2362582 (2006).

179 Taniyasu, Y. & Kasu, M. Polarization property of deep-ultraviolet light emission from C-plane AlN/GaN short-period superlattices. *Applied Physics Letters* **99**, 251112, doi:10.1063/1.3671668 (2011).

180 Stampfl, C. & Van de Walle, C. G. Theoretical investigation of native defects, impurities, and complexes in aluminum nitride. *Physical Review B* **65**, 155212, doi:10.1103/PhysRevB.65.155212 (2002).

181 Mymrin, V. F., Bulashevich, K. A., Podolskaya, N. I. & Karpov, S. Y. Bandgap engineering of electronic and optoelectronic devices on native AlN and GaN substrates: A modelling insight. *Journal of Crystal Growth* **281**, 115-124, doi:10.1016/j.jcrysgro.2005.03.019 (2005).

182 Shur, M. S. & Gaska, R. Deep-Ultraviolet Light-Emitting Diodes. *IEEE Transactions on Electron Devices* **57**, 12-25, doi:10.1109/TED.2009.2033768 (2010).

183 Kashima, Y. *et al.* High external quantum efficiency (10%) AlGaN-based deep-ultraviolet light-emitting diodes achieved by using highly reflective photonic crystal on p-AlGaN contact layer. *Applied Physics Express* **11**, 012101, doi:10.7567/APEX.11.012101 (2017).

184 Djavid, M. & Mi, Z. Enhancing the light extraction efficiency of AlGaN deep ultraviolet light emitting diodes by using nanowire structures. *Applied Physics Letters* **108**, 051102, doi:10.1063/1.4941239 (2016).

185 Liu, X., Mashooq, K., Szkopek, T. & Mi, Z. Improving the Efficiency of Transverse

Magnetic Polarized Emission from AlGaN Based LEDs by Using Nanowire Photonic Crystal. *IEEE Photonics Journal* **10**, 1-11, doi:10.1109/JPHOT.2018.2842110 (2018).

186 Zhao, S., Nguyen, H. P. T., Kibria, M. G. & Mi, Z. III-Nitride nanowire optoelectronics. *Progress in Quantum Electronics* **44**, 14-68, doi:10.1016/j.pquantelec.2015.11.001 (2015).

187 Dong, P. *et al.* 282-nm AlGaN-based deep ultraviolet light-emitting diodes with improved performance on nano-patterned sapphire substrates. *Applied Physics Letters* **102**, 241113, doi:10.1063/1.4812237 (2013).

188 Hirayama, H., Yatabe, T., Noguchi, N., Ohashi, T. & Kamata, N. 231–261nm AlGaN deep-ultraviolet light-emitting diodes fabricated on AlN multilayer buffers grown by ammonia pulse-flow method on sapphire. *Applied Physics Letters* **91**, 071901, doi:10.1063/1.2770662 (2007).

189 Susilo, N. *et al.* AlGaN-based deep UV LEDs grown on sputtered and high temperature annealed AlN/sapphire. *Applied Physics Letters* **112**, 041110, doi:10.1063/1.5010265 (2018).

190 Zhang, J. P. *et al.* AlGaN-based 280nm light-emitting diodes with continuous-wave power exceeding 1mW at 25mA. *Applied Physics Letters* **85**, 5532-5534, doi:10.1063/1.1831557 (2004).

191 Takano, T. *et al.* Deep-ultraviolet light-emitting diodes with external quantum efficiency higher than 20% at 275 nm achieved by improving light-extraction efficiency. *Applied Physics Express* **10**, 031002, doi:10.7567/APEX.10.031002 (2017).

192 Vilhunen, S., Särkkä, H. & Sillanpää, M. Ultraviolet light-emitting diodes in water disinfection. *Environmental Science and Pollution Research* **16**, 439-442, doi:10.1007/s11356-009-0103-y (2009).

193 Inoue, S.-i., Naoki, T., Kinoshita, T., Obata, T. & Yanagi, H. Light extraction enhancement of 265 nm deep-ultraviolet light-emitting diodes with over 90 mW output power via an AlN hybrid nanostructure. *Applied Physics Letters* **106**, 131104, doi:10.1063/1.4915255 (2015).

194 Inoue, S.-i., Tamari, N. & Taniguchi, M. 150 mW deep-ultraviolet light-emitting diodes with large-area AlN nanophotonic light-extraction structure emitting at 265 nm. *Applied Physics Letters* **110**, 141106, doi:10.1063/1.4978855 (2017).

195 Hao, G.-D., Tamari, N., Obata, T., Kinoshita, T. & Inoue, S.-i. Electrical determination of current injection and internal quantum efficiencies in AlGaN-based deep-ultraviolet light-emitting diodes. *Optics Express* **25**, A639-A648, doi:10.1364/OE.25.00A639 (2017).

196 Liao, Y. *et al.* Recent progress of efficient deep UV-LEDs by plasma-assisted molecular beam epitaxy. *physica status solidi c* **9**, 798-801, doi:https://doi.org/10.1002/pssc.201100438 (2012).

197 Lin, G.-B. *et al.* Analytic model for the efficiency droop in semiconductors with asymmetric carrier-transport properties based on drift-induced reduction of injection efficiency. *Applied Physics Letters* **100**, 161106, doi:10.1063/1.4704366 (2012).

198 Hirayama, H., Tsukada, Y., Maeda, T. & Kamata, N. Marked Enhancement in the Efficiency of Deep-Ultraviolet AlGaN Light-Emitting Diodes by Using a Multiquantum-Barrier Electron Blocking Layer. *Applied Physics Express* **3**, 031002, doi:10.1143/APEX.3.031002 (2010).

199 Zhang, Z.-H. *et al.* InGaN/GaN light-emitting diode with a polarization tunnel junction. *Applied Physics Letters* **102**, 193508, doi:10.1063/1.4806978 (2013).

200 Adivarahan, V. *et al.* 250nmAlGaN light-emitting diodes. *Applied Physics Letters* **85**, 2175-2177, doi:10.1063/1.1796525 (2004).

201 Yun, J., Shim, J.-I. & Hirayama, H. Analysis of efficiency droop in 280-nm AlGaN multiple-quantum-well light-emitting diodes based on carrier rate equation. *Applied Physics Express* **8**, 022104, doi:10.7567/APEX.8.022104 (2015).

202 Sun, W. *et al.* Efficiency droop in 245–247 nm AlGaN light-emitting diodes with continuous wave 2 mW output power. *Applied Physics Letters* **96**, 061102, doi:10.1063/1.3302466 (2010).

203 Hirayama, H., Maeda, N., Fujikawa, S., Toyoda, S. & Kamata, N. Recent progress and future prospects of AlGaN-based high-efficiency deep-ultraviolet light-emitting diodes. *Japanese Journal of Applied Physics* **53**, 100209, doi:10.7567/JJAP.53.100209 (2014).

204 Kamiya, K., Ebihara, Y., Shiraishi, K. & Kasu, M. Structural design of AlN/GaN superlattices for deep-ultraviolet light-emitting diodes with high emission efficiency. *Applied Physics Letters* **99**, 151108, doi:10.1063/1.3651335 (2011).

205 Islam, S. M. *et al.* Deep-UV emission at 219 nm from ultrathin MBE GaN/AlN quantum

heterostructures. *Applied Physics Letters* **111**, 091104, doi:10.1063/1.5000844 (2017).

206 Islam, S. M. *et al.* MBE-grown 232–270 nm deep-UV LEDs using monolayer thin binary GaN/AlN quantum heterostructures. *Applied Physics Letters* **110**, 041108, doi:10.1063/1.4975068 (2017).

207 Kobayashi, H., Ichikawa, S., Funato, M. & Kawakami, Y. Self-Limiting Growth of Ultrathin GaN/AlN Quantum Wells for Highly Efficient Deep Ultraviolet Emitters. *Advanced Optical Materials* **7**, 1900860, doi:https://doi.org/10.1002/adom.201900860 (2019).

208 Neumayer, D. A. & Ekerdt, J. G. Growth of Group III Nitrides. A Review of Precursors and Techniques. *Chemistry of Materials* **8**, 9-25, doi:10.1021/cm950108r (1996).

209 Nakamura, S. The Roles of Structural Imperfections in InGaN-Based Blue Light-Emitting Diodes and Laser Diodes. *Science* **281**, 956-961, doi:10.1126/science.281.5379.956 (1998).

210 Wu, Y. *et al.* Controlling Defect Formation of Nanoscale AlN: Toward Efficient Current Conduction of Ultrawide-Bandgap Semiconductors. *Advanced Electronic Materials* **6**, 2000337, doi:https://doi.org/10.1002/aelm.202000337 (2020).

211 Tran, N. H., Le, B. H., Zhao, S. & Mi, Z. On the mechanism of highly efficient p-type conduction of Mg-doped ultra-wide-bandgap AlN nanostructures. *Applied Physics Letters* **110**, 032102, doi:10.1063/1.4973999 (2017).

212 Zhao, S. *et al.* Three-Dimensional Quantum Confinement of Charge Carriers in Self-Organized AlGaN Nanowires: A Viable Route to Electrically Injected Deep Ultraviolet Lasers. *Nano Letters* **15**, 7801-7807, doi:10.1021/acs.nanolett.5b02133 (2015).

213 Zhao, S. *et al.* Molecular beam epitaxy growth of Al-rich AlGaN nanowires for deep ultraviolet optoelectronics. *APL Materials* **4**, 086115, doi:10.1063/1.4961680 (2016).

214 Moustakas, T. D. & Bhattacharyya, A. The role of liquid phase epitaxy during growth of AlGaN by MBE. *physica status solidi c* **9**, 580-583, doi:https://doi.org/10.1002/pssc.201100427 (2012).

215 Bhattacharyya, A., Moustakas, T. D., Zhou, L., Smith, D. J. & Hug, W. Deep ultraviolet emitting AlGaN quantum wells with high internal quantum efficiency. *Applied Physics Letters* **94**, 181907, doi:10.1063/1.3130755 (2009).

216 Pernot, C. *et al.* Improved Efficiency of 255–280 nm AlGaN-Based Light-Emitting Diodes. *Applied Physics Express* **3**, 061004, doi:10.1143/APEX.3.061004 (2010).

217 Chand, N. & Chu, S. N. G. Origin and improvement of interface roughness in AlGaAs/GaAs heterostructures grown by molecular beam epitaxy. *Applied Physics Letters* **57**, 1796-1798, doi:10.1063/1.104025 (1990).

218 Eliseev, P. G., Perlin, P., Lee, J. & Osiński, M. "Blue" temperature-induced shift and band-tail emission in InGaN-based light sources. *Applied Physics Letters* **71**, 569-571, doi:10.1063/1.119797 (1997).

219 Bayerl, D. *et al.* Deep ultraviolet emission from ultra-thin GaN/AlN heterostructures. *Applied Physics Letters* **109**, 241102, doi:10.1063/1.4971968 (2016).

220 Muller, D. A., Nakagawa, N., Ohtomo, A., Grazul, J. L. & Hwang, H. Y. Atomic-scale imaging of nanoengineered oxygen vacancy profiles in SrTiO 3. *Nature* **430**, 657-661, doi:10.1038/nature02756 (2004).

221 Gutt, R. *et al.* Reduction of the threading edge dislocation density in AlGaN epilayers by GaN nucleation for efficient 350 nm light emitting diodes. *physica status solidi (b)* **247**, 1710-1712, doi:https://doi.org/10.1002/pssb.200983526 (2010).

222 Chang, H. *et al.* Graphene-assisted quasi-van der Waals epitaxy of AlN film for ultraviolet light emitting diodes on nano-patterned sapphire substrate. *Applied Physics Letters* **114**, 091107, doi:10.1063/1.5081112 (2019).

223 Chen, Z. *et al.* Improved Epitaxy of AlN Film for Deep-Ultraviolet Light-Emitting Diodes Enabled by Graphene. *Advanced Materials* **31**, 1807345, doi:https://doi.org/10.1002/adma.201807345 (2019).